



**COMPUTATIONAL AERODYNAMIC
ANALYSIS OF THE FLOW FIELD ABOUT A
HYPERVELOCITY TEST SLED**

THESIS

Andrew J. Lofthouse, Captain, USAF

AFIT/GAE/ENY/02-07

**DEPARTMENT OF THE AIR FORCE
AIR UNIVERSITY**

AIR FORCE INSTITUTE OF TECHNOLOGY

Wright-Patterson Air Force Base, Ohio

APPROVED FOR PUBLIC RELEASE; DISTRIBUTION UNLIMITED.

Report Documentation Page

Report Date 26 Mar 02	Report Type Final	Dates Covered (from... to) Sep 2001 - Mar 2002
Title and Subtitle Computational Aerodynamic Analysis of the Flow Field about a Hypervelocity Test Sled	Contract Number	
	Grant Number	
	Program Element Number	
Author(s) Capt Andrew J. Lofthouse, USAF	Project Number	
	Task Number	
	Work Unit Number	
Performing Organization Name(s) and Address(es) Air Force Institute of Technology Graduate School of Engineering and Management (AFIT/EN) 2950 P Street, Bldg 640 WPAFB, OH 45433-7765	Performing Organization Report Number AFIT/GAE/ENY/02-07	
Sponsoring/Monitoring Agency Name(s) and Address(es) Dr. Len Sakell AFOSR/NM 801 N. Randall Street, Room 732 Arlington VA 22203-1977	Sponsor/Monitor's Acronym(s)	
	Sponsor/Monitor's Report Number(s)	
Distribution/Availability Statement Approved for public release, distribution unlimited		
Supplementary Notes The original document contains color images.		
Abstract The flow field about the nose section of a hypervelocity test sled is computed using computational fluid dynamics. The numerical model of the test sled corresponds to the Nike O/U narrow gage sled used in the upgrade program at the High Speed Test Track facility, Holloman Air Force Base, New Mexico. The high temperatures and pressures resulting from the aerodynamic heating and loading affect the sled structure and the performance of the vehicle. The sled transitions from an air environment to a helium environment at a speed of approximately 3,300 feet per second (Mach 3 in air, Mach 1.02 in helium) to reduce the effects of high Mach number flows. Steady, three-dimensional, inviscid flow solutions are computed for Mach numbers of 2 and 3 in air (2,200 and 3,300 feet per second), and for Mach numbers of 1.02, 2.5 and 3.1 in helium (3,300, 8,076 and 10,000 feet per second). Mesh adaptation is used to obtain a mesh-independent solution. Second-order solutions are obtained for the Mach 3 in air and Mach 1.02 in helium cases. The unsteady transition from air to helium at 3,300 feet per second is also modeled. Mach 3 in air computations are compared with analytical results.		

Subject Terms High Velocity, Test Vehicles, Computational Fluid Dynamics, Hypersonic Test Vehicles, Euler Equations	
Report Classification unclassified	Classification of this page unclassified
Classification of Abstract unclassified	Limitation of Abstract UU
Number of Pages 118	

The views expressed in this thesis are those of the author and do not reflect the official policy or position of the United States Air Force, the Department of Defense or the United States Government.

AFIT/GAE/ENY/02-07

COMPUTATIONAL AERODYNAMIC ANALYSIS OF THE FLOW FIELD
ABOUT A HYPERVELOCITY TEST SLED

THESIS

Presented to the Faculty

Department of Aeronautics and Astronautics

Graduate School of Engineering and Management

Air Force Institute of Technology

Air University

Air Education and Training Command

In Partial Fulfillment of the

Requirements for the Degree of

Master of Science in Aeronautical Engineering

Andrew J. Lofthouse, BS

Captain, USAF

March 2002

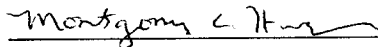
APPROVED FOR PUBLIC RELEASE; DISTRIBUTION UNLIMITED

AFIT/GAE/ENY/02-07

COMPUTATIONAL AERODYNAMIC ANALYSIS OF THE FLOW FIELD
ABOUT A HYPERVELOCITY TEST SLED

Andrew J. Lofthouse, BS
Captain, USAF

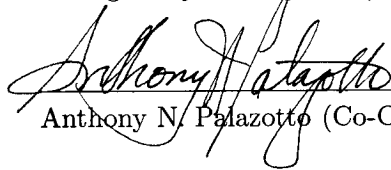
Approved:



Montgomery C. Hughson (Co-Chairman)

14 MARCH 2002

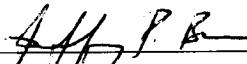
Date



Anthony N. Palazotto (Co-Chairman)

14 March 2002

Date



Jeffrey P. Bons (Member)

14 March 2002

Date

Acknowledgements

I am eternally grateful for the support and love my wife has shown me. Since the day we met as undergraduate students, she has inspired and motivated me beyond mere academic mediocrity. During the past year and a half, this support has continued as she has been a virtual "single mom" (as well as full-time graduate student herself) – taking care of our two children while "Dad is at school." The satisfaction of completing this research project would have been meaningless without having my family by my side throughout the entire process. I dedicate this work to them.

I am also indebted to Lt Col Monty Hughson for his guidance and insights into the "finer" aspects of CFD, and for his trust in me that I could accomplish such a work. The assistance of Lt Col Ray Maple was invaluable as well; not only is he a CFD genius, but also a rather skilled Linux guru.

Finally, this research wouldn't have been possible without the financial and technical support of Dr. Len Sakell of the Air Force Office of Scientific Research, Dr. Michael Hooser (and others) from the High Speed Test Track Facility at Holloman Air Force Base, New Mexico, and Dr. Anthony Palazotto.

Andrew J. Lofthouse

Table of Contents

	Page
Acknowledgements	iv
List of Figures	viii
List of Tables	xiii
List of Symbols	xiv
List of Abbreviations	xv
Abstract	xvi
 I. Introduction	 1-1
Background	1-1
Previous Work	1-3
The “Virtual Wind-Tunnel”	1-4
Research Objectives and Scope	1-6
 II. Computational Fluid Dynamics General Theory	 2-1
Equations of Fluid Flow	2-1
Finite Volume Method	2-2
Discretization of the Domain of Interest–Mesh Generation	2-3
Structured	2-3
Unstructured	2-3
Solution Accuracy	2-4
Validation and Verification	2-4
Mesh Independent Solutions	2-5
First- and Second-Order Accuracy	2-6
Time Accurate Solutions	2-7

	Page
III. Computational Facilities	3-1
Hardware	3-1
Software	3-1
Gridgen	3-1
FLUENT	3-2
Tecplot	3-2
IV. Numerical Simulation	4-1
Inviscid, Steady	4-1
Mesh Generation	4-1
Solver Initialization and Flow Solution	4-17
Mesh Adaptation	4-22
Inviscid, Unsteady	4-24
Solver Initialization and Flow Solution	4-24
V. Results and Discussion	5-1
Computational Time	5-1
Post-Processing Issues	5-3
Definitions	5-4
Analytical Solutions	5-5
Steady, Inviscid Flow	5-10
Overview of Results	5-10
Mach 3.0 in Air	5-19
Mach 1.02 in Helium	5-27
Slipper/Rail Gap	5-33
Unsteady, Inviscid Flow	5-41
VI. Conclusions and Recommendations	6-1
Future Work	6-2

	Page
Bibliography	BIB-1
Vita	VITA-1

List of Figures

Figure		Page
1.1.	Super Road Runner (SRR) Narrow Gage Sled	1-2
1.2.	Slipper and Rail Configuration (14:3)	1-2
1.3.	SRR Sled at 4,865 fps in Air (Mach 4.3)	1-2
4.1.	Experimental Sled Run Trajectory and Corresponding CFD Cases Modeled	4-2
4.2.	Technical Drawing of Nike O/U Sled	4-2
4.3.	Modeled Nose Portion of Sled	4-3
4.4.	Forward Assembly Cut-Away View, Looking Forward	4-3
4.5.	Isometric View of Forward Assembly, Including Slipper/Rail Area .	4-4
4.6.	Slipper/Rail Assembly Cut-Away Detailed View	4-4
4.7.	Modeled Domain Boundaries	4-6
4.8.	Initial Surface Mesh	4-7
4.9.	Initial Mesh on Rail Surface Near Slipper/Rail Gap	4-8
4.10.	Final Mesh on Rail Surface ($M_\infty = 3.0$ in Air)	4-9
4.11.	Final Mesh on Rail Surface ($M_\infty = 1.02$ in Helium)	4-9
4.12.	Initial Mesh at $y = 0$ Inches (Bottom Surface of Slipper Wedge) . .	4-10
4.13.	Initial Mesh at $y = -0.0625$ Inches (Half-Way Through Gap)	4-10
4.14.	Initial Mesh at $y = -0.125$ Inches (Top Surface of Rail)	4-11
4.15.	Adapted Mesh ($M_\infty = 3.0$ in Air) at $y = 0$ Inches (Bottom Surface of Slipper Wedge)	4-11
4.16.	Adapted Mesh ($M_\infty = 3.0$ in Air) at $y = -0.0625$ Inches (Half-Way Through Gap)	4-12
4.17.	Adapted Mesh ($M_\infty = 3.0$ in Air) at $y = -0.125$ (Top Surface of Rail)	4-12
4.18.	Adapted Mesh ($M_\infty = 1.02$ in Helium) at $y = 0$ Inches (Bottom Surface of Slipper Wedge)	4-13

Figure		Page
4.19.	Adapted Mesh ($M_\infty = 1.02$ in Helium) at $y = -0.0625$ Inches (Half-Way Through Gap)	4-13
4.20.	Adapted Mesh ($M_\infty = 1.02$ in Helium) at $y = -0.125$ Inches (Top Surface of Rail)	4-14
4.21.	Outflow Plane Mesh in Gap Area (Initial Mesh) at $x = 23.8$ Inches	4-15
4.22.	Mesh in Plane at $x = 22.6$ Inches	4-15
4.23.	Outflow Plane Mesh in Gap Area($M_\infty = 3.0$) in Air	4-16
4.24.	Outflow Plane Mesh in Gap Area ($M_\infty = 1.02$ in Helium)	4-16
4.25.	Residual History for $M_\infty = 3.0$ in Air	4-20
4.26.	Residual History for $M_\infty = 1.02$ in Helium	4-20
4.27.	Drag Coefficient History for $M_\infty = 3.0$ in Air	4-21
4.28.	Drag Coefficient History for $M_\infty = 1.02$ in Helium	4-21
5.1.	Regions of Flow Defined for Analytic Solution	5-6
5.2.	Regions of Flow Defined for Analytic Solution	5-6
5.3.	Region 1 Pressure	5-8
5.4.	Detail of Mesh on Payload Cone	5-8
5.5.	Region 2 Pressure	5-9
5.6.	Region 3 Pressure	5-9
5.7.	Region 4 Pressure	5-9
5.8.	Region 4 Pressure Contours	5-9
5.9.	Region 5 Pressure	5-10
5.10.	Mach Iso-Surface for $M_\infty = 2.0$ in Air (2,200 fps)	5-11
5.11.	Mach Iso-Surface for $M_\infty = 3.0$ in Air (3,300 fps)	5-12
5.12.	Mach Iso-Surface for $M_\infty = 1.02$ in Helium (3,300 fps)	5-12
5.13.	Mach Iso-Surface for $M_\infty = 2.5$ in Helium (8,076 fps)	5-13
5.14.	Mach Iso-Surface for $M_\infty = 3.10$ in Helium (10,000 fps)	5-13
5.15.	Surface Pressure Contours (psi) for $M_\infty = 2.0$ in Air	5-14

Figure		Page
5.16.	Surface Pressure Contours (psi) for $M_\infty = 3.0$ in Air	5-14
5.17.	Surface Pressure Contours (psi) for $M_\infty = 1.02$ in Helium	5-15
5.18.	Surface Pressure Contours (psi) for $M_\infty = 2.5$ in Helium	5-15
5.19.	Surface Pressure Contours (psi) for $M_\infty = 3.10$ in Helium	5-16
5.20.	Surface Temperature Contours ($^{\circ}\text{R}$) for $M_\infty = 2.0$ in Air	5-16
5.21.	Surface Temperature Contours ($^{\circ}\text{R}$) for $M_\infty = 3.0$ in Air	5-17
5.22.	Surface Temperature Contours ($^{\circ}\text{R}$) for $M_\infty = 1.02$ in Helium	5-17
5.23.	Surface Temperature Contours ($^{\circ}\text{R}$) for $M_\infty = 2.5$ in Helium	5-18
5.24.	Surface Temperature Contours ($^{\circ}\text{R}$) for $M_\infty = 3.10$ in Helium	5-18
5.25.	Surface Density Contours (lb_m/ft^3) for $M_\infty = 3.0$ in Air	5-19
5.26.	Surface Density Contour (lb_m/ft^3) Detail for $M_\infty = 3.0$ in Air	5-20
5.27.	Streamlines at $y = 4$ Inches in Flow for $M_\infty = 3.0$ in Air	5-20
5.28.	Side View of Streamlines in Flow for $M_\infty = 3.0$ in Air.	5-21
5.29.	Front View of Streamlines in Flow for $M_\infty = 3.0$ in Air.	5-21
5.30.	Density Contours (lb_m/ft^3) at $x = 19$ Inches for $M_\infty = 3.0$ in Air	5-22
5.31.	Density Contours (lb_m/ft^3) at $y = 3.4$ Inches for $M_\infty = 3.0$ in Air	5-23
5.32.	Pressure Contours (psi) at $x = 19$ Inches for $M_\infty = 3.0$ in Air	5-23
5.33.	Pressure Contours (psi) at $y = 3.4$ Inches for $M_\infty = 3.0$ in Air	5-24
5.34.	Temperature Contours ($^{\circ}\text{R}$) at $x = 19$ Inches for $M_\infty = 3.0$ in Air	5-24
5.35.	Temperature Contours ($^{\circ}\text{R}$) at $y = 3.4$ for $M_\infty = 3.0$ in Air	5-25
5.36.	Velocity Magnitude Contours (ft/s) at $x = 19$ Inches for $M_\infty = 3.0$ in Air	5-25
5.37.	Velocity Magnitude Contours (ft/s) at $y = 3.4$ Inches for $M_\infty = 3.0$ in Air	5-26
5.38.	Surface Density Contours (lb_m/ft^3) for $M_\infty = 1.02$ in Helium	5-28
5.39.	Density Contours (lb_m/ft^3) at $x = 0$ Inches for $M_\infty = 1.02$ in Helium	5-28
5.40.	Density Contours (lb_m/ft^3) at $x = 16$ Inches for $M_\infty = 1.02$ in Helium	5-29
5.41.	Density Contours (lb_m/ft^3) at $x = 18$ Inches for $M_\infty = 1.02$ in Helium	5-29

Figure		Page
5.42.	Density Contours (lb_m/ft^3) at $x = 20$ Inches for $M_\infty = 1.02$ in Helium	5-30
5.43.	Density Contours (lb_m/ft^3) at $x = 22$ Inches for $M_\infty = 1.02$ in Helium	5-30
5.44.	Density Contours (lb_m/ft^3) at $y = 5$ Inches for $M_\infty = 1.02$ in Helium	5-31
5.45.	Pressure Contours (psi) at $y = 5$ Inches for $M_\infty = 1.02$ in Helium	5-31
5.46.	Temperature Contours (psi) at $y = 5$ Inches for $M_\infty = 1.02$ in Helium	5-32
5.47.	Streamlines in Slipper/Rail Gap Area ($y = 0.2$ Inches) for $M_\infty = 3.0$ in Air.	5-34
5.48.	Streamlines in Slipper/Rail Gap Area ($y = 0.2$ Inches) for $M_\infty = 1.02$ in Helium	5-34
5.49.	Streamlines in Slipper/Rail Gap Area ($y = -0.0625$ Inches) for $M_\infty = 3.0$ in Air.	5-35
5.50.	Streamlines in Slipper/Rail Gap Area ($y = -0.0625$ Inches) for $M_\infty = 1.02$ in Helium	5-35
5.51.	Detail of Slipper/Rail Gap Area (Looking Up Through Transparent Rail)	5-36
5.52.	Definitions of Lines Used in Plots (Looking Up Through Rail to Bottom of Slipper Wedge)	5-37
5.53.	Pressure Distribution Along Line 1 (Outlet)	5-38
5.54.	Temperature Distribution Along Line 1 (Outlet)	5-38
5.55.	Pressure Distribution Along Line 2 (Inboard Side)	5-39
5.56.	Temperature Distribution Along Line 2 (Inboard Side)	5-39
5.57.	Pressure Distribution Along Line 3 (Outboard Side)	5-40
5.58.	Temperature Distribution Along Line 3 (Outboard Side)	5-40
5.59.	Mass Fraction of Air at $t = 1.0 \times 10^{-3}$ Seconds	5-42
5.60.	Mass Fraction of Air at $t = 2.0 \times 10^{-3}$ Seconds	5-42
5.61.	Mass Fraction of Air at $t = 3.0e - 3$ Seconds	5-43
5.62.	Mass Fraction of Air at $t = 4.0e - 3$ Seconds	5-43
5.63.	Drag Coefficient During Air-to-Helium Transition	5-44
5.64.	Static Pressure (psi) Contours at $t = 2.0 \times 10^{-3}$ Seconds	5-45

Figure		Page
5.65.	Static Pressure (psi) Contours at $t = 3.0 \times 10^{-3}$ Seconds	5-46
5.66.	Static Pressure (psi) Contours at $t = 3.3 \times 10^{-3}$ Seconds	5-46
5.67.	Static Pressure (psi) Contours at $t = 3.5 \times 10^{-3}$ Seconds	5-47
5.68.	Static Pressure (psi) Contours at $t = 3.7 \times 10^{-3}$ Seconds	5-47
5.69.	Static Pressure (psi) Contours at $t = 4.0 \times 10^{-3}$ Seconds	5-48
5.70.	Static Pressure (psi) Contours at $t = 4.5 \times 10^{-3}$ Seconds	5-48
5.71.	Static Pressure (psi) Contours at $t = 5.0 \times 10^{-3}$ Seconds	5-49
5.72.	Static Pressure (psi) Contours at $t = 6.0 \times 10^{-3}$ Seconds	5-49
5.73.	Surface Static Pressure (psi) Contours at $t = 2.0 \times 10^{-3}$ Seconds . .	5-50
5.74.	Surface Static Pressure (psi) Contours at $t = 3.0 \times 10^{-3}$ Seconds . .	5-51
5.75.	Surface Static Pressure (psi) Contours at $t = 3.3 \times 10^{-3}$ Seconds . .	5-51
5.76.	Surface Static Pressure (psi) Contours at $t = 3.5 \times 10^{-3}$ Seconds . .	5-52
5.77.	Surface Static Pressure (psi) Contours at $t = 3.7 \times 10^{-3}$ Seconds . .	5-52
5.78.	Surface Static Pressure (psi) Contours at $t = 4.0 \times 10^{-3}$ Seconds . .	5-53
5.79.	Surface Static Pressure (psi) Contours at $t = 4.5 \times 10^{-3}$ Seconds . .	5-53
5.80.	Surface Static Pressure (psi) Contours at $t = 5.0 \times 10^{-3}$ Seconds . .	5-54
5.81.	Surface Static Pressure (psi) Contours at $t = 6.0 \times 10^{-3}$ Seconds . .	5-54

List of Tables

Table		Page
4.1.	Mach Numbers and Corresponding Velocities Modeled	4-18
4.2.	Mesh Adaptations and Threshold Values Used	4-23
4.3.	Final Properties of Adapted Meshes	4-24
5.1.	Computation Time	5-2
5.2.	Parallel Computation Times	5-3
5.3.	Summary of Analytic Results for $M_\infty = 3.0$ in Air	5-7

List of Symbols

Symbol	Page
\mathbf{Q} , vector of primitive variables	2-1
\mathbf{E} , flux vector in x -direction	2-1
\mathbf{F} , flux vector in y -direction	2-1
\mathbf{G} , flux vector in z -direction	2-1
x , coordinate in x -direction	2-1
y , coordinate in y -direction	2-1
z , coordinate in z -direction	2-1
t , time	2-1
ρ , density	2-2
u , velocity component in the x -direction	2-2
v , velocity component in the y -direction	2-2
w , velocity component in the z -direction	2-2
e_t , total energy	2-2
p , pressure	2-2
γ , ratio of specific heats	2-2
e , internal energy	2-2
T , temperature	5-4
M , Mach number	5-4
R , specific gas constant	5-4
ft , feet	5-4
lb_f , pounds-force	5-4
lb_m , pounds-mass	5-4
Pa , Pascal (N/m^2)	5-4

List of Abbreviations

Abbreviation	Page
HSTT, High Speed Test Track	1-1
SRR, Super Road Runner test sled	1-1
O/U, Over/Under	1-1
fps, feet per second	1-3
CFD, computational fluid dynamics	1-4
GUI, graphical user interface	1-5
PDE, partial differential equation	2-1
2D, two-dimensional	2-4
3D, three-dimensional	2-4
CDDL, Computational Dynamics and Design Laboratory	3-1
AFIT, Air Force Institute of Technology	3-1
SGI, Silicon Graphics, Incorporated	3-1
MHz, megahertz (10^3 hertz)	3-1
MB, megabyte (10^3 bytes)	3-1
RAM, random access memory	3-1
CPU, central processing unit	3-1
GHz, gigahertz (10^6 hertz)	3-1
AMD, Advanced Micro Devices	3-1
GB, gigabyte (10^6 bytes)	3-1
SMP, Symmetric Multi-Processor or Shared Memory	5-3

Abstract

The flow field about the nose section of a hypervelocity test sled is computed using computational fluid dynamics. The numerical model of the test sled corresponds to the Nike O/U narrow gage sled used in the upgrade program at the High Speed Test Track facility, Holloman Air Force Base, New Mexico. The high temperatures and pressures resulting from the aerodynamic heating and loading affect the sled structure and the performance of the vehicle. The sled transitions from an air environment to a helium environment at a speed of approximately 3,300 feet per second (Mach 3 in air, Mach 1.02 in helium) to reduce the effects of high Mach number flows. Steady, three-dimensional, inviscid flow solutions are computed for Mach numbers of 2 and 3 in air (2,200 and 3,300 feet per second), and for Mach numbers of 1.02, 2.5 and 3.1 in helium (3,300, 8,076 and 10,000 feet per second). Mesh adaptation is used to obtain a mesh-independent solution. Second-order solutions are obtained for the Mach 3 in air and Mach 1.02 in helium cases. The unsteady transition from air to helium at 3,300 feet per second is also modeled. Mach 3 in air computations are compared with analytical results.

COMPUTATIONAL AERODYNAMIC ANALYSIS OF THE FLOW FIELD ABOUT A HYPERVELOCITY TEST SLED

I. Introduction

Background

Hypersonic flight conditions are difficult to replicate without undergoing actual flight testing. Since flight testing can be expensive and dangerous, other methods are sought to simulate flight test conditions for hypersonic vehicle systems. One such method is the ground test facility at the High Speed Test Track (HSTT) at Holloman Air Force Base, New Mexico. Several types of tests are performed at this facility, including “missile impact and penetration tests, interceptor tracking tests, material erosion and ablation tests, aircrew escape system tests, submunition dispenser tests, and tests of inertial guidance systems” (8:1). The test article is accelerated by a solid rocket booster while riding on parallel steel crane rails that are approximately 10 miles long.

Figure 1.1 shows one configuration of the hypervelocity sled being developed, called the Super Road Runner (SRR), during an experimental run. The structure of the SRR sled is essentially the same as the Nike O/U Narrow Gage sled modeled in this study; the main difference between the two being the rocket motors used. The sled is attached to the rails by slippers, which wrap around the rails (Figure 1.2), with a small gap (initially 0.125 inches) between the rail and the slipper. The gap is necessary due to differences in manufacturing tolerances for the separate sections of track.

As the sled is accelerated to hypersonic speeds, the sled’s supporting structure is subjected to severe vibrations due to imperfections in the alignment of the parallel rails, as well as unsteady aerodynamic effects. Occasional severe metal-to-metal contact occurs as the vibrations “bounce” the sled within the constraints of the slipper-rail gap. This contact causes rail damage, known as gouging, which was studied recently by Laird (14). Severe

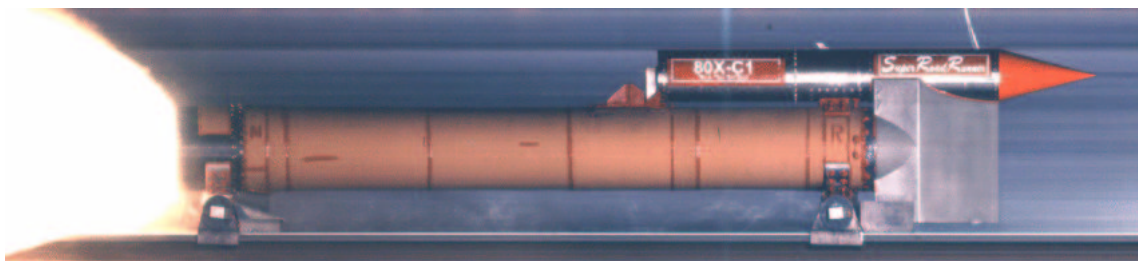


Figure 1.1 Super Road Runner (SRR) Narrow Gauge Sled



Figure 1.2 Slipper and Rail Configuration (14:3)



Figure 1.3 SRR Sled at 4,865 fps in Air (Mach 4.3)

aerodynamic heating and loading at hypersonic speeds worsen the structural difficulties. Figure 1.3 illustrates some of the erosive effects encountered during test runs.

During the latter portions of the run, when hypersonic effects would be encountered in air, the sled is run through a helium environment. Because the speed of sound is higher in helium than in air, the Mach number is reduced while maintaining a constant ground speed. This effectively reduces the aerodynamic and aerothermal effects. Due to the reduction in Mach number, the sled does not experience typical hypersonic phenomena during acceleration to terminal test velocity. For this reason the sled is termed a *hypervelocity* rather than a *hypersonic* vehicle in this study.

Current sled designs support test velocities of approximately 8,900 feet per second (fps). The goal for an upgraded design currently in development is to deliver payloads at velocities approaching 10,000 fps (3:1). A successful upgrade design requires detailed knowledge of the flow field properties as the sled accelerates to mission speeds, and as it traverses the air and helium environments. Specifically, knowledge of the pressure field allows accurate prediction of the aerodynamic drag, which allows proper sizing of the rocket engines required to attain the final test velocity; and temperature data assist in designing a slipper-rail system that resists damage due to gouging effects.

Previous Work

Current sled designs are based on empirical methods developed after years of running different sled configurations at the HSTT. Most new designs do not differ significantly from previous designs, allowing the use of earlier experimental data. However, for the design of a significantly different sled, trial runs are necessary to experimentally determine performance data (19:3-4).

All sled configurations designed and used since the test track was initially developed in the 1950's and 1960's have been analyzed using theoretical methods (such as compressible flow dynamics to determine shock angles, pressures, etc.) and wind-tunnel testing. Static force tests of early dual rail and monorail sleds were conducted in the von Karman Gas Dynamics Facility at Arnold Engineering and Development Center (10). However,

since the design of the current sled is considerably different than those modeled previously, the earlier wind-tunnel test results are not very useful and are not expected to be duplicated in this study.

The technical development of monorail variants is reported by Krupovage and Rasmussen (13). They discuss solutions to several aerodynamic, structural and thermodynamic problems to achieve stability control and reduce thermodynamic heating. Korkegi and Briggs (12, 11) analyzed the flow between the rail and the slipper of a generic sled using a simplified, two-dimensional approach. They assumed that the flow through the slipper gap was shock-compressed through a normal (bow) shock off the slipper, and that the boundary layer rapidly expands to fill the entire gap. Their analysis shows that the flow is essentially like a supersonic nozzle; the flow accelerates to supersonic speeds at the entrance to the gap and then, through expansion, the pressure decreases toward the end of the gap (11:34-36).

As noted before, the current sled design is fairly recent (within the last five years); the research cited above was finished almost 40 years previously. The Nike sled configuration has been run experimentally only once, and no aerodynamic data were taken. An early draft report by Myers (15) gives brief aerodynamic estimates for pressure, temperatures and Mach numbers for $M_\infty = 2.0$ in air in several regions of interest about the Nike sled configuration.

The “Virtual Wind-Tunnel”

Hypersonic wind-tunnels are very difficult and expensive to design, build and operate and, therefore, very few even exist. An alternative to in-flight or wind-tunnel testing of any hypersonic vehicle is to run computational simulations in so-called “virtual wind-tunnels,” or computational fluid dynamic (CFD) simulations on high-performance computing platforms.

Several years ago, CFD methods were in their infancy and their use was typically restricted to research specialists. Combined with computational hardware limitations, this meant that any computational modeling of a fluid flow was expensive and labor intensive.

Mesh generation was particularly troublesome and time consuming (and, to an extent, remains so today). Many of the CFD codes in use required expertise in the numerical methods used to obtain accurate and stable solutions. Computational models used many simplifications so that solutions could be obtained in reasonable times.

Today, however, advances in computer hardware and the development of robust commercial software packages have brought the use of CFD more into the mainstream of engineering science. Highly sophisticated graphical user interfaces (GUIs) allow relative ease of use. Robust algorithms for accurate and stable flow modeling don't require as much specialization as before. High-end computer workstations and low-cost supercomputing clusters provide enough computing power to solve fairly complex flows (including three-dimensional, viscous flows that take into account chemical reactions) in a reasonable amount of time.

The ability to simulate hypersonic flows is particularly enticing. CFD simulations are not subject to experimental inaccuracies, and, because of the deterministic nature of computers, experimental results are easily duplicated by simply matching the input conditions. Flow conditions that would be too dangerous or even impossible to replicate in a wind-tunnel are readily simulated. The number of expensive flight tests can be reduced by obtaining accurate CFD results to improve a design virtually.

Notwithstanding the positive aspects of CFD simulations, there still remain many caveats. Despite the advancements with user interfaces and software packages, CFD is still the work of specialists. Mesh generation is also very much an art, rather than a pure science. Many solver packages require additional knowledge about the various models so the user can choose options intelligently.

There are also doubts about the accuracy of CFD simulations. Much work has been put into defining what is known as validation (solving the right equations) and verification (solving the equations right). That is, whether or not the computational model does, in fact, model real, physical flows. The age-old adage of computer programming "garbage in, garbage out" still applies; CFD results are only as good as the computational models used to obtain them. Each new code written must be verified by comparing the CFD solutions to

experimental data and theoretical solutions. Further flight-testing or wind-tunnel testing is almost always needed to validate each solution before using the CFD code for design or virtual testing.

Despite these challenges, the “virtual wind-tunnel” remains a cost-effective alternative to in-flight and wind-tunnel testing. Current research is constantly improving the state-of-the-art; CFD simulations can only get better.

Research Objectives and Scope

The objective of the current research is to simulate the flow about the nose section of a hypersonic test sled using commercially available software packages. The temperature and pressure data obtained are used to support current redesign efforts at the HSTT. The flow surrounding the nose section is extremely complex, with many shock-shock interactions, shocks impinging on structural surfaces, reflected shocks from ground effect, possible high-temperature effects, etc.

The solutions contained herein were obtained for flight conditions similar to test sled experiments currently being planned. The sled transitions from an air environment to a helium environment at approximately 3,300 fps ($M_\infty = 3.0$ in air). In this study inviscid, three-dimensional solutions were obtained for Mach numbers of 2 and 3 in air (velocities of 2,200 and 3,300 fps), and Mach numbers of 1.02, 2.5 and 3.1 in helium (velocities of 3,300, 8,076 and 10,000 fps). The unsteady transition between air and helium was also modeled at a velocity of 3,300 fps.

Although robust commercial CFD software packages with user-friendly GUIs are available to reduce the burden of a CFD analysis, there is still considerable effort required to learn how to use these packages sufficiently well to obtain accurate and stable solutions. Therefore, a secondary objective of the current research was to evaluate and gain experience with a suite of commercially available software packages suitable for computational aerodynamic analysis.

II. Computational Fluid Dynamics General Theory

The computational analysis of a fluid flow requires an understanding of the general area of computational fluid dynamics and its application to aerodynamic problems. A typical CFD analysis goes through a series of distinct steps. Here these steps are given in the order in which they are performed by the analyst:

- Pre-Processing (Mesh Generation) – the surfaces of the object of interest and the space around the object (for an external flow) are discretized into a series of grid points, or nodes. This is similar to the placement of probes in a wind-tunnel experiment.
- Processing (Numerical Computation) – this step includes initializing the flow solver options to correctly interpret boundary and initial conditions. The solver then computes the flow properties desired at each mesh node.
- Post-Processing (Flow Visualization and Analysis) – once the flow properties have been computed, the resulting solution is analyzed for relevant trends or relations using software generally known as scientific visualization tools. Additionally, the computed solution may be compared to theoretical or experimental results for validation exercises.

This chapter discusses each of these general steps in the CFD process in more detail, although not necessarily in the same order.

Equations of Fluid Flow

The physics of a three-dimensional, inviscid flow are described by three sets of partial differential equations (PDEs). These equations describe the conservation of mass, the conservation of momentum and the conservation of energy. These equations are known as the Euler equations and are written here in the flux vector form (6:98)

$$\frac{\partial \mathbf{Q}}{\partial t} + \frac{\partial \mathbf{E}}{\partial x} + \frac{\partial \mathbf{F}}{\partial y} + \frac{\partial \mathbf{G}}{\partial z} = 0 \quad (2.1)$$

where

$$\mathbf{Q} = \begin{bmatrix} \rho & \rho u & \rho v & \rho w & \rho e_t \end{bmatrix}^T$$

$$\mathbf{E} = \begin{bmatrix} \rho u \\ \rho u^2 + p \\ \rho uv \\ \rho uw \\ (\rho e_t + p) u \end{bmatrix}, \quad \mathbf{F} = \begin{bmatrix} \rho v \\ \rho vu \\ \rho v^2 + p \\ \rho vw \\ (\rho e_t + p) v \end{bmatrix}, \quad \mathbf{G} = \begin{bmatrix} \rho w \\ \rho wu \\ \rho wv \\ \rho w^2 + p \\ (\rho e_t + p) w \end{bmatrix}$$

This set of equations is not a closed set; generally, the ideal gas law is chosen to close the set and make the system mathematically well-posed. The ideal gas law can be written in the following form

$$p = \rho e(\gamma - 1) \quad (2.2)$$

The Euler equations are restricted to flows where the viscous effects are negligible. Examples are the computations to determine the lift and drag (due to pressure) on an airfoil. Since boundary layer theory indicates that the pressure gradient normal to the surface through the boundary layer is negligible, the inviscid flow field outside the boundary layer can be computed and the resulting pressure distribution approximates the actual pressure fields with reasonable accuracy. However, inviscid results are not valid for separating flows, and may predict negative pressures in such cases.

Finite Volume Method

Digital computers cannot solve partial differential equations that describe continuous physics as shown above. Instead, the equations must be *discretized* and put into an algebraic form. Current methods can be categorized into three methods: finite-difference, finite-volume and finite-element. The finite-volume method will be discussed here.

If the Euler equations are written in integral form for arbitrary control volumes, the resulting method is known as a finite-volume method. The Euler equations can then be written as

$$\iiint_V \left(\frac{\partial \mathbf{Q}}{\partial t} \right) dx dy dz = - \iiint_V \left(\frac{\partial \mathbf{E}}{\partial x} + \frac{\partial \mathbf{F}}{\partial y} + \frac{\partial \mathbf{G}}{\partial z} \right) dx dy dz \quad (2.3)$$

where the volume integral is computed over each individual cell.

A finite-volume method does not require a regular, rectilinear (or curvilinear) domain on which to solve the conservation equations, as would be required with a finite-difference method. There is a large variety of shapes that can be used for the cell volumes, allowing great flexibility in generating a mesh. This allows the modeling of complex geometries with irregularly shaped cells. The effort required to generate a mesh for a finite-volume solver is usually much less than that required to generate a structured mesh for the same problem. Additionally, the laws of conservation do not need to be explicitly specified for the entire domain, since they are specified in the form of the integral equations for each individual cell volume.

Discretization of the Domain of Interest–Mesh Generation

As mentioned, computers cannot solve the continuous equations and they must be discretized. The flow field of interest must also be discretized, or covered with a mesh or grid (the terms can be used interchangeably) of node points. Current CFD technology uses two types of meshes, structured and unstructured.

Structured. Structured grids are distinguished by having a rectangular *computational* (versus *physical*) domain, with the interior nodes being distributed along distinct grid lines (7:358). The neighboring nodes of any particular node are implicitly defined by the indices of those nodes. For example, the neighboring nodes of a node with indices i, j are $i+1, j$, $i-1, j$, $i, j-1$, etc. Unless the physical domain is also rectangular, the physical domain must be mapped to the computational domain through a transformation for use in a finite-difference solver. No such transformation is required with a finite-volume solver. Structured grids can be used with finite-difference or finite-volume solvers.

Unstructured. Unstructured meshes can be defined as one where the nodes cannot be associated with regular grid lines (7:359). The elements of an unstructured

mesh can be any geometric shape. Typically, 2D meshes use triangles or quadrilaterals and 3D meshes use tetrahedrons and pyramids (6:356). Each node's neighbors cannot be determined simply by looking at the indices of the nodes, so additional memory is consumed (relative to a structured mesh with an equal number of nodes) to hold node-to-cell mappings. Since the mesh is constructed in the physical domain itself, no coordinate transformations are needed. Unstructured meshes cannot be used with finite-difference solvers.

Solution Accuracy

Again, physical flow phenomena are continuous in nature, while the solutions obtained using CFD methods are obtained for discrete points. Therefore, errors are present in the CFD solutions that must be taken into consideration. Many errors such as truncation error (from the discretization technique used) and machine round-off error contribute to the overall error of the solution. Active research is being conducted in areas to improve the accuracy of solutions (while maintaining numerical stability). This section discusses some of the important issues related to solution accuracy.

Validation and Verification. The credibility of any computational simulation must always be addressed. To assist CFD analysts in quantifying “error and uncertainty in computational simulations,” a process known as *Validation and Verification* has been advanced by many CFD researchers and organizations. These two words are not synonymous; they both refer to two distinct parts of the process. The definitions given here are not universally accepted, but they seem to be emerging as the standard. The *Guide for the Verification and Validation of Computational Fluid Dynamics Simulations* published by the American Institute of Aeronautics and Astronautics defines Verification as “the process of determining if a computational simulation accurately represents the conceptual model, but no claim is made of the relationship of the simulation to the real world.” Validation is defined as “the process of determining if a computational simulation represents the real world.” In other words, verification is determining if the computational simulation

is solving the correct equations (and with the correct order of accuracy), while validation is ensuring that a physically possible (and correct) solution is obtained (5:1).

Although the present research has been conducted with commercially-available, verified software, there are pitfalls to blindly accepting the results of such software. As Roache states in his treatise on validation and verification, “the user must have confidence that the numerical methods as described in the manuals are actually those implemented in the code” and that

CFD algorithm developers have long known that there is a trade-off between code robustness and accuracy, and CFD code marketers know that there is little market for numerical accuracy but much demand for bullet-proof code robustness. General purpose CFD codes must be treated with skepticism in any new application by any conscientious user” (18:10-11).

Due to the lack of experimental data for the Nike sled configuration, the computational solutions presented in this study can only be compared to relatively simple analytical solutions.

Mesh Independent Solutions. The accuracy of any CFD simulation is highly dependent on the mesh used. If there is too little resolution in terms of the number of nodes to adequately resolve flow features such as shock waves, the solution will be in error. In addition, too many nodes can negatively impact the computational efficiency. The ideal mesh would be refined enough to capture all flow features and yet be as coarse as possible so as to consume less computational resources. A grid-convergence study in which the grid spacing is systematically reduced until the solution no longer changes can be conducted to find such a grid. Grid convergence studies are typically conducted with structured meshes where increasing or decreasing mesh resolution is straightforward.

Mesh Adaptation. Mesh adaptation is a method whereby highly accurate meshes can be obtained while retaining computation efficiency. The idea behind adaptations is to obtain a highly accurate solution while minimizing the total number of mesh points used. This is accomplished in two ways; the existing nodes can be redistributed, or more nodes can be added in order to minimize the errors over the entire flow domain. As more node points are added, the global error is reduced. Optimizing the number and lo-

cation of additional nodes requires knowing the locations of the maximum errors, which is impossible without knowing the exact solution. “Therefore, most adaptive methods rely on estimating the behavior of the error using feature-detection algorithms. These algorithms assume regions of high error are associated with regions of high gradients” (22:4). In CFD applications, this assumption that the highest errors are in the regions of highest gradients has been proven to be reliable in the resolution of certain flow features, although there is no guarantee that adapting to high-gradients will improve the accuracy (22:5). Nonetheless, mesh adaptation remains the best method available to improve the accuracy of solutions while maintaining computational efficiency, especially for unstructured meshes (in which case it is arguably as good as, if not better than, a traditional grid convergence study). In this study, mesh adaptations were performed to obtain mesh-independent solutions.

First- and Second-Order Accuracy. The accuracy of a numerical simulation is also affected by the order of accuracy of the discretization method used (both temporally and spatially). The order of the method can be determined by looking at the order of the dominant truncation error term; a second-order derivative in the error term indicates a first order solution while a third-order derivative indicates a second-order solutions, etc. The order of a method determines the effect of dispersion and dissipation errors on the solutions. For example, a second-order method will usually be dominated by dispersion error; that is, solution gradients increase, and artificial oscillations can be introduced. First order methods are usually dominated by dissipation error, where the gradients are “smeared” out. This dissipation effect can be attributed to second-order error terms that resemble viscosity terms. For this reason, they are known as “artificial viscosity” terms.

Second-order methods resolve gradients much better than first-order methods; shocks and other discontinuities tend to be more defined. For this reason, second-order methods are preferred in CFD. However, the dissipation errors associated with second-order methods have a tendency to be numerically destabilizing. This can be remedied with the use of explicit artificial viscosity or limiters. Limiters put limits (obviously) on certain flow quantities such as temperature or pressure, and so assist in maintaining stability—but this increase in stability can adversely affect the convergence rate of the solution.

Time Accurate Solutions

Solutions for steady flows can be obtained by simply dropping the time-dependent term in Equation (2.1). A steady solution can also be obtained by integrating the governing equations in time and driving the time derivatives to zero. Although these solutions use a time step, any intermediate solutions obtained are not necessarily time-accurate because different time steps can be used for each cell in the flow domain. This procedure is known as local time-stepping and is frequently used to increase the convergence rate while maintaining stability. This is possible by decreasing the time step in areas or cells of decreased stability, while maintaining a larger time-step in solution areas that are more stable. Time accurate solutions are obtained in a similar manner as steady solutions, with the exception that a global time step is used. If starting from a physically correct initial state, the intermediate solutions are also physically correct.

III. Computational Facilities

The research presented here was accomplished using the computational facilities of the Computational Dynamics and Design Laboratory (CDDL) of the Department of Aeronautics and Astronautics, Graduate School of Engineering and Management, Air Force Institute of Technology (AFIT). This chapter presents a brief overview of the hardware and software used during the study.

Hardware

Early mesh generation was accomplished on an SGI Octane2 V6 running IRIX64. The SGI has dual MIPS R12000A processors running at 360 MHz and has 512 MB of RAM. Early CFD solutions were obtained on Compaq XP1000 professional workstations running Tru64 UNIX. Each workstation has an Alpha CPU running at 1 GHz and 512 MB of RAM. Later solutions were obtained on a 16-node Beowulf class supercomputing cluster, running Redhat Linux 7.1. Each node consists of two 1.4 GHz AMD Athlon CPUs, 512 MB of RAM and 20 GB of disk space. Some post-processing and some mesh generation was accomplished on a high-end Dell Precision 530 workstation running Redhat Linux 7.2. This graphics workstation has dual 1.4 MHz Pentium 4 Xeon processors, 512 MB of RAM and 37 GB of disk space; it is configured as an access terminal to the Beowulf cluster. Additional post-processing was accomplished on a Dell Precision 530 workstation running Microsoft Windows 2000 Professional. The Windows machine has dual 1.7 MHz Pentium 4 Xeon processors and 512 MB of RAM.

Software

All software used for the mesh generation, flow simulation and post-processing is commercially available. A brief overview of the software packages and their features is given here.

Gridgen. The meshes used were generated with Gridgen Version 13.3 (on both the SGI and Linux workstations). Gridgen supports structured, unstructured and hybrid meshes 17). User input is accomplished through a fairly intuitive GUI.

FLUENT. Solutions were computed with FLUENT Version 5.5.14 (on the Compaq Alpha workstations) and FLUENT Version 6.0.12 (on the Linux cluster). FLUENT is a general purpose, finite-volume solver; as such, structured and unstructured meshes can be used. Options are available for several different discretization schemes, including first- and second-order upwinding. Mesh adaptation using gradients (among other options) is available to refine or coarsen the mesh (4).

Tecplot. Post-processing was done with Tecplot Version 9.0.2. FLUENT data can be imported using the FLUENT Data Loader add-on, or by exporting the data from FLUENT in Tecplot format. However, the FLUENT data exporter does not write the data in a volume mesh format, so several features of Tecplot (such as iso-surfaces and 3D slices) are not available. CFD-Analyzer is another add-on available for Tecplot that allows the computation of several CFD quantities (such as Mach number), the integration of scalars and vectors along lines, over surfaces and through volumes, the visualization of particle paths and streaklines as well as error analysis (order of accuracy) (1, 2).

IV. Numerical Simulation

This chapter discusses the setup of the computational problem, including mesh generation, flow solver initialization and flow solution.

Inviscid, Steady

Inviscid solutions were obtained for Mach numbers of 2.0 and 3.0 (2,200 and 3,300 fps) in air; and 1.02, 2.1 and 3.10 (3,300, 8,075 and 10,000 fps) in helium. This simulates an actual test run that transitions from air to helium at about 3,300 fps and continues to accelerate to the goal of 10,000 fps in the helium environment. After reaching the top speed required for the test (shown here as 10,000 fps), the actual sled leaves the helium environment and returns to the air environment. Figure 4.1 illustrates the experimental run trajectory, as well as the actual flow conditions modeled in this study. As mentioned previously, the sled transitions from an air environment to a helium environment at about 3,300 fps.

Mesh Generation. Thompson (20) described mesh generation as a “major pacing item (THE major pacing item were it not for turbulence)” in current CFD methods. Many industry experts have complained that the majority of the work in obtaining a CFD solution is expended in the generation of the mesh. This bottleneck in productivity has been eased somewhat for initial meshes through the use of GUIs. However, GUIs “are of little or no use to a designer who needs to repeatedly mesh and solve on a series of similar geometries” (20). One feature that is often overlooked in mesh generation packages is a non-interactive scripting capability that could be used to batch process many different configurations of one design.

This trend is also illustrated in the current research; a vast majority of the time spent was on mesh generation. So much time was spent constructing the initial mesh (and refining it along the way), that no design iterations were possible for this study.

Model Geometry. The initial model geometry was obtained from technical drawings (9) of the Nike O/U Hypersonic Upgrade narrow gage rail sled that is currently

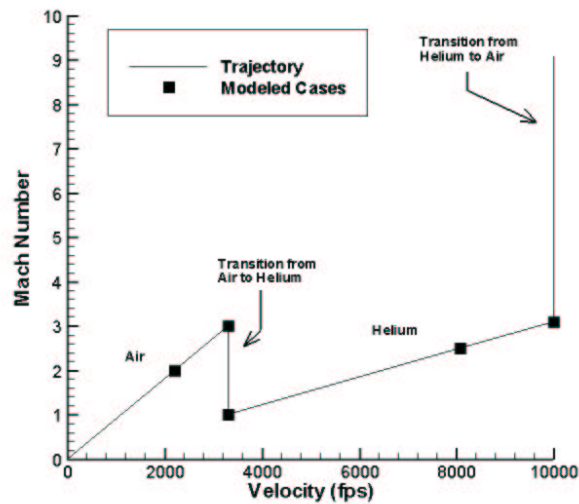


Figure 4.1 Experimental Sled Run Trajectory and Corresponding CFD Cases Modeled

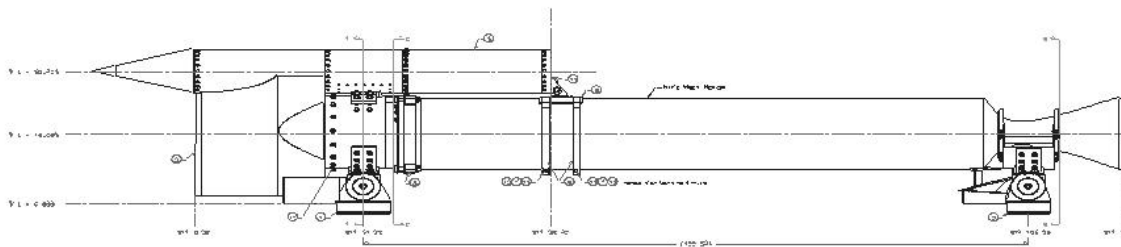


Figure 4.2 Technical Drawing of Nike O/U Sled

under development at the HSTT of Holloman AFB, NM. Figures 4.2-4.6 show portions of the technical drawings from which the geometry details were extracted. A side view of the entire sled, consisting of a payload section, several wedges to divert the flow around structural components (part of forward and rear structural assemblies) and the solid rocket engine, is shown in Figure 4.2. Figure 4.3 gives a more detailed view of the front portion that was actually modeled, still from the side. Figure 4.4 is a cut-away view; the cut-away plane is shown as a broken line in Figure 4.3 (the plane cuts through the slipper wedge). The front assembly is shown in Figures 4.5-4.6.

The payload modeled is a cylinder-cone combination that sits at the top of the sled. The cone half-angle is 15° and its length is 19 inches (giving a cylinder diameter of

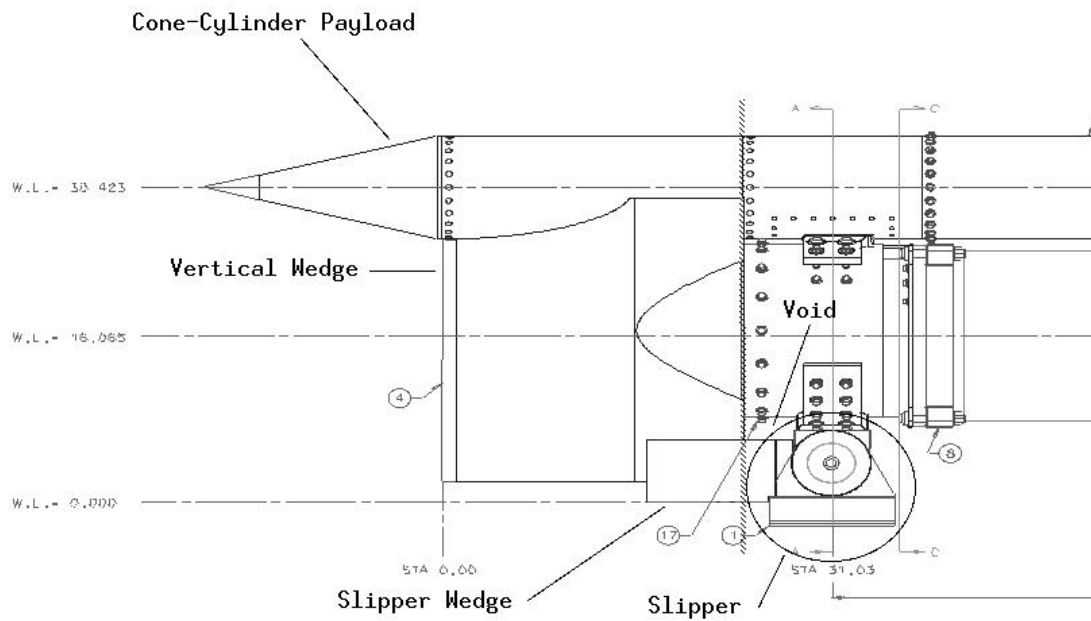


Figure 4.3 Modeled Nose Portion of Sled

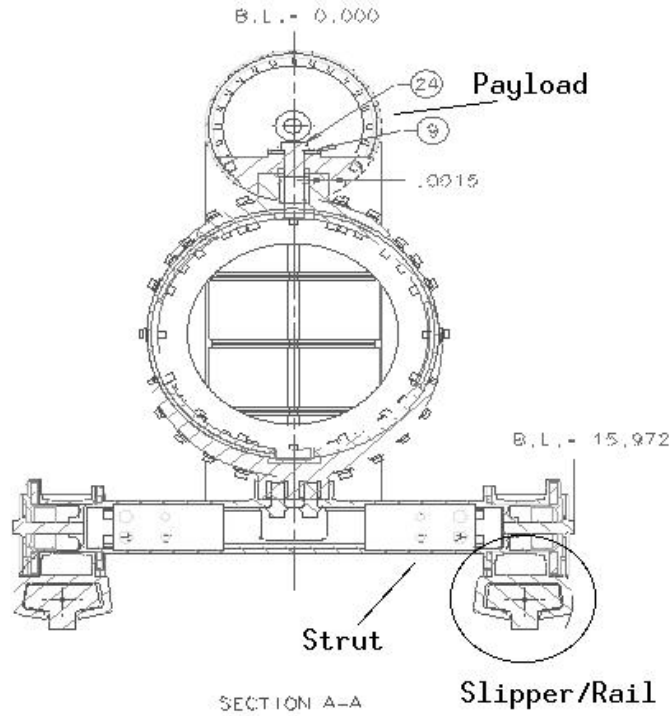


Figure 4.4 Forward Assembly Cut-Away View, Looking Forward

above the horizontal strut (Figure 4.3). The flow would surely separate when hitting this void, causing numerical difficulties.

The rail was modeled as a rectangular block with rounded upper edges. Although the actual slipper/rail gap is not modeled, the gap between the slipper wedge and the rail is assumed to be the same height as the slipper/rail gap, which was modeled as 0.125 inches. The initial gap of the sled is about 0.065 inches all around the slipper. During tests, the slipper material erodes and the gap can range from 0 to 0.125 inches and more. The height of the rail is 6 inches.

The following coordinate definitions were used: x is positive in the flow direction with $x = 0$ being the cone-cylinder intersection; y is positive up, with $y = 0$ at the lower surface of the small slipper-wedge; z is positive toward the outboard side of the sled (the direction in which the strut extends), with $z = 0$ being at the symmetry plane.

Domain Boundaries. Since flow cannot propagate upstream in supersonic flows, it is unnecessary to model a large amount of the flow field upstream of the model. The minimum x distance was set to be at -100 inches (about 80 inches upstream of the cone point). The maximum y and z distances were chosen based on the expected shock angle. For all freestream Mach numbers, it is desired that any shocks propagate out through the outflow domain to keep the boundary conditions constant at freestream conditions for the forward domain. The maximum shock angle was obtained from Chart 5, NACA Report 1135 (16:48), for the $M_\infty = 1.02$ in helium case. For $M_\infty = 1.02$ around a cone with a half-angle of 15° , the shock angle is $\theta = 75^\circ$. This is simply an estimate since the chart used is for $\gamma = 1.405$ while helium has $\gamma = 5/3$. This shock angle gives a minimum y_{max} of 160 inches for the shock to exit out of the backplane. The value chosen was $y_{max} = 185$ inches to be conservative. Due to the height of the rail (6 inches) and the gap height (0.125 inches), y_{min} was -6.125 inches. The outer domain in the z -direction was found by rotating the y boundary about the $z = 0$ axis, giving $z_{max} = 191.125$ inches. Figure 4.7 shows each of the different boundary zones in the computational model. The individual faces that comprised the model of the domain of interest were divided into six zones: pressure-far-field, pressure-outlet, symmetry, ground, rail and body.

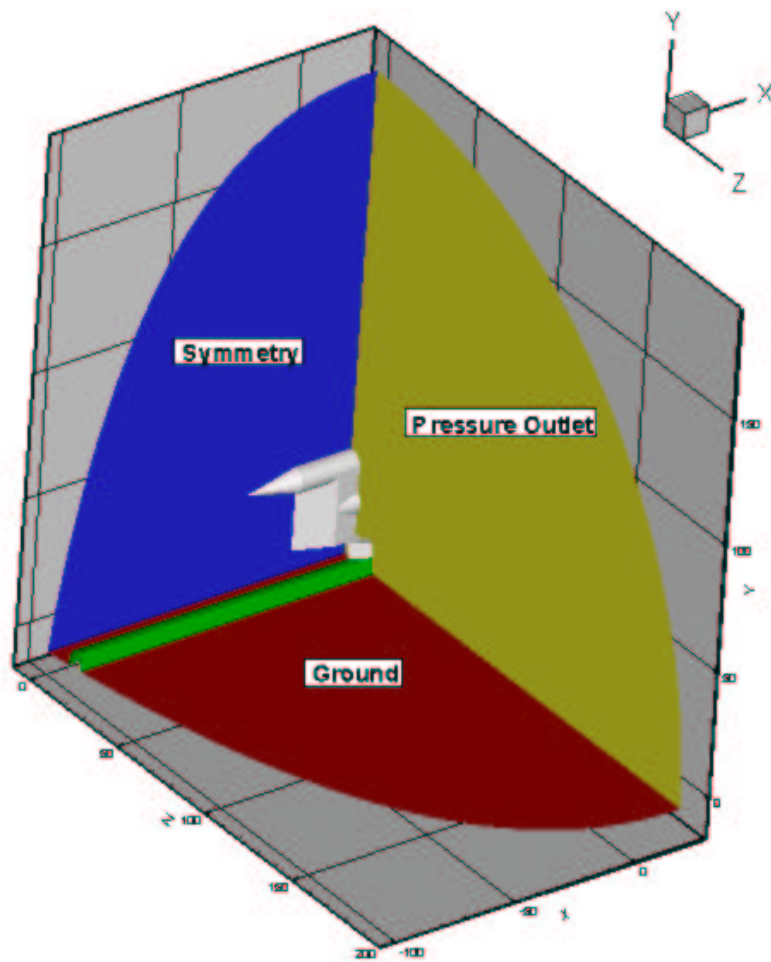


Figure 4.7 Modeled Domain Boundaries

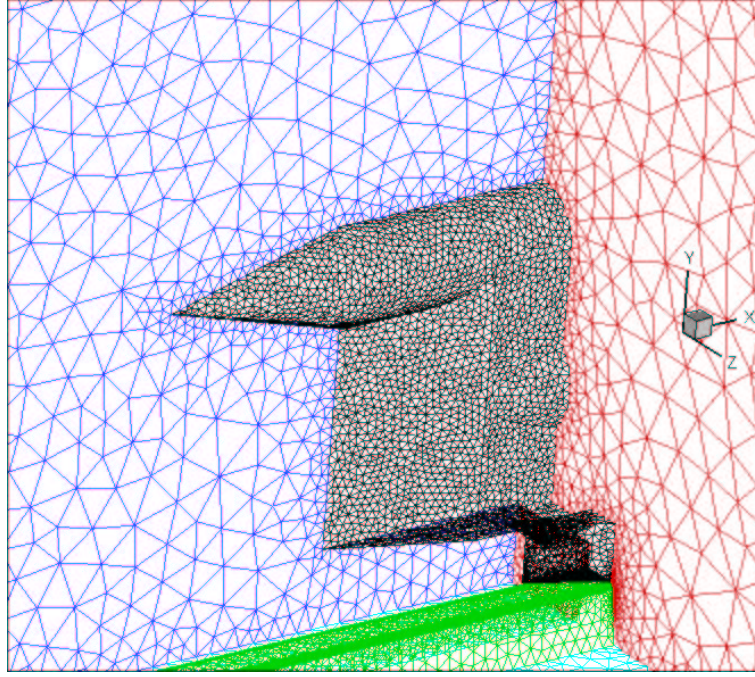


Figure 4.8 Initial Surface Mesh

Mesh Solver Options. The initial mesh was generated using equal spacing of the nodes along all edges, with the exception of the rail and the lower surface of the slipper wedge. The rounded edges of the rail were meshed using a finer, structured mesh to preserve the curvature. The rectangular cells were converted to triangles by triangulating along one horizontal.

The node spacings along the sled body edges were ~ 1 inch (Figure 4.8), and those along the outer boundaries were ~ 5 inches. Average node spacing along the rail and the lower surface of the slipper wedge in the vicinity of the gap was ~ 0.2 inch. Default values for the unstructured mesh solver were used to generate the surface meshes and the interior volume mesh. The initial mesh consisted of 271,038 tetrahedral cells, with 527,668 triangular faces and 52,261 nodes.

Mesh Quality. As mentioned previously, the quality of a mesh can significantly influence the quality and stability of the computational solution. In spite of this fact, very little emphasis was placed on the importance of mesh generation during this research as it was believed the default options on the mesh solver were sufficient to

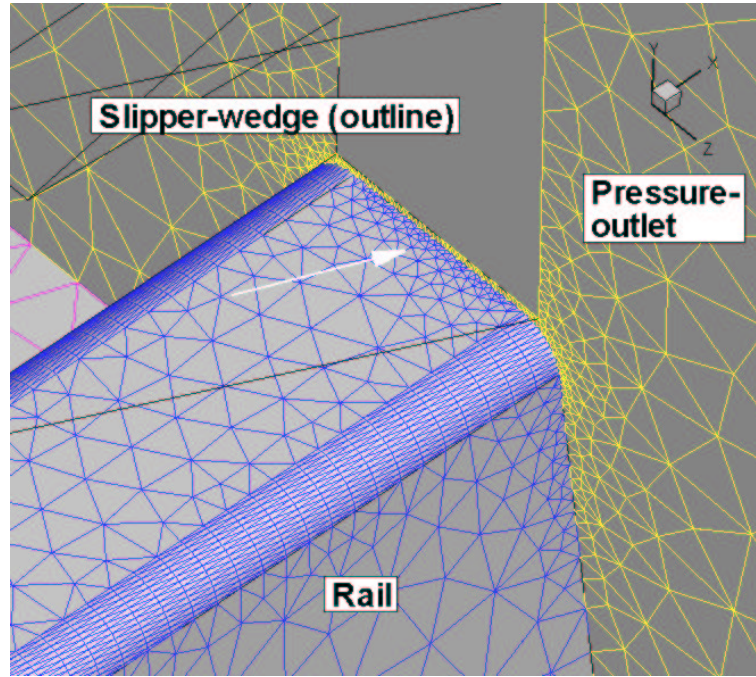


Figure 4.9 Initial Mesh on Rail Surface Near Slipper/Rail Gap

generate a reasonable mesh. Toward the conclusion of the project, several trouble spots in the original mesh were recognized that may have prevented the obtaining of well-converged solutions.

The area that is the most critical in terms of mesh generation is the gap between the slipper wedge and the rail. Figure 4.9 shows the initial mesh in the area in question; and Figures 4.10-4.11 show the same area after being adapted for the $M_\infty = 3.0$ in air and $M_\infty = 1.02$ in helium cases, respectively. The main problem with the mesh, as seen in Figure 4.9 is the node spacings along the surfaces of the rail. The node spacings along the upper surface of the rail in the z -direction at the outflow plane are sufficiently small (white arrow in the figures). This was intended to increase the resolution of the mesh along the top surface of the rail inside the gap. However, the boundary node spacings did not propagate into the rest of the surface mesh as expected. After adaptations, though, especially in the $M_\infty = 3.0$ in air case as seen in Figure 4.10, the spacing along the top surface are improved, due to the high gradients present.

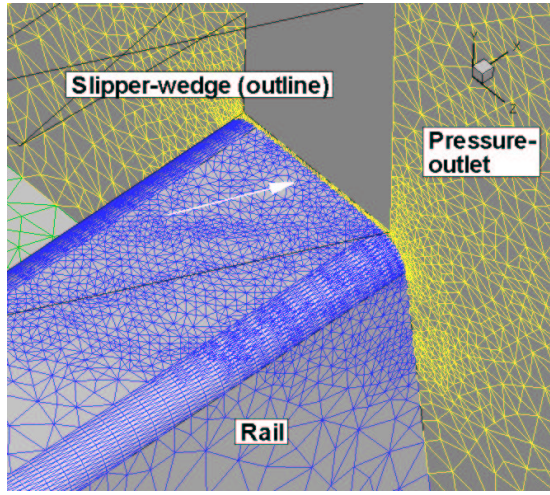


Figure 4.10 Final Mesh on Rail Surface
($M_\infty = 3.0$ in Air)

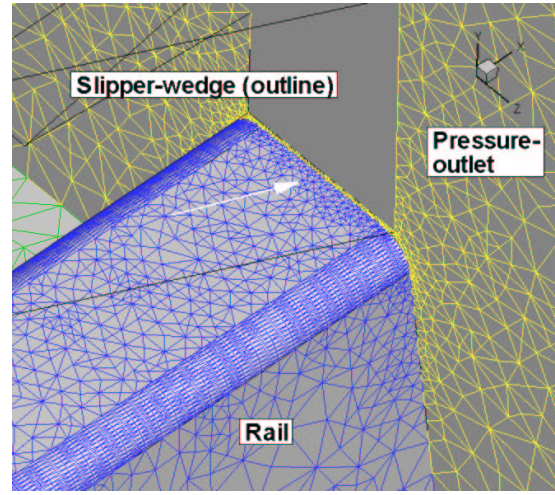


Figure 4.11 Final Mesh on Rail Surface
($M_\infty = 1.02$ in Helium)

Figures 4.12-4.14 show the mesh at slices along constant- y planes; specifically, $y = 0$ inches (the bottom surface of the slipper wedge, or the top of the gap), $y = -0.0625$ inches (or half-way through the gap) and $y = -0.125$ inches (the top surface of the rail or the bottom of the gap); Figures 4.15-4.17 and Figures 4.18-4.20 show the same areas for the adapted meshes. The skewness that resulted from inadequate resolution on the top surface of the rail is seen in Figures 4.12-4.14. The mesh along the bottom surface of the slipper wedge is finer than that on the top surface of the rail and the result is skewed cells in the volume as the mesh generator transitions between the two surfaces.

Figures 4.15-4.20 show that the mesh adaptation may have improved the situation. Due to mesh adaptation, the cells in this region were refined along large pressure gradients and tended to decrease the skewness. The $M_\infty = 3.0$ in air case shows the most adaptation in the region, due to large gradients from the impinging shock wave, while the helium case shows very little adaptation.

Compounding the issue was the lack of adequate resolution in the y -direction, as shown in Figure 4.21. Figures 4.21 and 4.22 show the initial mesh in two planes; the pressure-outflow plane at $x = 23.8$ inches and a slice through the volume at $x = 22.6$ inches. Figures 4.23-4.24 show the final, adapted meshes in the outflow plane. Comparing

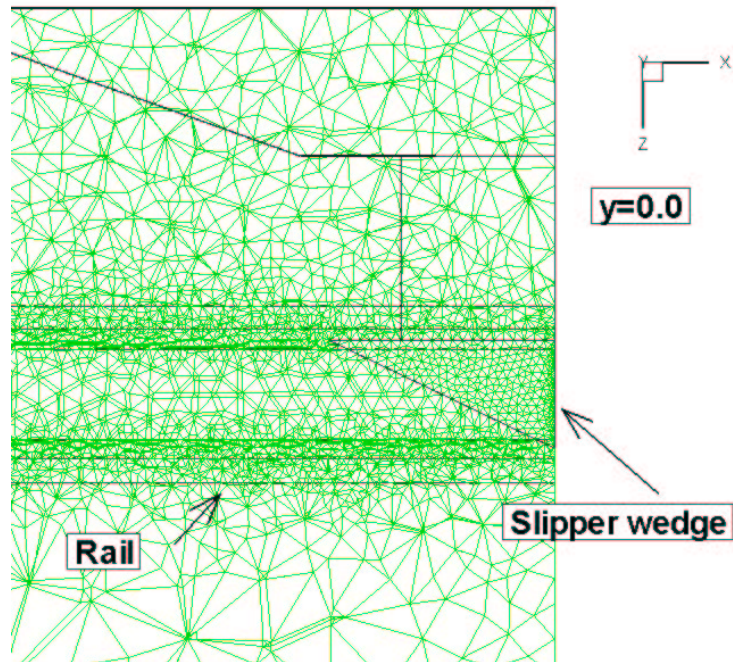


Figure 4.12 Initial Mesh at $y = 0$ Inches (Bottom Surface of Slipper Wedge)

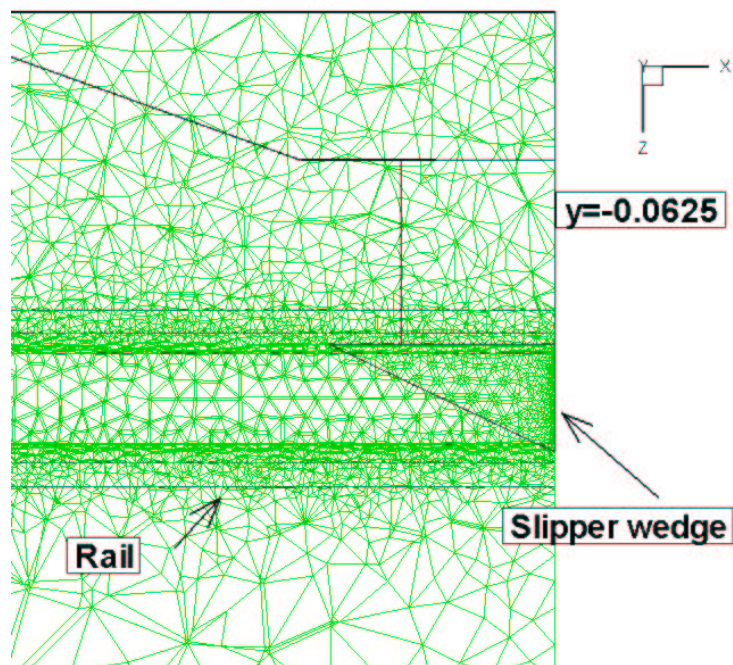


Figure 4.13 Initial Mesh at $y = -0.0625$ Inches (Half-Way Through Gap)

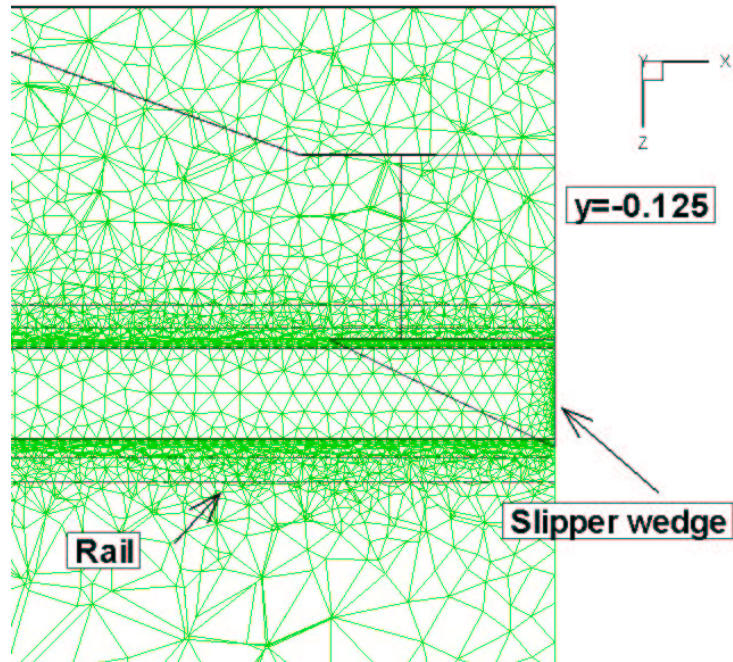


Figure 4.14 Initial Mesh at $y = -0.125$ Inches (Top Surface of Rail)

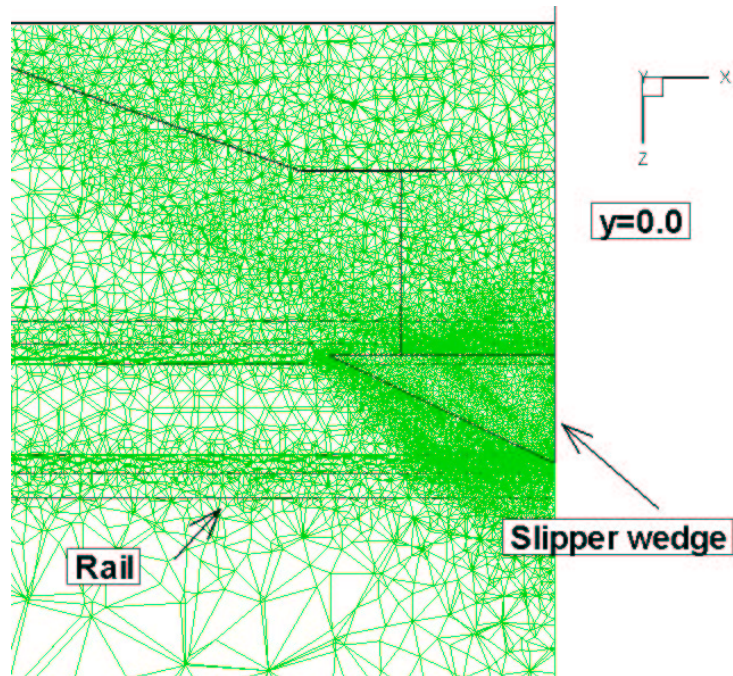


Figure 4.15 Adapted Mesh ($M_\infty = 3.0$ in Air) at $y = 0$ Inches (Bottom Surface of Slipper Wedge)

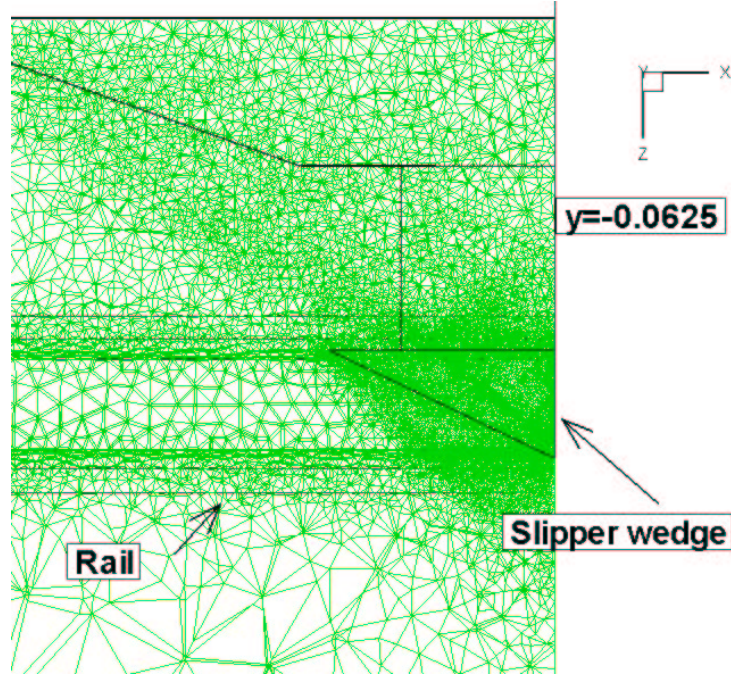


Figure 4.16 Adapted Mesh ($M_{\infty} = 3.0$ in Air) at $y = -0.0625$ Inches (Half-Way Through Gap)

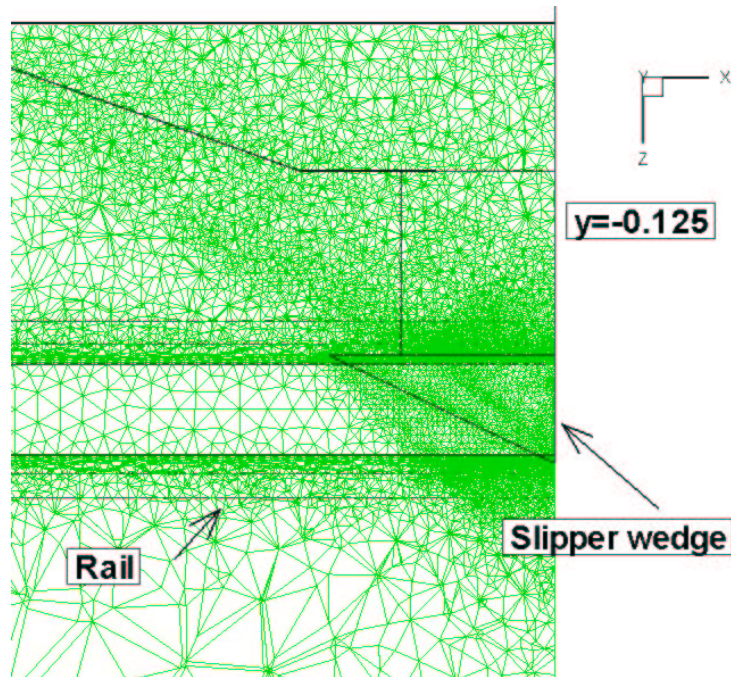


Figure 4.17 Adapted Mesh ($M_{\infty} = 3.0$ in Air) at $y = -0.125$ (Top Surface of Rail)

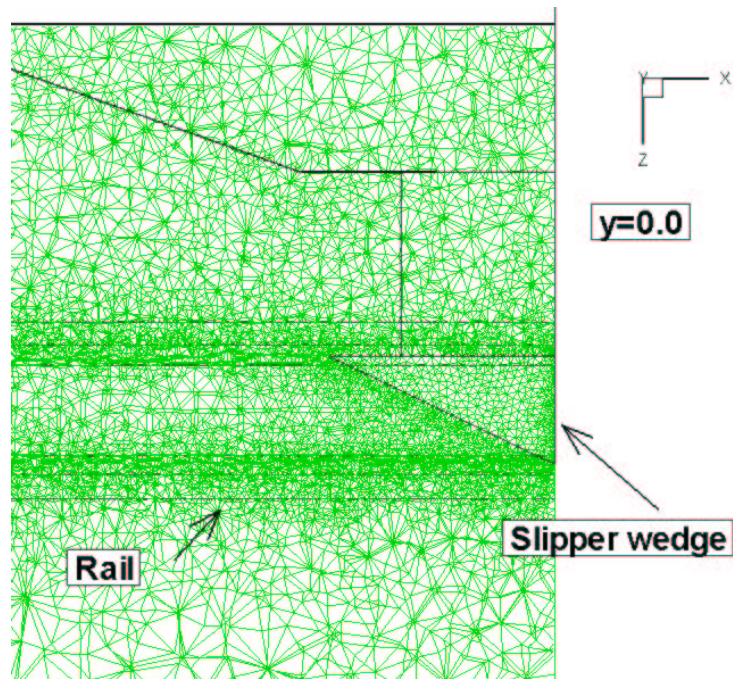


Figure 4.18 Adapted Mesh ($M_{\infty} = 1.02$ in Helium) at $y = 0$ Inches (Bottom Surface of Slipper Wedge)

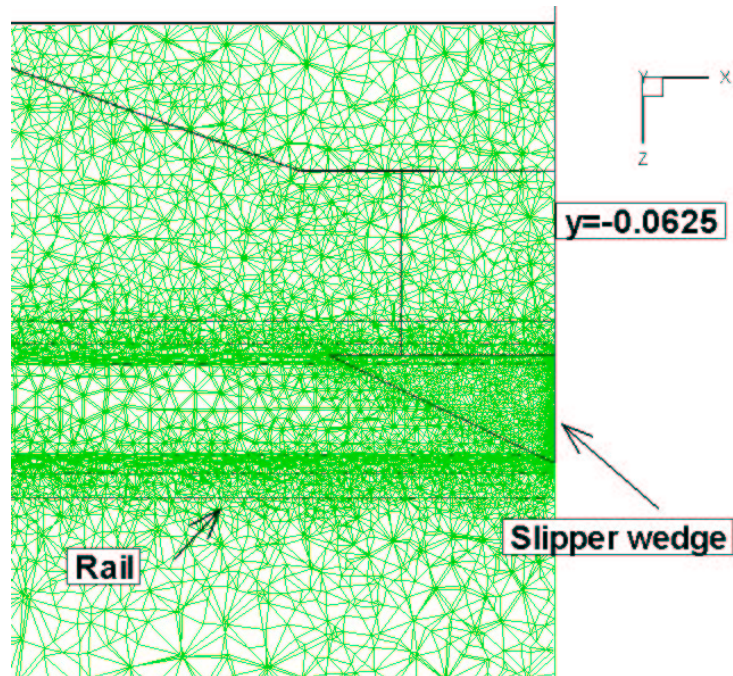


Figure 4.19 Adapted Mesh ($M_{\infty} = 1.02$ in Helium) at $y = -0.0625$ Inches (Half-Way Through Gap)

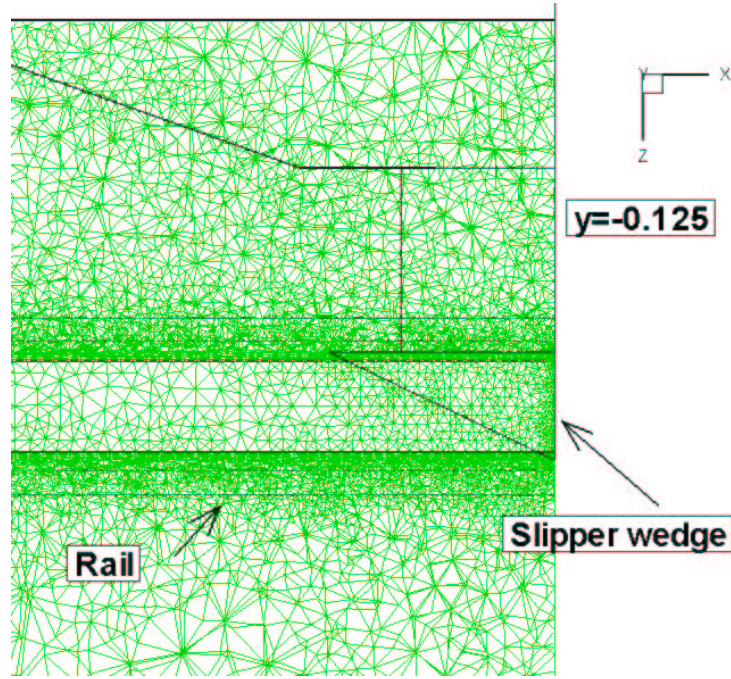


Figure 4.20 Adapted Mesh ($M_{\infty} = 1.02$ in Helium) at $y = -0.125$ Inches (Top Surface of Rail)

the initial mesh to the adapted meshes also shows the same trend mentioned above. Again, the adapted mesh for the air case shows much more cell refinement due to large gradients.

Adding still more problems is the manner in which the rounded portions of the rail were meshed. As mentioned previously, these areas were initially meshed with a structured mesh and converted to an unstructured mesh by diagonalizing each element (to maintain the curvature resolution of the geometry). The net result is also some very skewed cells. Comparing the mesh along constant- x planes shows how the resolution along these domains did not propagate into the volume mesh, as seen in Figures 4.21 and 4.22.

Despite the refinement due to the mesh adaptation, the initial mesh quality may still have adversely affected the stability and accuracy of the solution. Further studies are warranted to investigate this possibility.

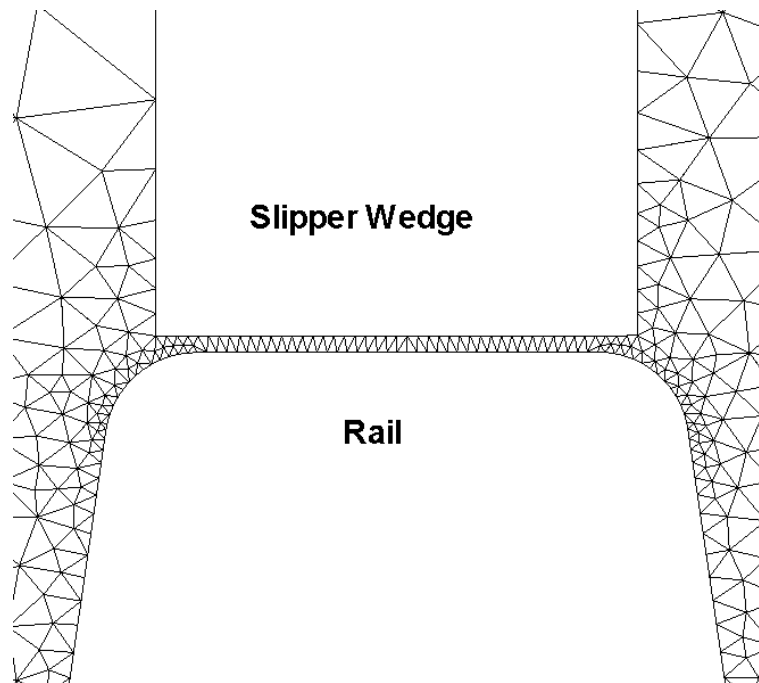


Figure 4.21 Outflow Plane Mesh in Gap Area (Initial Mesh) at $x = 23.8$ Inches

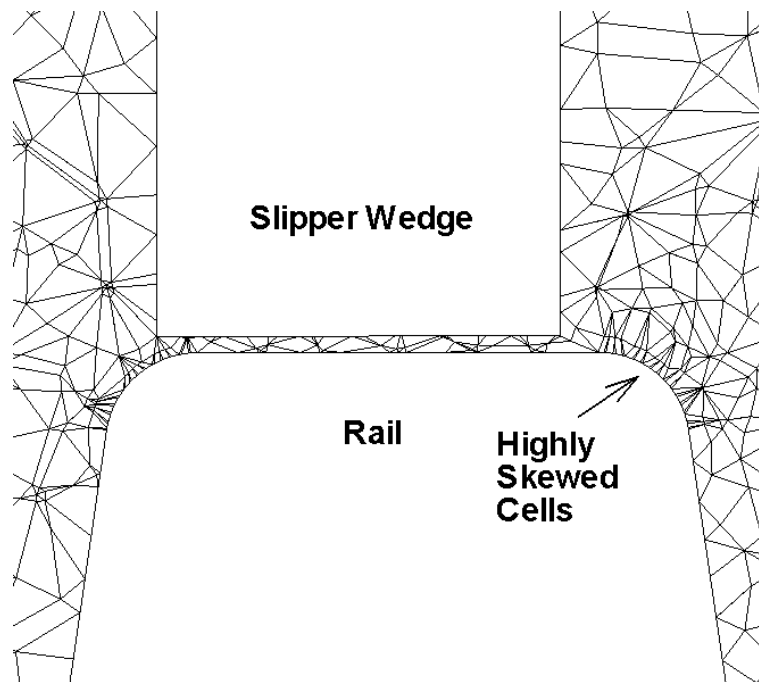


Figure 4.22 Mesh in Plane at $x = 22.6$ Inches

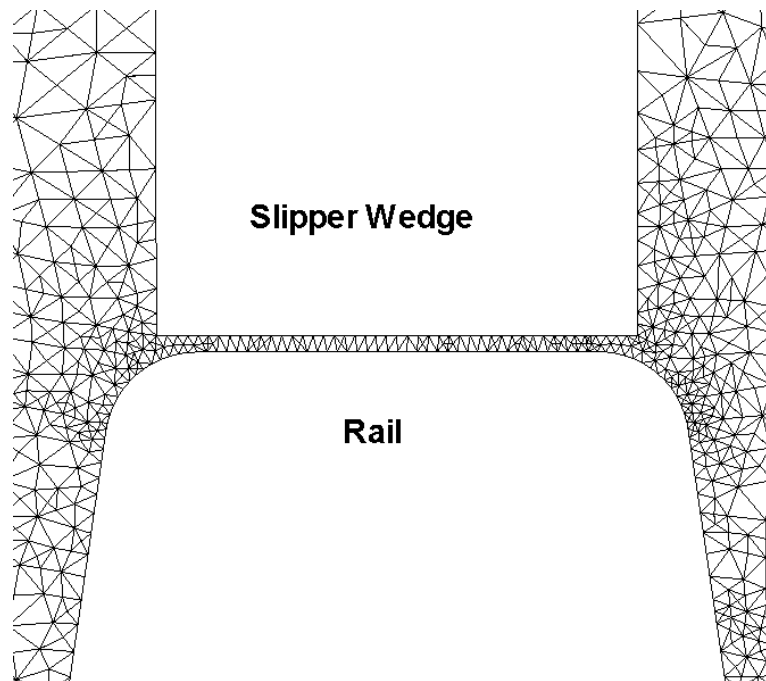


Figure 4.23 Outflow Plane Mesh in Gap Area($M_{\infty} = 3.0$) in Air

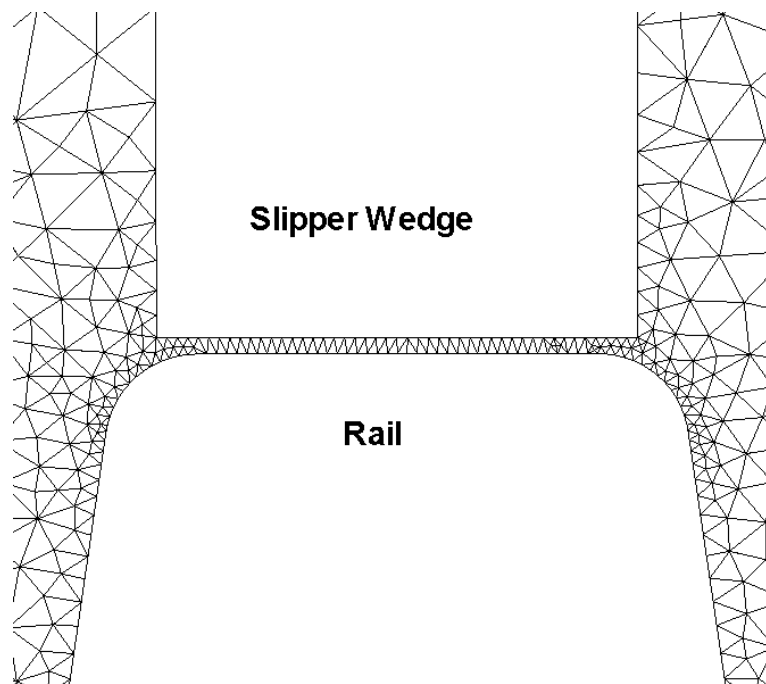


Figure 4.24 Outflow Plane Mesh in Gap Area ($M_{\infty} = 1.02$ in Helium)

Solver Initialization and Flow Solution. The following procedure was used to set up the solution in FLUENT.

Importing the Mesh. Once the mesh was completed in Gridgen (including the definition of the boundary zones), it was exported to a FLUENT Version 5 case file. This case file was read directly into FLUENT. The mesh was checked to ensure that no negative volumes existed, and a smoothing/swapping procedure was performed (as recommended) to ensure maximum mesh quality (4:23.11.3). Since the mesh was generated with units of inches, and FLUENT uses SI units by default, the mesh was scaled, and the units were changed to use English units everywhere (4:4.2-4.3).

Solver Options. The following options were used to set up the initial solution in FLUENT. Under the *define*→*solver* menu, the options for the coupled, explicit, 3D, steady solver with absolute velocity formulation were selected. The viscous model was set to *inviscid* and the energy equation was selected. The material was defined to be an air-helium mixture (to simplify the unsteady modeling of the air-to-helium transition), with species of air and helium only (no chemical reactions were defined). The density was modeled as an ideal gas and the specific heat coefficient was modeled using the mixing law (4:13). Operating pressure was set at zero (all pressures computed are absolute pressures).

The boundary conditions were set as follows. All solid boundaries were modeled as simple walls (slip boundary conditions with the inviscid solver). These included the body, the rail and the ground. The symmetry plane used a simple symmetry boundary condition. The pressure-far-field boundary conditions were set to ambient properties of a standard day of an altitude of 4,093 feet (corresponding to Holloman AFB, New Mexico). These conditions were a pressure of 1,821.39 lb/ft² and a temperature of 504 °R. For a supersonic outflow case, the outlet boundary values are extrapolated from the interior of the domain. However, in case of reverse flow, the pressure-outlet boundary conditions were set to the same values as the pressure-far-field values. The Mach number was set according to the case being run (the initial run used $M_\infty = 2.0$), and the mass fraction was set either to 100% air (as initially run) or 100% helium.

Table 4.1 Mach Numbers and Corresponding Velocities Modeled

M_∞	Velocity(fps)	Environment
2.0	2,200.3	air
3.0	3,300.4	air
1.0215	3,300	helium
2.5	8,075.6	helium
3.096	10,000.8	helium

Flow Field Initialization. Prior to solving the first case, the flow field was initialized to freestream conditions, based on the pressure-far-field boundary (this was $M_\infty = 2.0$ for the first run).

Computation Strategy. The initial flow computed was for $M_\infty = 2.0$ in air. This solution was then used as the initial condition for the $M_\infty = 3.0$ in air case. The helium solutions were initialized for the $M_\infty = 1.02$ case; that solution was used as the initial conditions for the $M_\infty = 2.5$ case, which was then used as the initial condition for the $M_\infty = 3.10$ case. After each solution was iterated for 2,000 iterations (or until converged), the mesh was adapted and the solution computed again. Second-order solutions were computed on the final, adapted first-order mesh.

These values of freestream Mach number were chosen based on the velocities of an actual experimental test run of the hypervelocity sled. The sled initially starts from a resting position and accelerates to about 3,300 fps in air, at which point it transitions to the helium environment. This transition point corresponds to the $M_\infty = 3.0$ and $M_\infty = 1.02$ cases in air and helium, respectively. The sled continues to accelerate in the helium environment to a (desired) top speed of 10,000 fps, which corresponds to the $M_\infty = 3.10$ in helium case. The other values for M_∞ were chosen arbitrarily for ease of the solution. Table 4.1 shows the exact Mach numbers and the corresponding velocities used.

Convergence. As each case was being computed, the residuals were monitored to check for convergence. Residuals are essentially the change in flow field properties from one iteration to the next. Convergence was defined as being the point at which all

residuals were reduced by three orders of magnitude. However, due to some inherent flow instabilities or the low quality of the mesh, only the solution for $M_\infty = 3.0$ in air actually converged according to this definition, and this only with the initial, unadapted mesh.

Another method of determining the convergence of a solution is to monitor an integrated quantity, such as the drag coefficient. This was done for all cases and the solution was judged to be converged when the drag coefficient remained relatively constant over time. To ensure convergence, each of the first-order cases was iterated for 2,000 iterations, and the second-order cases were iterated for 1,000 iterations.

The residual histories for the air-to-helium transition solutions (3,300 fps) are shown in Figures 4.25 and 4.26. The reduction of the residuals by three orders of magnitude is shown in Figure 4.25 (the first 500 iterations) for the $M_\infty = 3.0$ in air case computed with the unadapted mesh as all the residuals fall below the 10^{-3} point. Also note that the spikes in residual values throughout the histories correspond to those points at which the boundary conditions were changed (for example, from $M_\infty = 2.0$ to $M_\infty = 3.0$) or the meshes were adapted and the solutions computed again.

Drag Coefficient. As mentioned previously, the drag coefficient was also monitored. The drag coefficient uses a reference velocity, density and area. The reference velocity was the freestream velocity corresponding to the Mach number, the reference density was the ambient density, and the reference area was the frontal area of the sled body (over which the drag was computed). The values used were

$$A_{ref} = 1.45 \text{ ft}^2 = 208.15 \text{ in}^2$$

$$\rho_{ref} = 0.00936 \text{ lb}_m/\text{ft}^3$$

The drag coefficient histories for the transition cases are shown in Figures 4.27 and 4.28. These plots show that the drag coefficient remains relatively constant with each of the different, adapted meshes used; it can be argued, then, that these solutions can be claimed as being independent of the mesh.

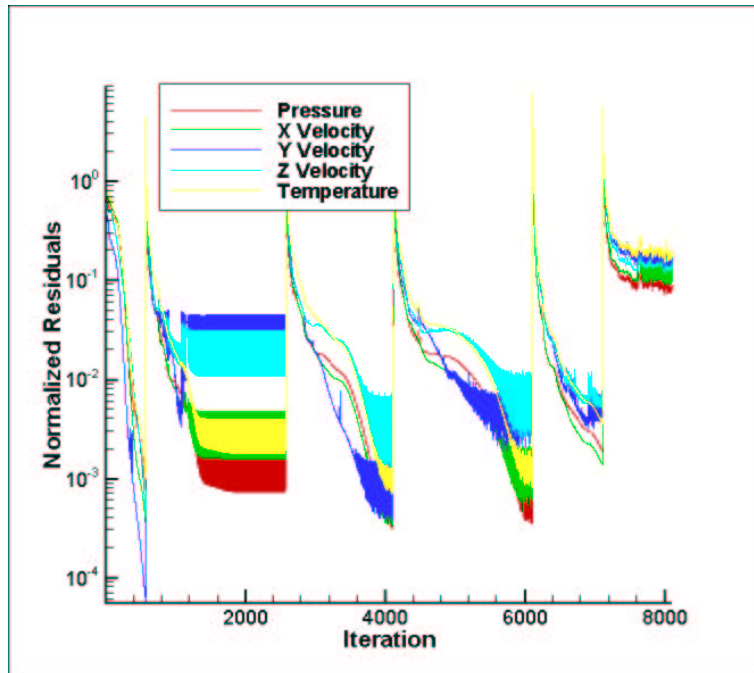


Figure 4.25 Residual History for $M_\infty = 3.0$ in Air

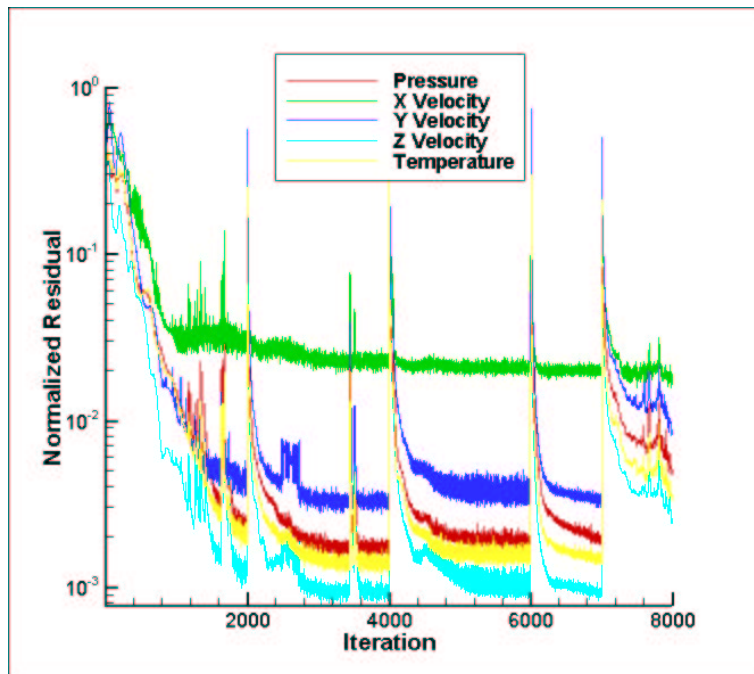


Figure 4.26 Residual History for $M_\infty = 1.02$ in Helium

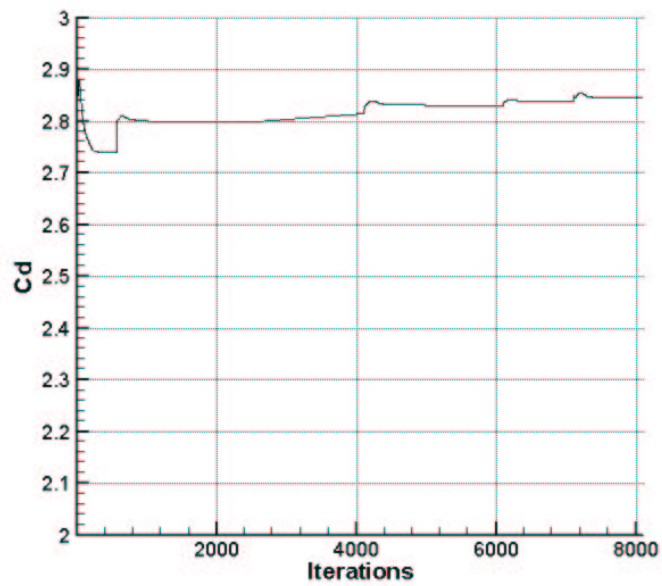


Figure 4.27 Drag Coefficient History for $M_\infty = 3.0$ in Air

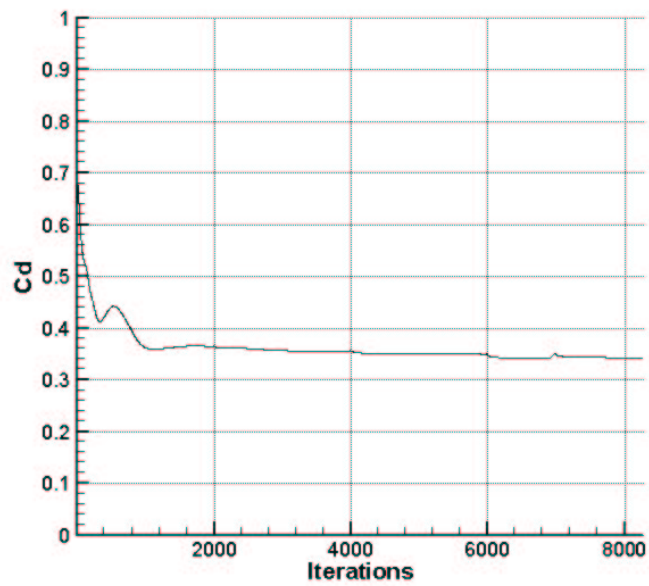


Figure 4.28 Drag Coefficient History for $M_\infty = 1.02$ in Helium

Mesh Adaptation. Once the solution was computed for each case, the meshes were adapted individually to obtain more accurate results. As previously mentioned, since the objective of mesh adaptation is the reduction in solution error, and since most errors are in areas of large gradients, the meshes were adapted based on gradients. For compressible flows, adaptation based on pressure gradients give the best results (4:23.1.2).

Mesh adaptation requires certain guidelines. First, the initial mesh should be fine enough to resolve the geometry. Second, it should be fine enough to resolve important flow features such as shock waves. Third, a “reasonably converged” solution should be obtained prior to the adaptation (4:23.1.2). By using the initial mesh and adapting to the solution after obtaining a fairly-well converged solution, these guidelines were followed.

The mesh adaptation was performed several times. Each time the adaptation parameter was the static pressure gradient. FLUENT adapts the mesh by increasing the number of nodes and re-triangulating the mesh (when using the conformal node method) for each cell with a gradient above a certain threshold value. The user specifies the threshold value. After each adaptation, the mesh was smoothed and cells were swapped to improve the mesh quality (4:23.11).

The threshold value in each case was determined based on memory constraints as well as a desire to reduce the maximum pressure gradient per cell in the solution domain as much as possible. The basic procedure for each case was similar, but the specifics (number of adaptations and threshold used) varied from case to case. Table 4.2 shows the details of the adaptations performed. The adaptation number is simply the number of adaptations performed. The threshold is the pressure gradient threshold (in lb_f/ft^3) used to determine which cells needed to be refined. The maximum gradient is the maximum pressure gradient existing in the solution *prior* to the adaptation. The cell count is the number of tetrahedral cells *after* the adaptation.

In each case, the adaption started with the initial, unadapted mesh of 271,038 cells. Table 4.3 shows the characteristics of the final, adapted mesh. The final meshes contained about 2 million cells; more adaptations were not possible due to computer memory constraints. Also, the maximum pressure gradients in most cases were less than $1,000 lb_f/ft^3$.

Table 4.2 Mesh Adaptations and Threshold Values Used

Case	Adaptation	Threshold	Maximum Gradient ^a	Cell Count ^b
$M_\infty = 2.0$ air	1	10	2060	461,608
	2	1	1298	1,069,455
	3	10	874	1,875,461
	4	100	845	1,959,300
$M_\infty = 3.0$ air	1	10	6649	432,003
	2	1	5948	910,403
	3	10	3226	1,768,803
	4	100	1947	1,921,229
$M_\infty = 1.02$ helium	1	10	310	436,469
	2	1	247	1,377,341
	3	10	166	1,563,328
$M_\infty = 2.5$ helium	1	10	4133	455,314
	2	1	3413	1,022,144
	3	10	1889	1,177,631
	4	50	1281	1,668,122
$M_\infty = 3.10$ helium	1	10	5725	441,439
	2	1	4030	950,619
	3	100	2915	1,152,504
	4	50	1846	1,772,524
	5	100	1888	2,153,145

^aGradients in lb_f/ft^3 ; maximum gradient *before* adaptation.

^bCell count *after* adaptation.

This seems to be the best that can be obtained with current memory restrictions, although the ideal case would reduce the gradients to $O(1)$. The exceptions to these two statements are, of course, the $M_\infty = 3.0$ case in air, which has higher maximum gradients; and the $M_\infty = 1.02$ in helium case, which has a lower number of cells. In each case this is due to the characteristics of the flow and the magnitude of the pressure gradients (less severe gradients means less cells required; more severe gradients require more cells).

It should be noted that the adaptations were performed on first-order solutions only. Following the final adaptations based on the first-order solutions, a second-order solution was attempted. Stable second-order solutions were obtained only for the $M_\infty = 3.0$ in air and $M_\infty = 1.02$ in helium cases.

Table 4.3 Final Properties of Adapted Meshes

Case	Cell Count	Maximum Gradient (lb_f/ft^3)
$M_\infty = 2.0$ (air)	1,959,300	686
$M_\infty = 3.0$ (air)	1,921,229	1456
$M_\infty = 1.02$ (helium)	1,563,328	117
$M_\infty = 2.5$ (helium)	1,668,122	769
$M_\infty = 3.1$ (helium)	2,153,145	972

Inviscid, Unsteady

All solutions mentioned thus far have been steady computations. These assume that the properties of the flow are unchanging through time. For the most part, these solutions should model the actual flow fairly well (assuming a snapshot in time). Additionally, the changes in flow properties are relatively gradual as the sled accelerates to mission speeds.

However, the transition from the air environment to the helium environment as the sled enters the helium tent is rather abrupt, and causes some very time-dependent flow features. Therefore, an unsteady computation was performed to capture the dynamics of the flow during this transition.

Solver Initialization and Flow Solution. The simplest method to model the air-to-helium transition is to simply change the boundary conditions on the pressure-far-field boundary. For this reason the material in the computations was modeled as an air-helium mixture; it was a simple matter to change the composition of the fluid at the boundary from 100% air to 100% helium. Additionally, the incoming Mach number was changed from $M_\infty = 3.0$ (in air) to $M_\infty = 1.0215$ (in helium). In this way, the actual ground speed remained 3,300 fps.

The mesh used in the unsteady solutions was the initial, unadapted mesh. Adapted meshes weren't used for two main reasons. First, the adaptation is solution-specific; the adaptation used for the $M_\infty = 3$ solution wouldn't be optimal for a $M_\infty = 1.02$ flow. Second, since the adaptations are solution specific, the adaptations would have to be performed at each individual time step. This method was judged to be too prohibitive in terms of computation time. Therefore, the unsteady computation was initialized using the $M_\infty = 3.0$ first-order solution on the unadapted mesh.

FLUENT provides two different ways to perform unsteady computations. One uses an explicit time integration scheme. With this scheme, the solution after each time-step is solved in one iteration. The time-step is selected by the solver based on the flow properties. The user determines how many iterations (thus, how long in time) over which to compute the solution.

The second method is an implicit method. Here, the user chooses the time-step and the solution at each time is iterated to convergence. The user also specifies the maximum number of iterations to perform at each time-step. This is necessary for flows (like the situation studied here) that may not necessarily meet the convergence criteria (namely, the reduction in residuals by a specified amount). The user can choose between a first-order or a second-order implicit time-integration method (4:22.15.1). Since the second-order solutions showed stability problems, and since the initial data was first-order accurate, the unsteady computations used the first-order implicit method.

The time-step used was chosen based on the FLUENT recommendation that it be small enough to allow the solution to converge within about 20 iterations per time-step (4:22.15.1). The unsteady solution was computed using a time-step of 5×10^{-6} seconds for 1,500 steps (modeling a total of 0.0075 seconds). Previous solutions computed showed that the unsteadiness in the transition settled out after about 0.0075 seconds. The maximum number of iterations per time-step was set at 40 in case the solution didn't converge within the 20 iterations as expected. The convergence criteria remained a reduction of the residuals by three orders of magnitude.

FLUENT allows the user to animate the flow solution during an unsteady solution. This is done by taking snapshots of flow property contours or other plots of certain variables. Animations of pressure contours, species mass fraction, temperature contours, etc. were thus obtained by taking snapshots every four time-steps (or every 2×10^{-5} seconds). The data file was also automatically saved every 20 time-steps (to be visualized in Tecplot).

V. Results and Discussion

As mentioned previously, second-order solutions were obtained only for the $V_\infty = 3,300$ fps cases (the air-to-helium transition regime); oscillations of flow properties, possibly attributed to the implicit use of limiters for numerical stability and robustness, restricted solutions for the other cases to first-order accuracy. The results presented here will focus on the second-order cases, although they will be compared to the first-order results to illustrate the effect of Mach number. The first-order, unsteady results will also be presented briefly. All results given are for static quantities (temperature and pressure) versus stagnation or total quantities.

Computational Time

In each case for which solutions were computed, the final meshes were close to 2 million cells, as were shown in Table 4.3. This required a significant amount of computational resources, both in CPU time and memory required. Table 5.1 gives a summary of the computational time required to run 1,000 iterations in each case. These computations were performed on the Beowulf class cluster. The wall clock times are not exact; all solutions given here were run in batch mode so the exact time is unknown. FLUENT gives an estimate of the time remaining for the number of iterations requested throughout the computation. If the solutions converges prior to completing the requested number of iterations, the time shown is more than the actual time. This is the case in the two situations where the solution did converge (according to the reduction of residuals by three orders of magnitude criteria).

The advantage of using parallel processing is illustrated in Table 5.2. The time required to compute 1000 iterations for the $M_\infty = 3.0$ in air case with the unadapted, 271,038 cell mesh on two different platforms is shown. There is a large difference in the time taken when using only one processor on each machine, but there is very little difference when using two processors (two networked workstations were used for the two-processor Compaq Alpha case, while one dual-processor node was used for the two-processor Linux cluster case). This is most likely due to the smaller amount of memory on the Compaq

Table 5.1 Computation Time

Case	Adaptation	Cell Count	# CPUs	Wall Clock Time (hours:minutes)
$M_\infty = 2.0$ air	none	271,038	2	1:30
	1	461,608	2	2:15
	2	1,069,455	2	5:45
	3	1,875,461	4	5:20
	4	1,959,300	4	4:30
$M_\infty = 3.0$ air	none	271,038	2	1:30*
	1	432,003	2	2:00
	2	910,403	2	4:10*
	3	1,768,803	2	8:30
	4	1,921,229	4	4:30
	<i>2nd order</i>	1,921,229	4	8:15
$M_\infty = 1.02$ helium	none	271,038	2	1:30
	1	436,469	2	2:05
	2	1,377,341	2	6:45
	3	1,563,328	2	8:00
	<i>2nd order</i>	1,563,328	4	7:30
$M_\infty = 2.5$ helium	none	271,038	2	1:40
	1	455,314	2	3:00
	2	1,022,144	2	5:25
	3	1,177,631	2	5:40
	4	1,668,122	2	8:00
$M_\infty = 3.10$ helium	none	271,038	2	1:25
	1	441,439	2	2:10
	2	950,619	2	5:05
	3	1,152,504	2	5:30
	4	1,772,524	2	20:00
	5	2,153,145	4	5:30
unsteady	none	271,038	8	24:00

*Met convergence criteria of a residual reduction by three orders of magnitude.

Table 5.2 Parallel Computation Times

# CPU	Machine	Time (h:m:s)	Network Protocol	FLUENT Version
1	Compaq Alpha Workstation	4:14:17	N/A	5.5.14
2		1:13:05	Ethernet (sockets)	
1	Linux Cluster	3:11:46	N/A	6.0.12
2		1:03:36	SMP	
4		0:41:27	Ethernet (sockets)	
8		0:27:43	Ethernet (sockets)	
2		1:03:48	Myrinet (sockets)	
4		0:41:13	Myrinet (sockets)	
8		0:27:56	Myrinet (sockets)	

Alpha workstations; if the entire computational problem doesn't fit in physical memory, more time is required due to memory swap operations. There is practically no difference in the compute times when comparing the use of the Ethernet and Myrinet networks. This can be explained in two ways; either there is very little communication occurring during the computations, or the socket interface used in both cases gives similar communication results. Also note that two different versions of FLUENT were used on the different architectures, and the computation times may have been influenced by improvements made in the new version. However, the full benefits of the higher-speed Myrinet network were not utilized; message passing libraries using the lightweight GM network protocol would take advantage of its capabilities. In general, though, FLUENT shows excellent parallel performance.

Post-Processing Issues

One significant drawback in using different commercial software packages for the different steps in a CFD analysis (i.e., mesh generation, computation, visualization) is the portability and compatibility of data file formats between the different software packages. Porting the mesh between Gridgen and FLUENT was not a problem because Gridgen supports FLUENT Version 5 file formats. However, porting data between FLUENT and Tecplot became an issue.

FLUENT supports exporting data files to a Tecplot format. However, FLUENT writes the Tecplot data using a triangular (area) format, rather than a tetrahedral (vol-

ume) format, even for the volume interior. Some of Tecplot's 3D features (iso-surface visualization and 3D slices) require the data to be in a volume format.

Tecplot, on the other hand, also supports importing FLUENT case and data files. The problem here is that FLUENT stores the data at the cell centers, while Tecplot requires the data to be at the node points. The FLUENT importer add-on for Tecplot works around this by interpolating the data at the cell centers to find the values at the node points. Unfortunately, the data at the boundary zones gets lost in this conversion and therefore, the data sets imported in this way does not contain data (pressure, temperature, velocity, etc) on the boundary zones, and no surface contour plots can be generated.

These issues were resolved by using portions of both data sets for different zones. The data exported by FLUENT into Tecplot format was used for the surface (boundary) zones, and the data imported by Tecplot from FLUENT was used for the interior volume data. In this way, all the features of Tecplot were available. Future work using FLUENT as the flow solver should be done using a scientific visualization software package that directly supports FLUENT data formats without the loss of surface data.

Definitions

The basic variables that were initially used in the data files were mesh coordinates (x, y, z) , velocities (u, v, w) , static temperature (T) , static pressure (p) and density (ρ) . Other variables were computed from these using the CFD Analyzer Tecplot add-on (for Mach number and pressure coefficient) and directly specifying the equations in Tecplot (x-, y- and z- momentum and velocity magnitude). The definitions of these variables used in the computations are (1:63-68)

$$\|U\| = \sqrt{(u^2 + v^2 + w^2)} \quad \text{velocity magnitude} \quad (5.1)$$

$$M = \frac{\|U\|}{\sqrt{\gamma RT}} \quad \text{Mach number} \quad (5.2)$$

$$x - \text{momentum} = \rho u \quad (5.3)$$

$$y - \text{momentum} = \rho v \quad (5.4)$$

$$z - momentum = \rho w \quad (5.5)$$

$$C_p = \frac{p - p_\infty}{\rho_\infty U_\infty^2 / 2} \quad (5.6)$$

where the reference quantities were specified according to a standard day at an altitude of 4,093 feet (or 1,247.5 meters) for Holloman AFB, NM (21).

$$p_\infty = 87210.4 \text{ Pa} = 1821.39 \text{ lb}_f/\text{ft}^2 = 12.65 \text{ psi}$$

$$T_\infty = 280 \text{ K} = 504 \text{ R}$$

$$\rho_\infty = 1.08486 \text{ kg/m}^3$$

$$R_{air} = 287 \text{ J/(kg K)}$$

$$\gamma_{air} = 7/5$$

$$R_{helium} = 2078 \text{ J/(kg K)}$$

$$\gamma_{helium} = 5/3$$

Analytical Solutions

Analytic solutions for several regions of the flow surrounding the sled were computed using simple oblique shock relations for 2D wedges and axisymmetric cones. Figures 5.1 and 5.2 show the regions that were used. The freestream conditions used matched the conditions for the $M_\infty = 3.0$ in air case (with $p_\infty = 12.65$ psi). The analytic solutions are summarized in Table 5.3. Figures 5.3-5.7 compare these analytic results to the computed results. The data for the computed results were obtained by extracting data along polylines in Tecplot.

Region 1 contains the flow after the shock generated from the payload cone. The flow was modeled as a simple, supersonic cone. The freestream conditions were used as the input conditions, and the pressure after the shock (along the surface of the cone) was obtained using NACA Report 1135 (16). Computational data was taken along the upper surface of the cone at the symmetry plane. Figure 5.3 shows that the computational results agree fairly well with the theoretical with the exception of the large oscillations near the

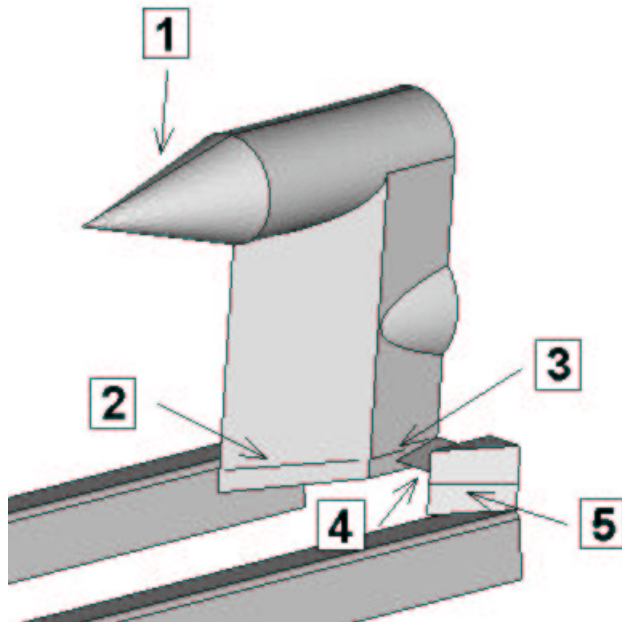


Figure 5.1 Regions of Flow Defined for Analytic Solution

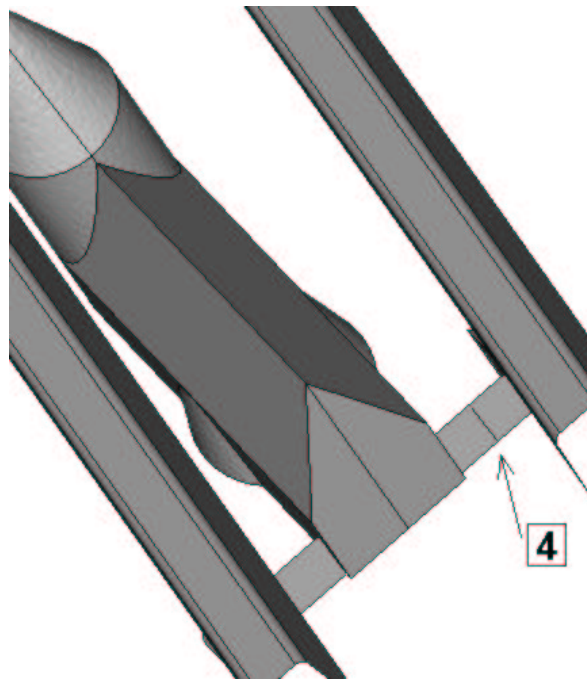


Figure 5.2 Regions of Flow Defined for Analytic Solution

Table 5.3 Summary of Analytic Results for $M_\infty = 3.0$ in Air

Region	Geometry	Input Conditions	Pressure (<i>psi</i>)
1	15° Cone	Freestream	26.55
2	19.65° Wedge	Freestream	47.01
3	19.65° Expansion	Region 2	13.15
4	5.25° Wedge	Freestream	18.66
5	25.6° Wedge	Freestream	64.53

upstream point. This is most likely due to the faceted nature of the mesh, as shown in Figure 5.4. Even though the data was extracted along the symmetry plane, where the mesh is smooth, the data still retain some of the effects of the uneven mesh, most likely due to interpolations from cell-centered data to node-centered data.

Region 2 is the flow along the lower portion of the large, vertical wedge. Simple oblique shock relations were used to calculate the pressures downstream of the attached shock. Freestream conditions were used as input conditions. Computational data was taken along a line from the vertical wedge leading edge to the shoulder, at $y = 4$ inches. The Region 2 data also compare well with the analytical results, as shown in Figure 5.5. After the initial compression through the shock, the pressure remains fairly constant as predicted, but then drops off. This is due to three-dimensional effects. While the analytical results are only valid for a strictly two-dimensional wedge, the actual modeled wedge is three-dimensional. As the flow expands around the bottom of the wedge, the pressure decreases.

Region 3 uses Region 2 values as the input values. The flow here expands around the shoulder of the vertical wedge. Prandtl-Meyer relations were used to compute the flow properties. Region 3 computational data continued from the Region 2 data back to about $x = 20$ inches (just above the strut wedge), at $y = 4$ inches. The data follows the constant trend predicted, but the magnitude is lower, as seen in Figure 5.6. The analytical results used the higher pressures predicted for Region 2 as the input values, but the actual values were lower due to the expansion around the bottom surface. This caused the pressure magnitude in Region 3 to be lower than expected.

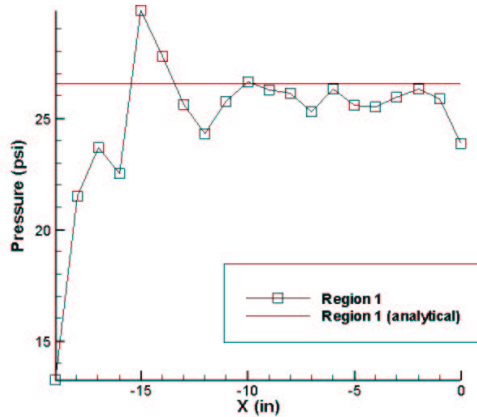


Figure 5.3 Region 1 Pressure

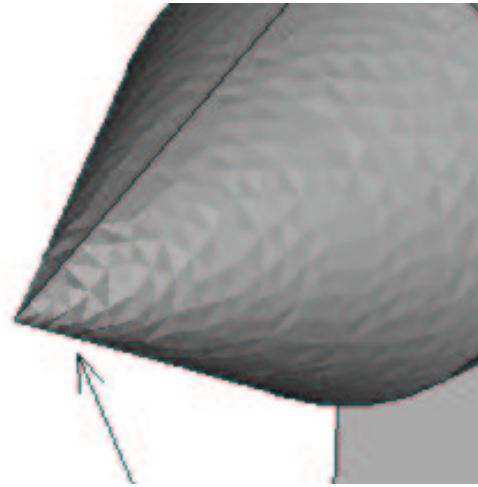


Figure 5.4 Detail of Mesh on Payload Cone

Region 4 is the underside of the strut wedge; freestream conditions were used as inputs. Computational data was taken along the lower strut wedge, midway between the sled body and the slipper wedge. Here, the computed results do not match the analytical results. This is certainly due to the many interactions present in that area, as seen by the pressure contours in Figure 5.8. The shock generated at the leading edge of the vertical wedge impinges on the slipper wedge and is reflected back along the strut wedge. This reflected, as well as causes the pressure gradients computed that would not be predicted when using simple, 2D oblique shock theory.

Region 5 is the outboard side of the slipper wedge. Again, freestream values were used as inputs to the oblique shock relations. Computational data was taken from the leading edge of the slipper wedge to the outflow plane, midway (vertically) between the bottom and top surfaces. The computational results again show good agreement with the analytical results, as seen in Figure 5.9. The drop in pressure is also due to the three-dimensional effects as the flow expands around the upper surface of the wedge, and around the rail below the lower surface.

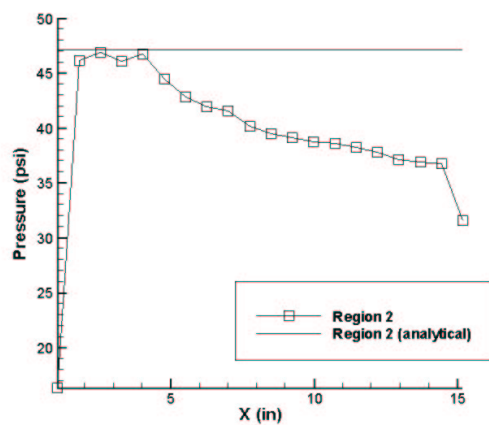


Figure 5.5 Region 2 Pressure

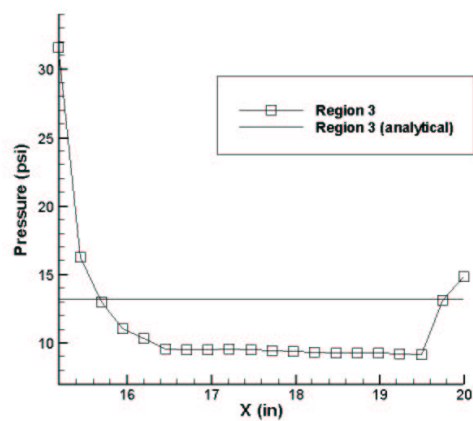


Figure 5.6 Region 3 Pressure

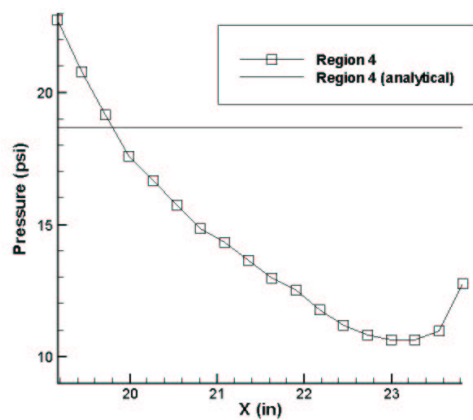


Figure 5.7 Region 4 Pressure

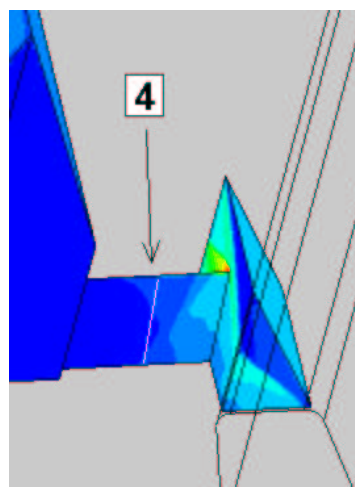


Figure 5.8 Region 4 Pressure Contours

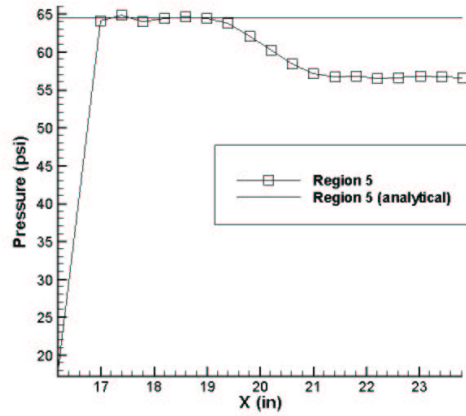


Figure 5.9 Region 5 Pressure

Steady, Inviscid Flow

Given that the present results do not include any viscous effects, the temperature distributions presented will not agree with experimental results in magnitude, but the general trends should be similar. On the other hand, since boundary-layer analysis shows that the pressure gradient normal to the surface through an attached boundary-layer is negligible, the pressure distributions presented should be fairly close to those experienced by the actual sled under the same conditions.

Overview of Results. The computational results for all computed cases (including the first-order solutions) are presented here. A more detailed analysis of the two second-order solutions will follow.

High-speed, inviscid flow properties are affected by discontinuities in the flow field, such as shock waves and expansion waves. The location of these features depends on the freestream Mach number and the body geometry. Figures 5.10-5.14 show the general shape of the shock waves generated by the sled at different Mach numbers and in different environments. The shocks are visualized in each case by an iso-surface for a Mach number just below the freestream Mach number.

These figures show that the bow shock impinges on the sled structure at different points for the different freestream Mach numbers. The location of the shock impingement

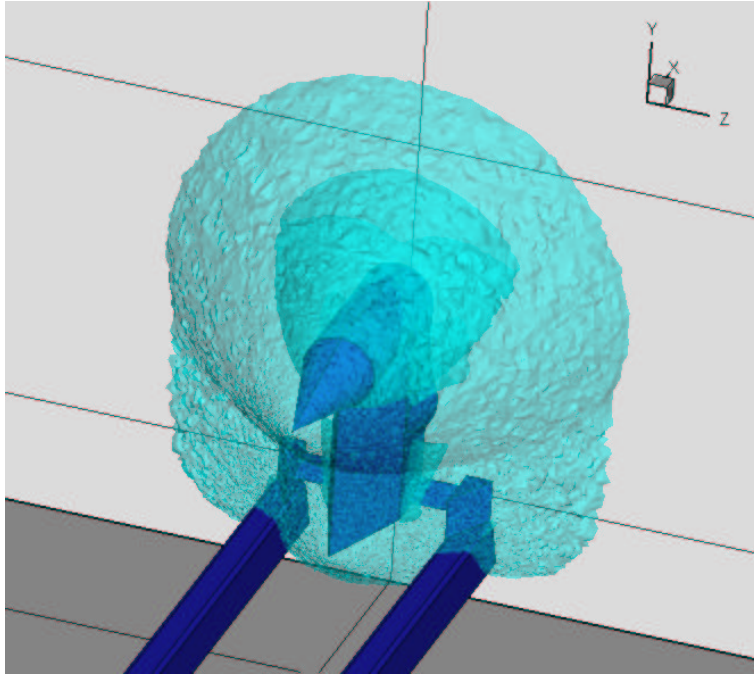


Figure 5.10 Mach Iso-Surface for $M_\infty = 2.0$ in Air (2,200 fps)

on the slipper wedge structure is shown in the $M_\infty = 3.0$ in air case with a red arrow (Figure 5.11). The Mach iso-surface also shows an expansion around the bottom of the vertical wedge, shown by the second red arrow in Figure 5.11. The $M_\infty = 1.02$ in helium case does not demonstrate a strong shock because it is in the transonic regime. The effects of the mesh are evident when looking at the texture of the iso-surfaces.

Figures 5.15-5.24 show the surface pressure and temperature contours for each of the cases. In the case of $M_\infty = 3.0$ in air, pressure gradients due to the cone shock's impinging on the vertical wedge are evident. However, the largest pressures and temperatures (and the largest gradients) are at the location where the shock from the vertical wedge impinges on the slipper wedge structure. In the case of $M_\infty = 1.02$ in helium, there is no shock impinging on the structure; therefore, the maximum temperature and pressure values are in the stagnation regions on the leading edges of the wedges. As the sled moves from the air environment to the helium environment, the magnitude of the pressures is reduced by approximately one order of magnitude, demonstrating the benefits of using the helium environment.

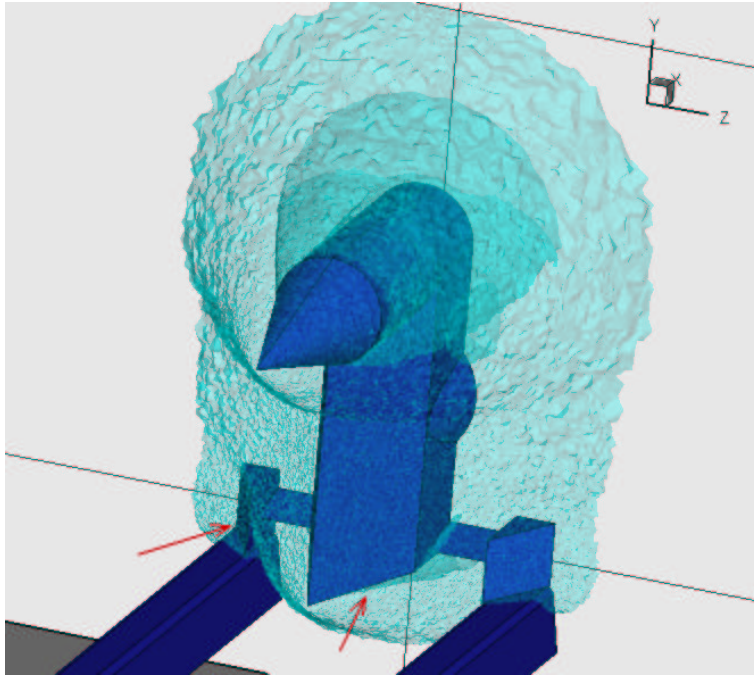


Figure 5.11 Mach Iso-Surface for $M_{\infty} = 3.0$ in Air (3,300 fps)

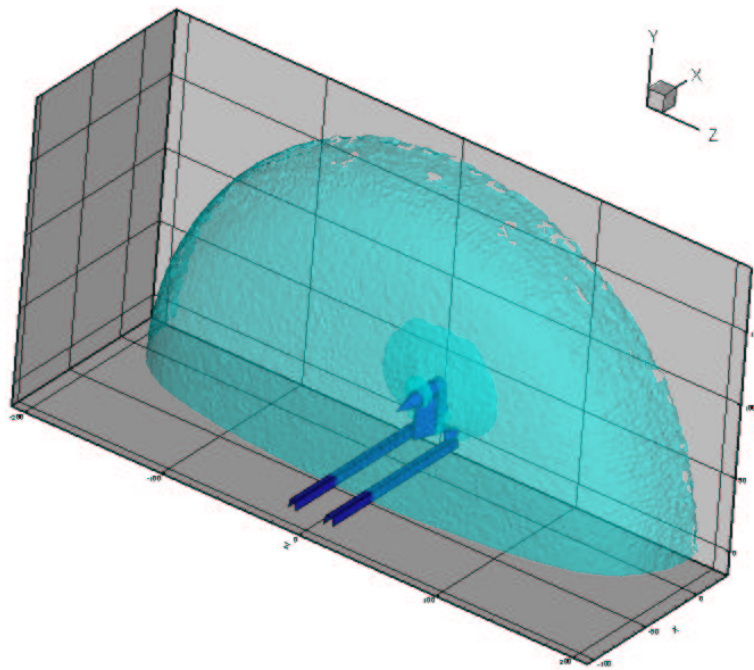


Figure 5.12 Mach Iso-Surface for $M_{\infty} = 1.02$ in Helium (3,300 fps)

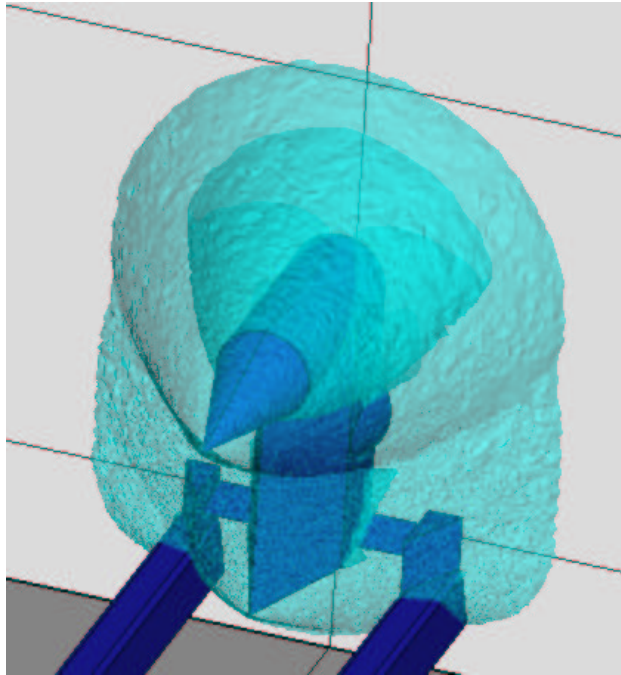


Figure 5.13 Mach Iso-Surface for $M_\infty = 2.5$ in Helium (8,076 fps)

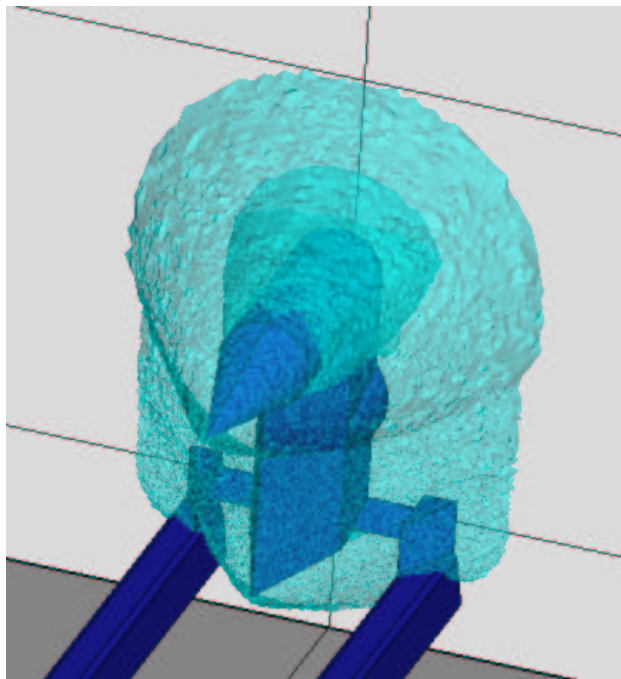


Figure 5.14 Mach Iso-Surface for $M_\infty = 3.10$ in Helium (10,000 fps)

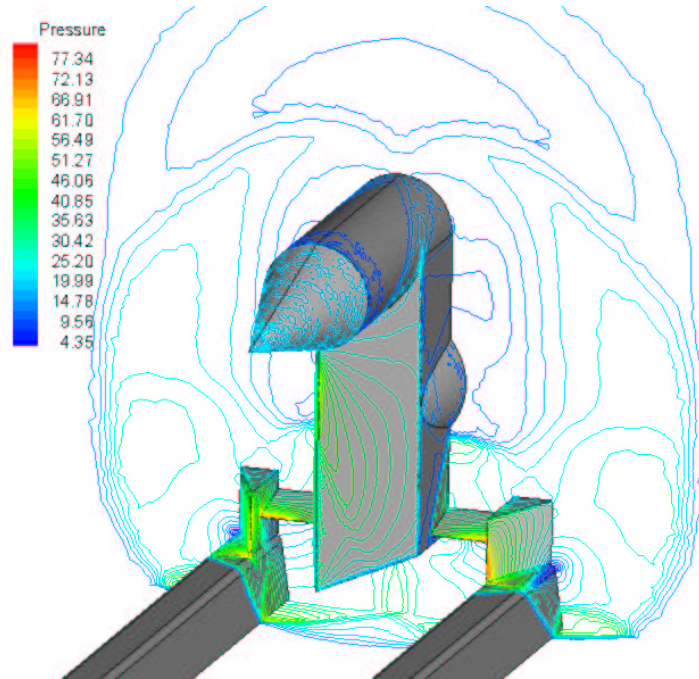


Figure 5.15 Surface Pressure Contours (psi) for $M_\infty = 2.0$ in Air

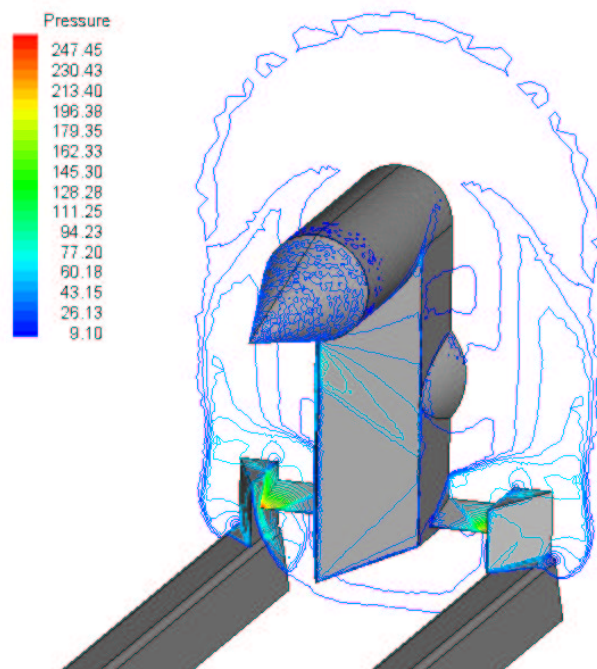


Figure 5.16 Surface Pressure Contours (psi) for $M_\infty = 3.0$ in Air

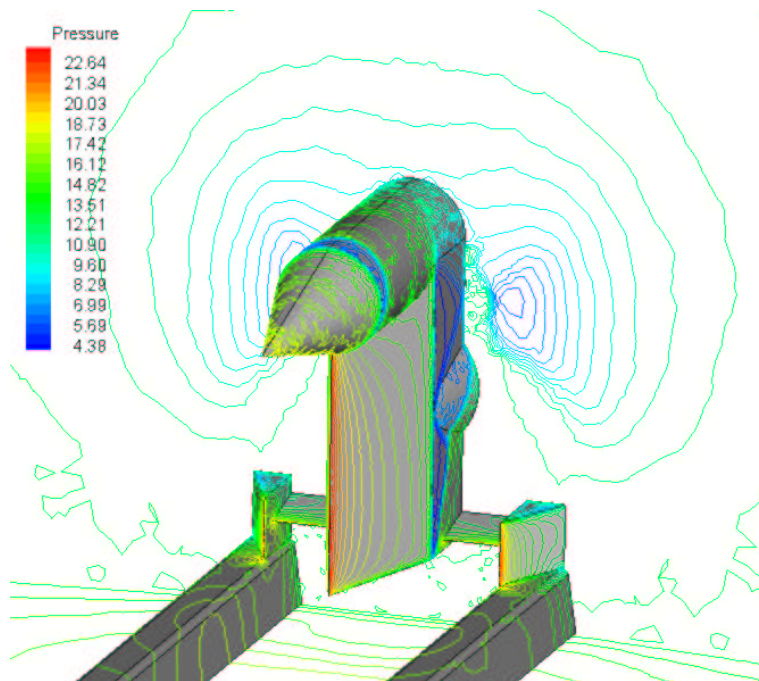


Figure 5.17 Surface Pressure Contours (psi) for $M_\infty = 1.02$ in Helium

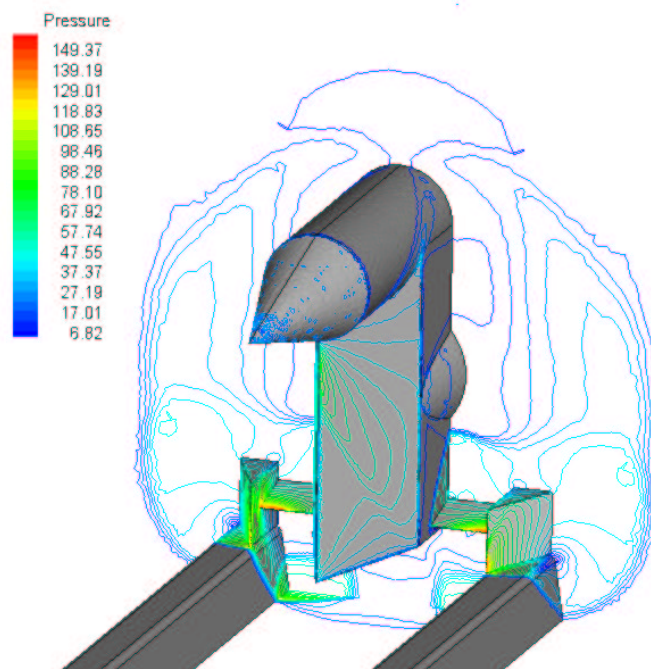


Figure 5.18 Surface Pressure Contours (psi) for $M_\infty = 2.5$ in Helium

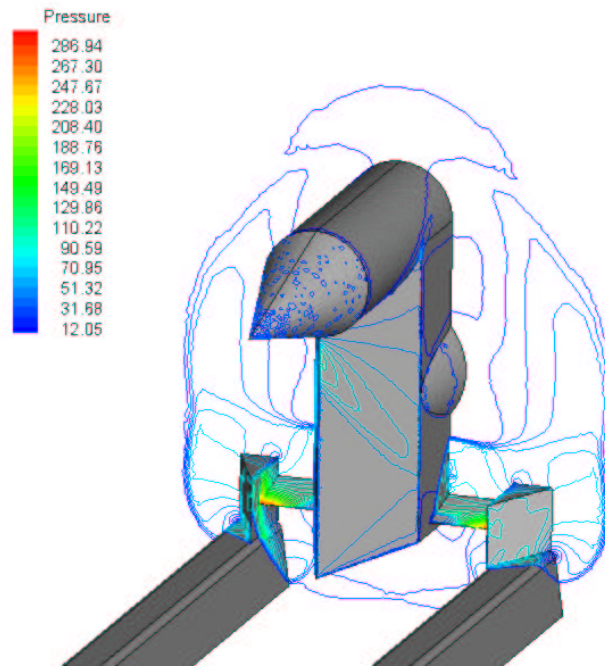


Figure 5.19 Surface Pressure Contours (psi) for $M_\infty = 3.10$ in Helium

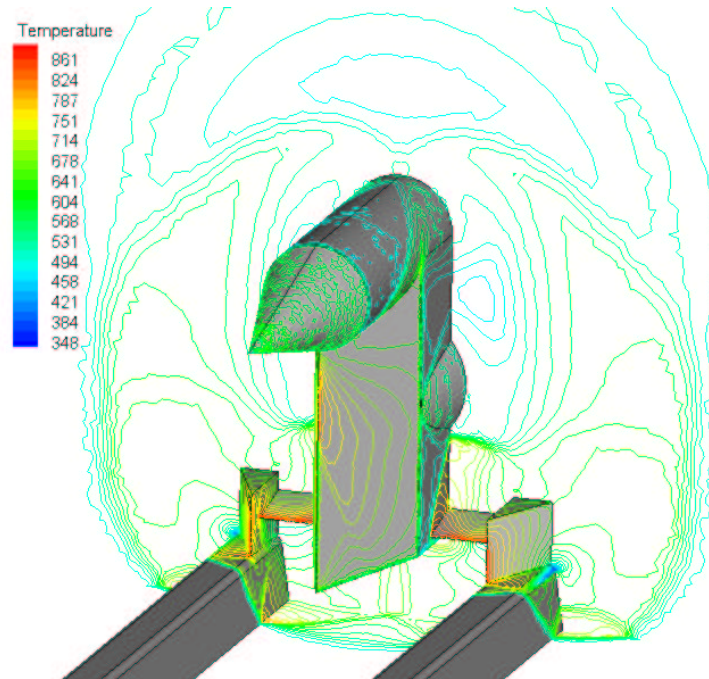


Figure 5.20 Surface Temperature Contours ($^{\circ}\text{R}$) for $M_\infty = 2.0$ in Air

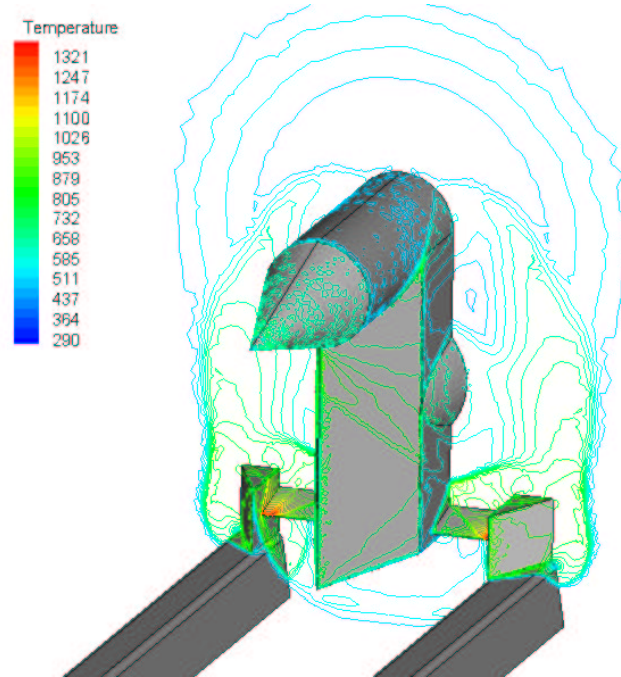


Figure 5.21 Surface Temperature Contours ($^{\circ}\text{R}$) for $M_{\infty} = 3.0$ in Air

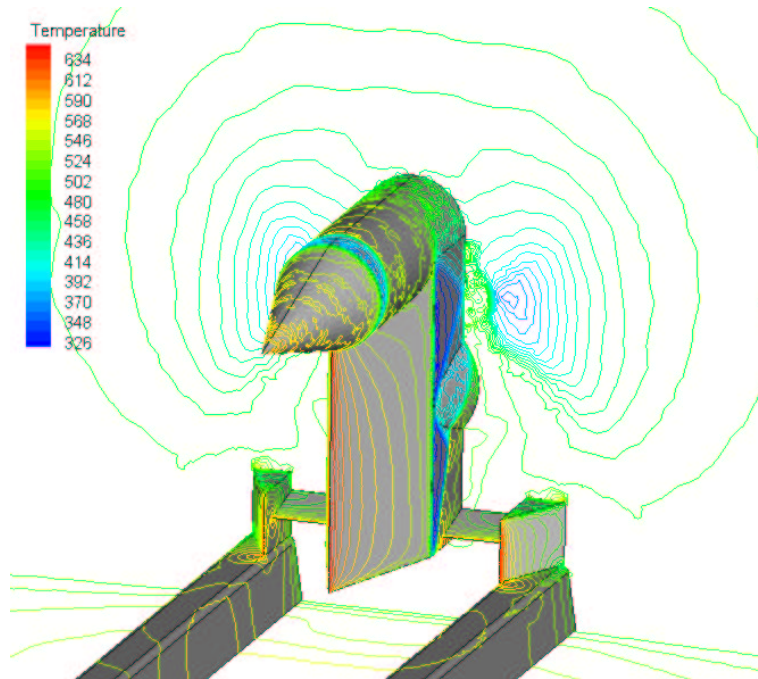


Figure 5.22 Surface Temperature Contours ($^{\circ}\text{R}$) for $M_{\infty} = 1.02$ in Helium

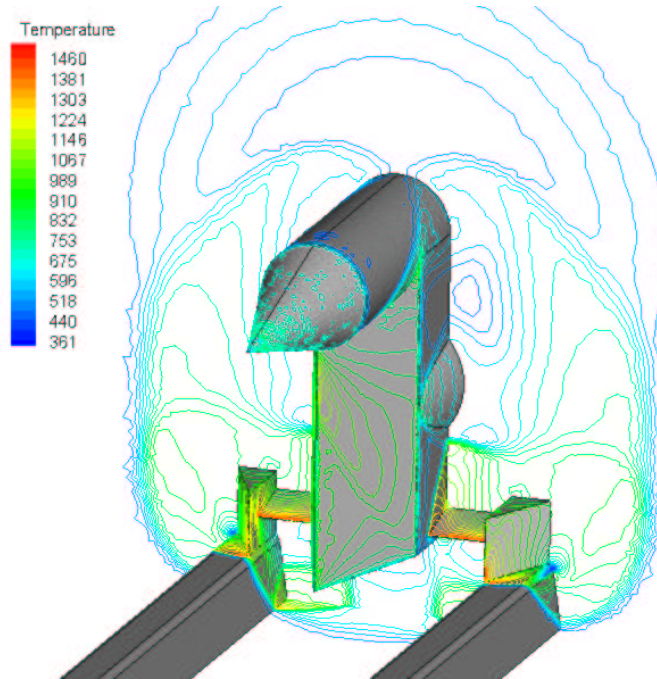


Figure 5.23 Surface Temperature Contours ($^{\circ}\text{R}$) for $M_{\infty} = 2.5$ in Helium

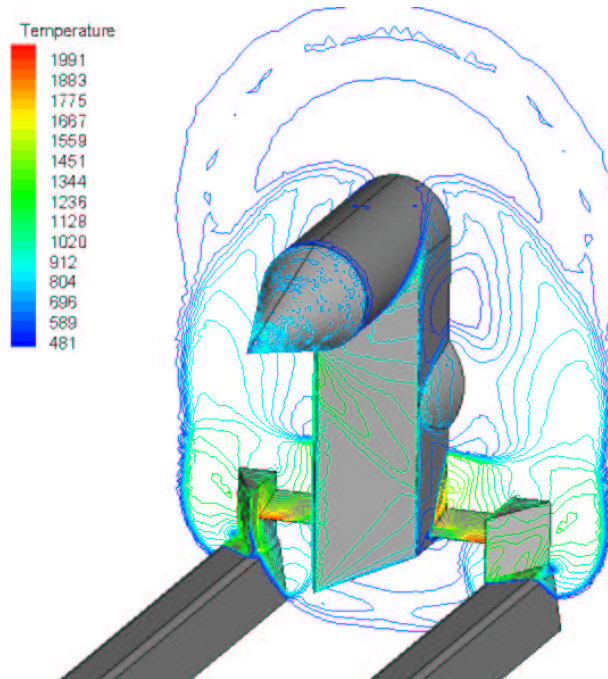


Figure 5.24 Surface Temperature Contours ($^{\circ}\text{R}$) for $M_{\infty} = 3.10$ in Helium

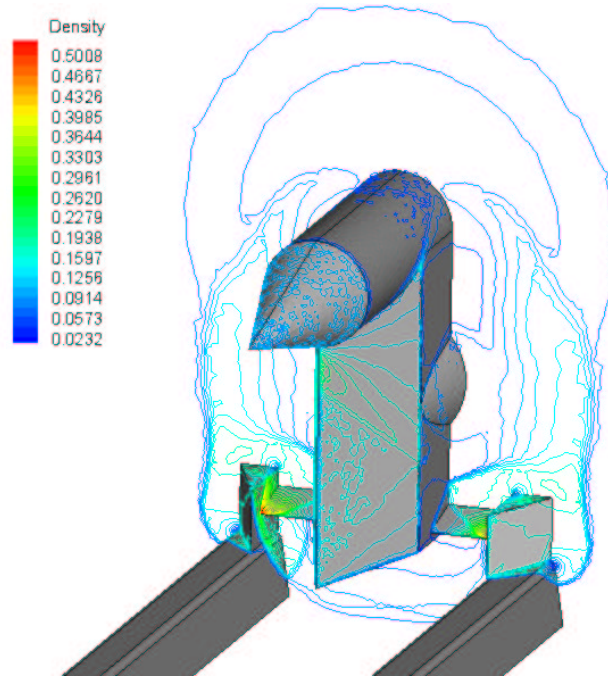


Figure 5.25 Surface Density Contours (lb_m/ft^3) for $M_\infty = 3.0$ in Air

Mach 3.0 in Air. Discontinuities in the flow properties are evidence of flow features that may be of interest (such as shock waves, expansion fans and contact surfaces). Density contour plots tend to show these discontinuities better than plots of other properties (such as pressure and temperature). Figure 5.25 shows the density contours for the $M_\infty = 3.0$ in air case. There is a region of high density where the bow shock impinges on the slipper wedge structure. This area is discussed in more detail below. Figure 5.26 also shows the density contours, but with decreased levels of contours, giving more resolution to the lower density areas. An area of low density around the lower edge of the vertical wedge can be clearly seen. This suggests that the flow expands around the edge. The streamlines visualized in Figures 5.27-5.29 show that this is the case. As the flow hits the vertical wedge, portions of the flow escape underneath the wedge, accelerating around the corner and creating the lower density areas. Farther back, this expansion causes part of the flow to go underneath the strut. This flow diversion could cause an upward (lift) force on the front of the sled. The structural design and performance prediction of the sled depends on an accurate knowledge of the lift forces present.

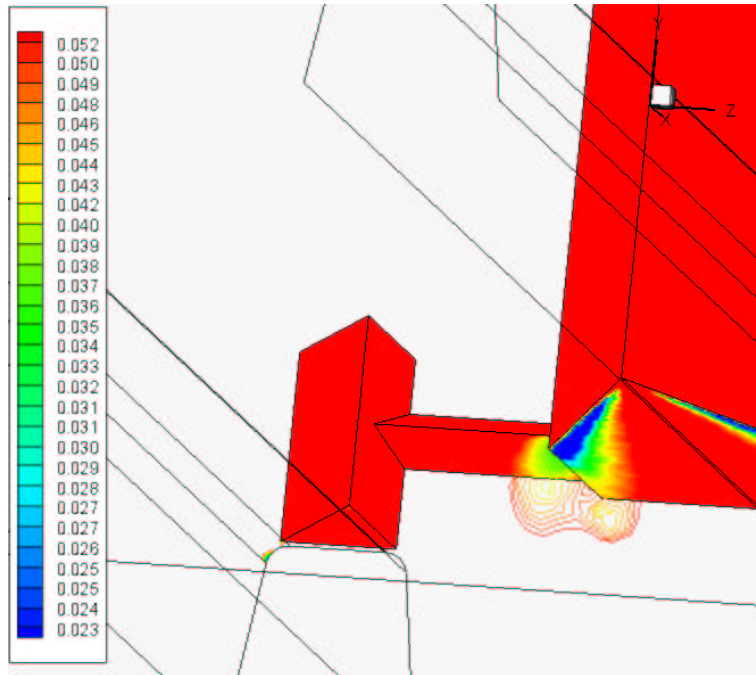


Figure 5.26 Surface Density Contour (lb_m/ft^3) Detail for $M_\infty = 3.0$ in Air

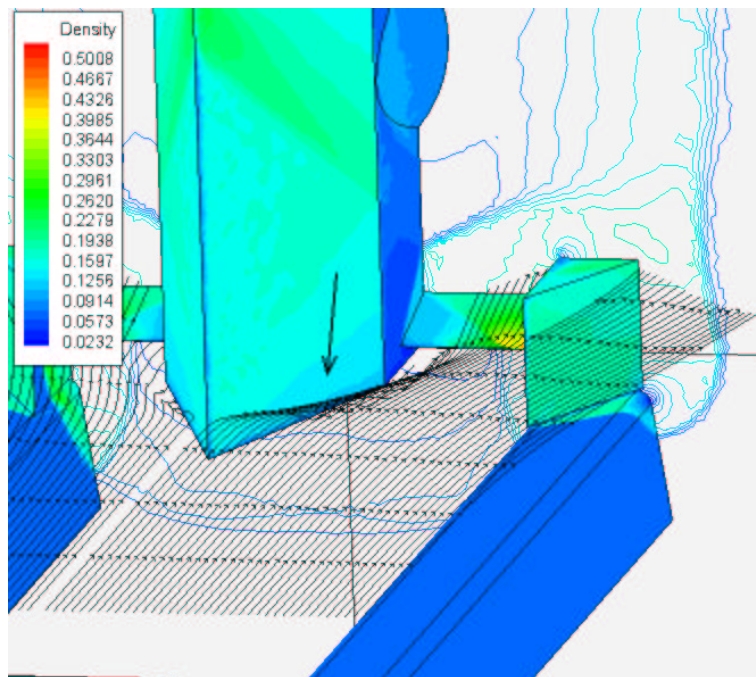


Figure 5.27 Streamlines at $y = 4$ Inches in Flow for $M_\infty = 3.0$ in Air

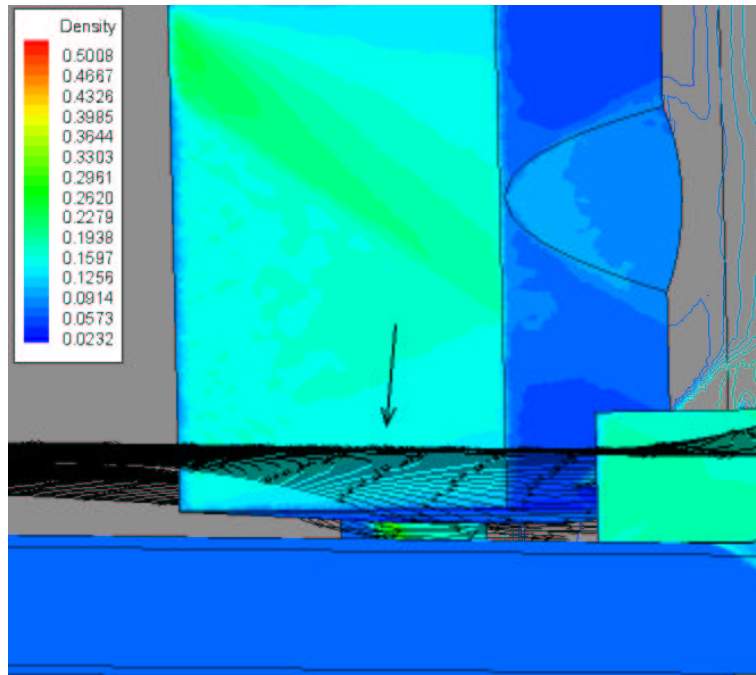


Figure 5.28 Side View of Streamlines in Flow for $M_\infty = 3.0$ in Air.

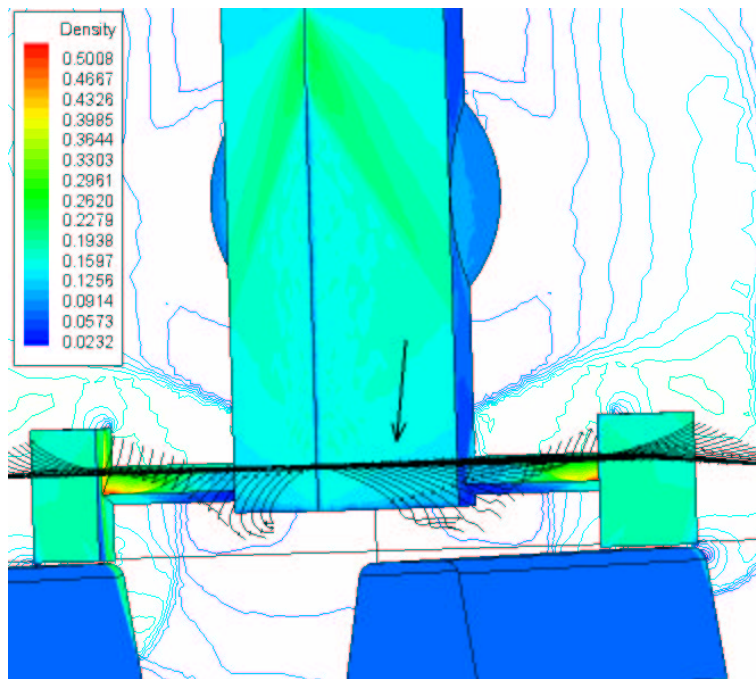


Figure 5.29 Front View of Streamlines in Flow for $M_\infty = 3.0$ in Air.

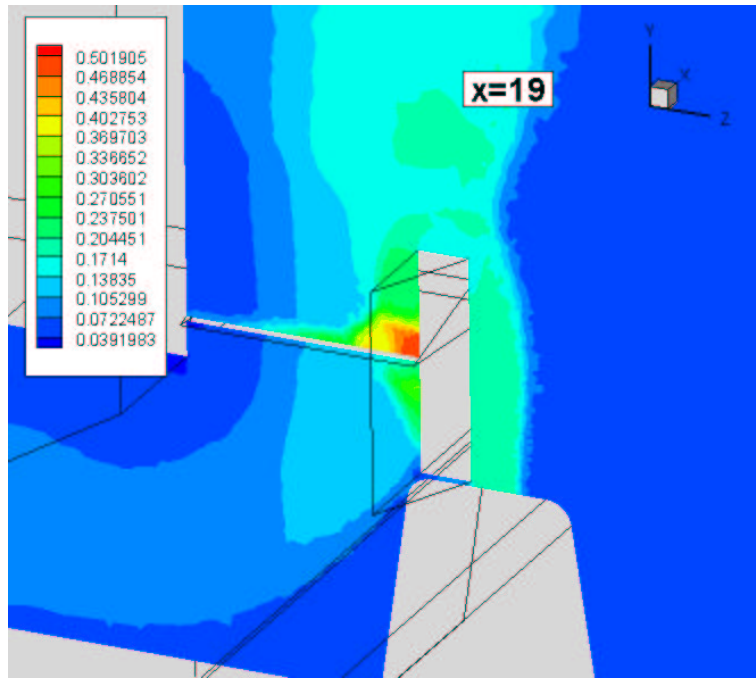


Figure 5.30 Density Contours (lb_m/ft^3) at $x = 19$ Inches for $M_\infty = 3.0$ in Air

Figure 5.30-5.37 show the flow features in the region where the shock impinges on the sled structure. Slices of the data are taken in the $x = 19$ and $y = 3.4$ inch planes. The shock generated by the vertical wedge hits the slipper wedge and reflects. However, the shock reflection then interacts with the expansion wave from the vertical wedge and also impinges on the surface of the strut wedge. These combined effects create a pocket of stagnated air (see the velocity contours in Figures 5.36 and 5.37) which, in turn, creates the high temperatures and pressures observed. These strong gradients would cause vibrations and heating on ablation regions that would adversely impact the sled performance and contribute to the gouging phenomenon in the slipper/rail gap.

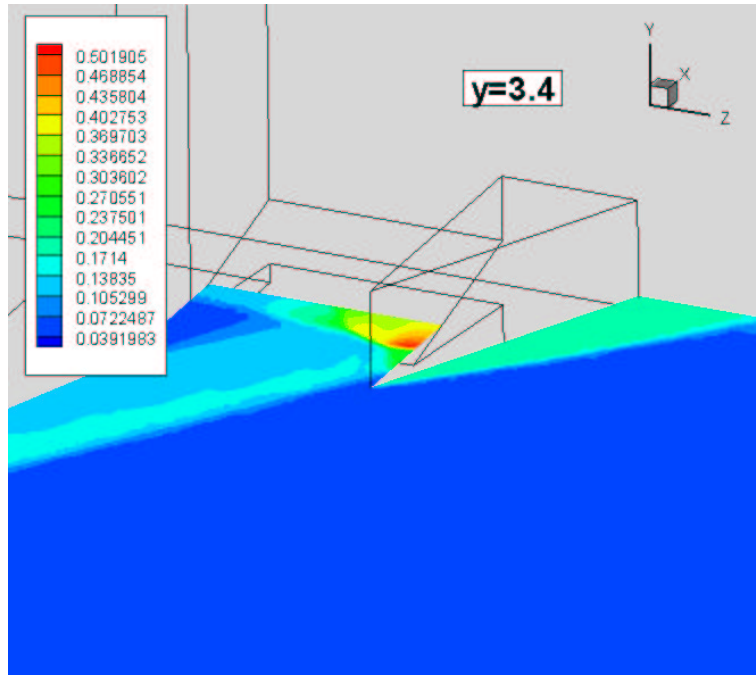


Figure 5.31 Density Contours (lb_m/ft^3) at $y = 3.4$ Inches for $M_\infty = 3.0$ in Air

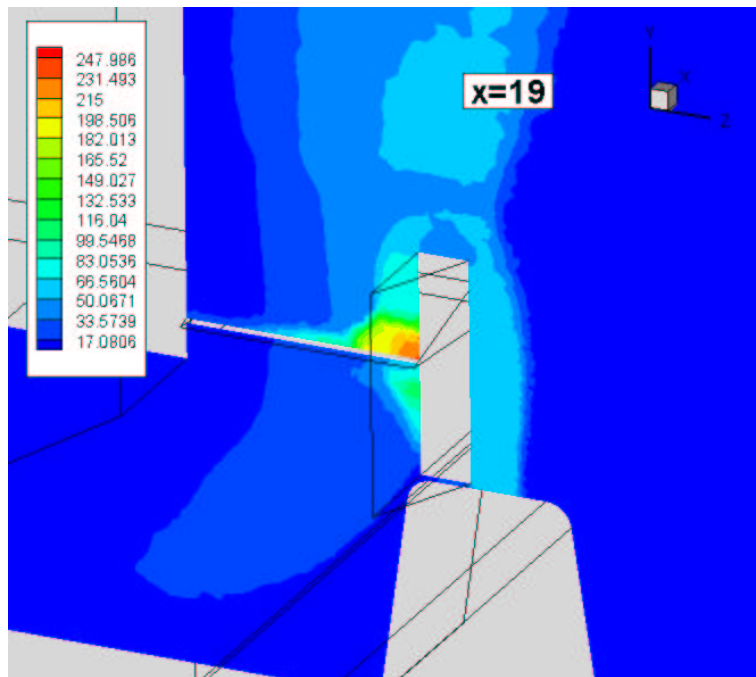


Figure 5.32 Pressure Contours (psi) at $x = 19$ Inches for $M_\infty = 3.0$ in Air

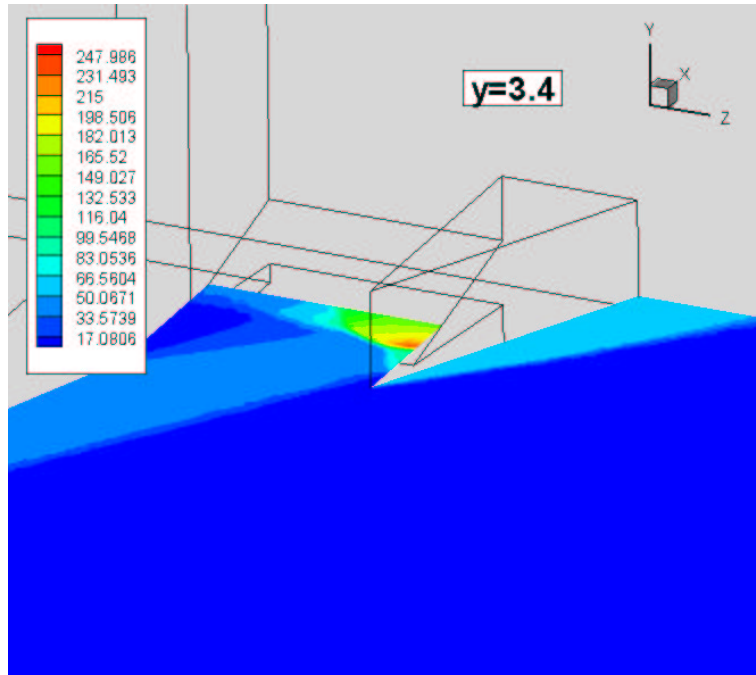


Figure 5.33 Pressure Contours (psi) at $y = 3.4$ Inches for $M_\infty = 3.0$ in Air

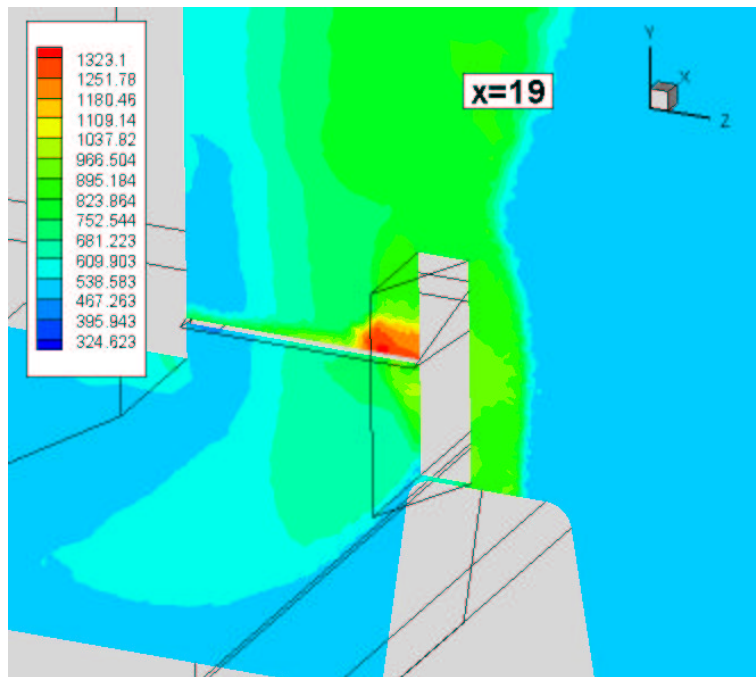


Figure 5.34 Temperature Contours ($^{\circ}\text{R}$) at $x = 19$ Inches for $M_\infty = 3.0$ in Air

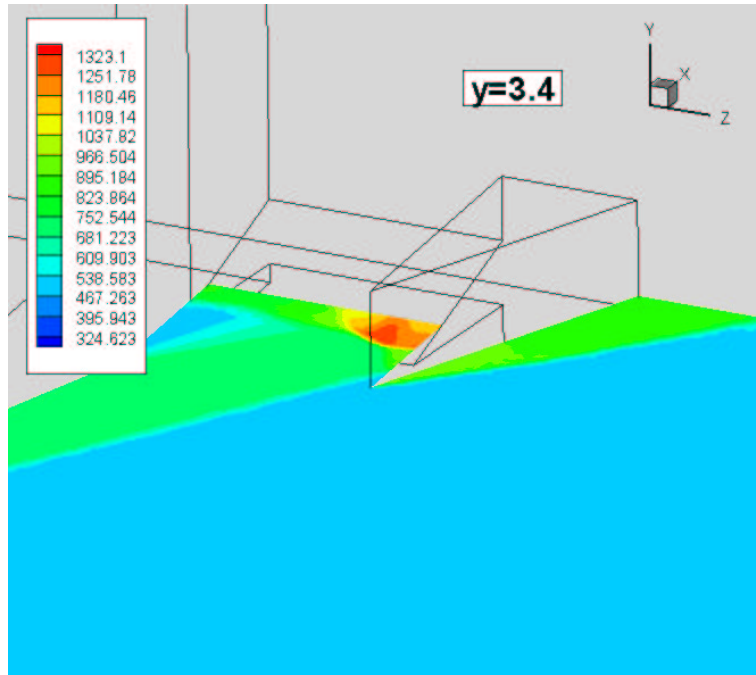


Figure 5.35 Temperature Contours (°R) at $y = 3.4$ for $M_{\infty} = 3.0$ in Air

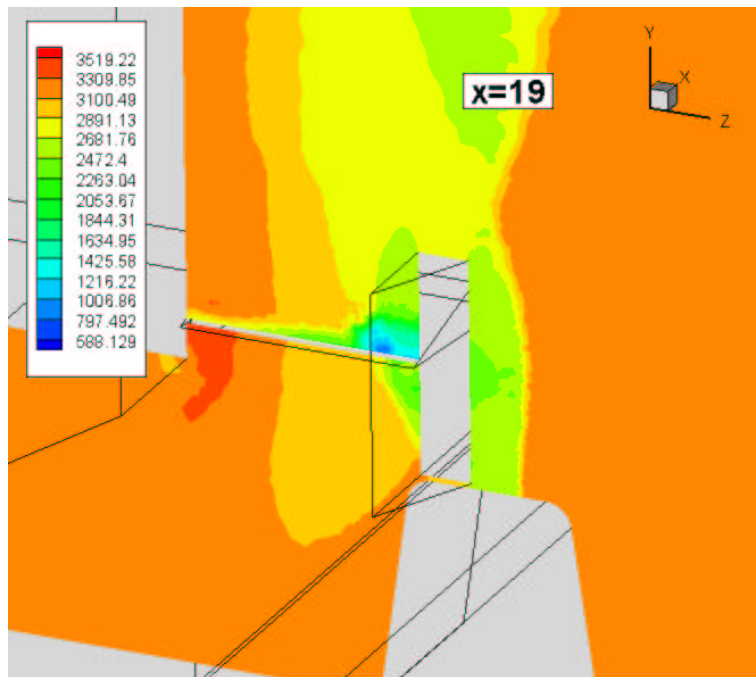


Figure 5.36 Velocity Magnitude Contours (ft/s) at $x = 19$ Inches for $M_{\infty} = 3.0$ in Air

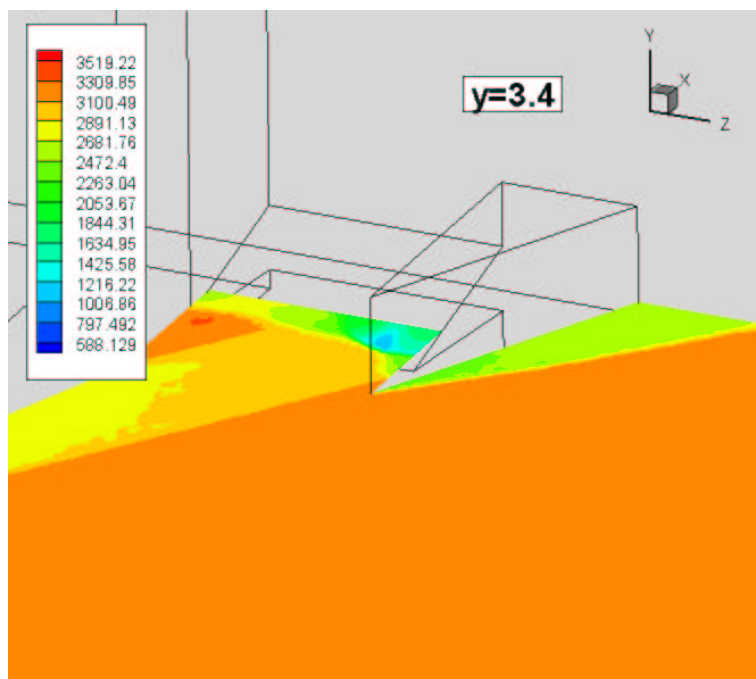


Figure 5.37 Velocity Magnitude Contours (ft/s) at $y = 3.4$ Inches for $M_\infty = 3.0$ in Air

Mach 1.02 in Helium. The same effects that create the large gradients in the $M_\infty = 3.0$ in air case are not seen in the $M_\infty = 1.02$ in helium case. This demonstrates the positive aspects of running in a helium environment; while the actual velocity of the sled is the same in both cases (3,300 fps), the same aerodynamic heating and loading is not seen in the helium environment because of the lower Mach number.

The density contours shown in Figure 5.38 suggest that the main regions of interest (those where there is high heating and loading) are simply those on the leading edges of the various wedges. Since there are no shocks reflecting off the structures, the stagnation points on the leading edges are the locations of highest temperatures and pressures.

Figures 5.39-5.43 show the density contours on constant- x planes. The flow stagnates at the leading edge of the large vertical wedge, then is mildly expanded along the wedge. At the shoulder of the wedge, the flow expands rapidly. The flow above the rounded blister immediately ahead of the rocket motor stays at the lower density achieved by the expansion around the shoulder, while the flow below the blister is compressed due to the compression caused by the stagnated flow near the strut wedge.

The fact that the flow is relatively simple is also shown by the constant- y plane contours in Figures 5.44-5.46. The flow stagnates at the leading edge, expands mildly along the leading edge of the vertical wedge, and then rapidly expands at the wedge shoulders. There are also stagnation regions on the leading edges of the slipper wedges. The pressures and temperatures are highest when the flow is compressed and are lowest in the expansion regions.

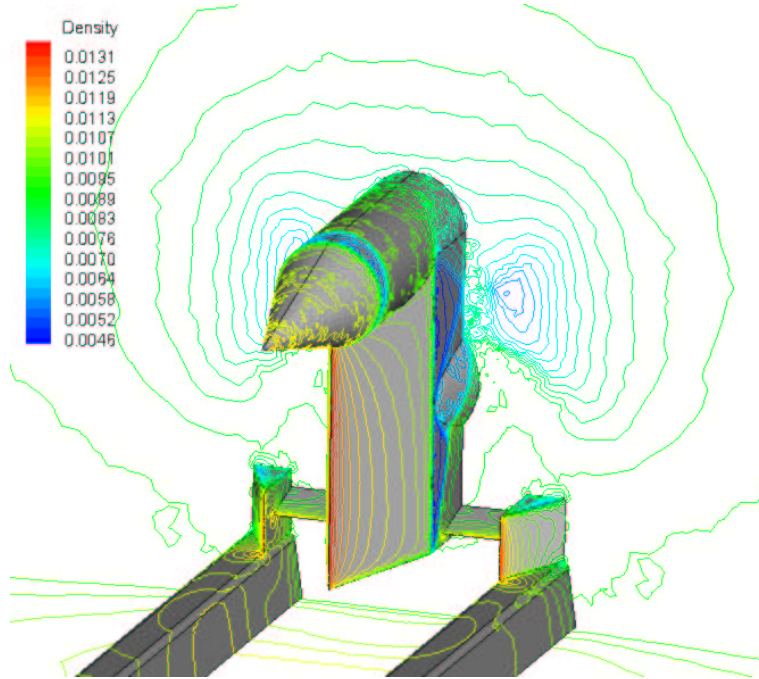


Figure 5.38 Surface Density Contours (lb_m/ft^3) for $M_\infty = 1.02$ in Helium

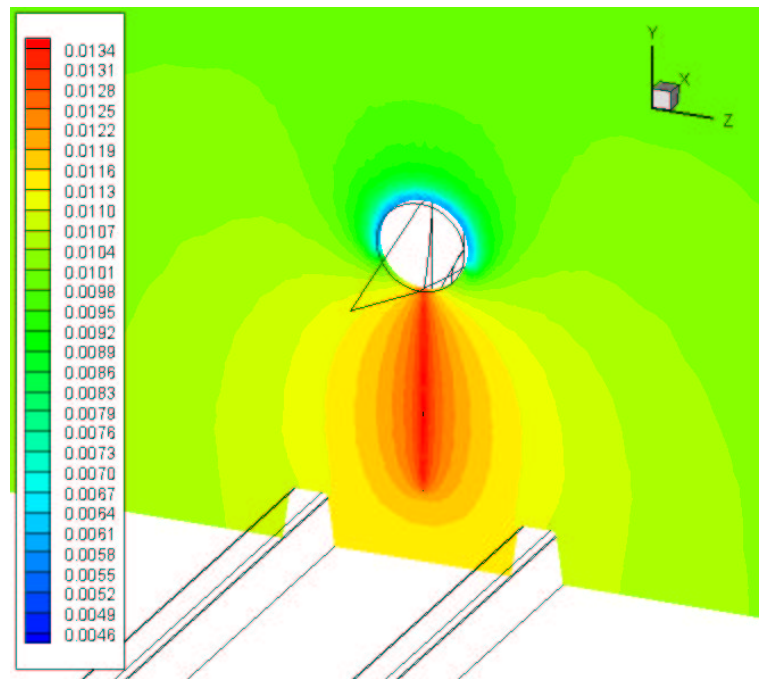


Figure 5.39 Density Contours (lb_m/ft^3) at $x = 0$ Inches for $M_\infty = 1.02$ in Helium

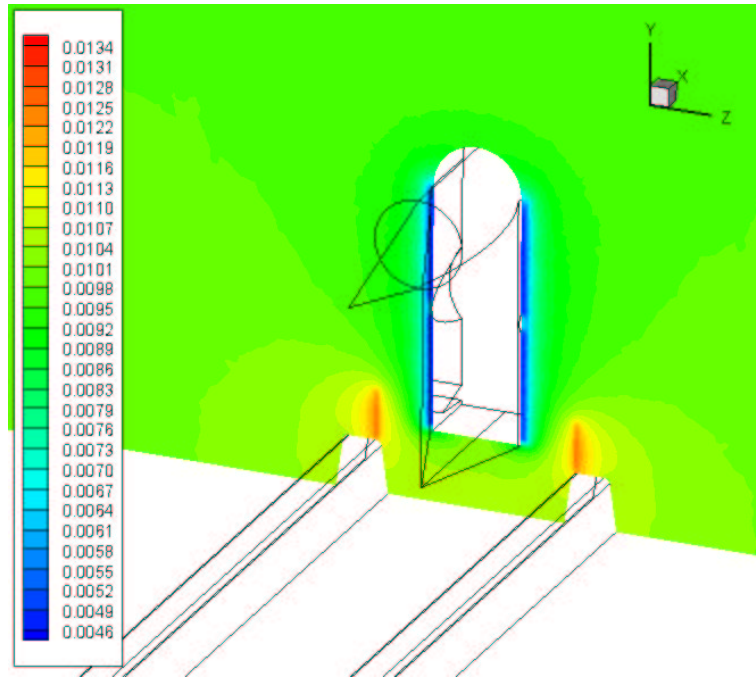


Figure 5.40 Density Contours (lb_m/ft^3) at $x = 16$ Inches for $M_\infty = 1.02$ in Helium

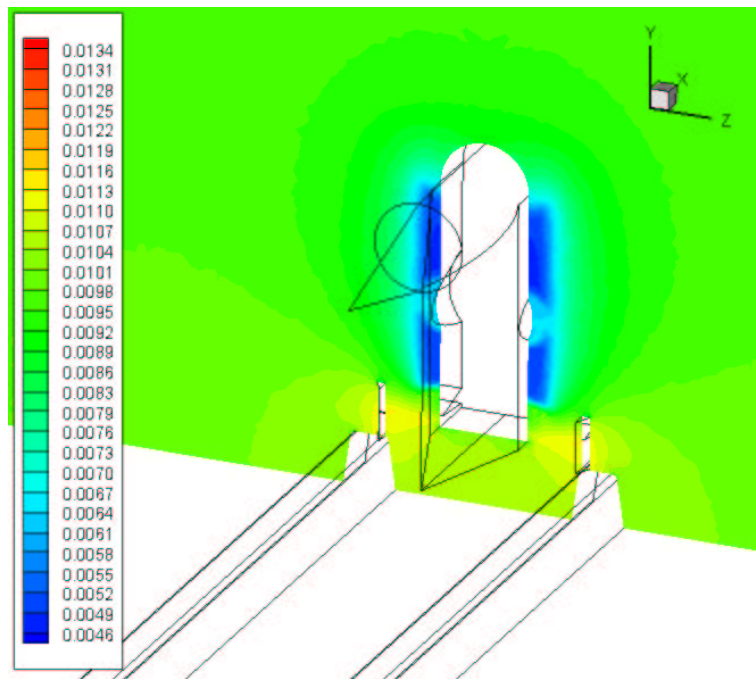


Figure 5.41 Density Contours (lb_m/ft^3) at $x = 18$ Inches for $M_\infty = 1.02$ in Helium

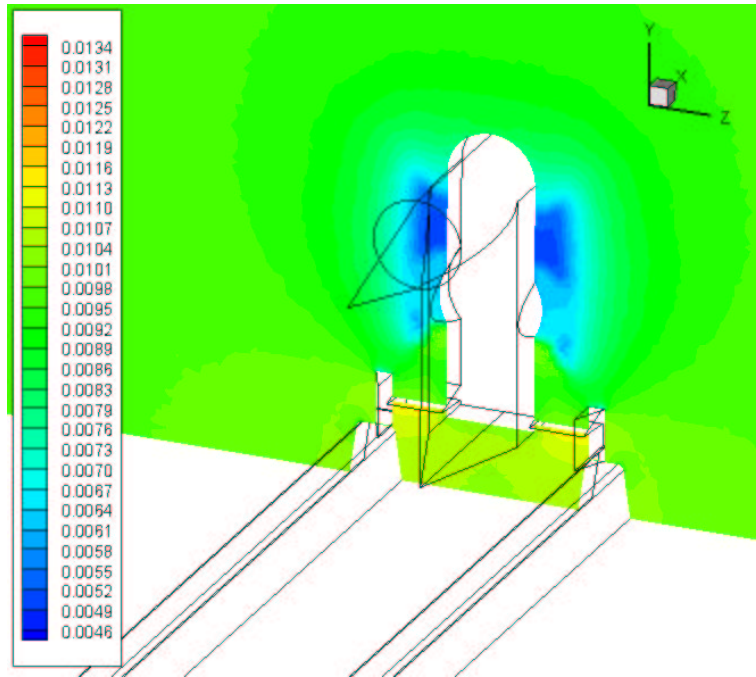


Figure 5.42 Density Contours (lb_m/ft^3) at $x = 20$ Inches for $M_\infty = 1.02$ in Helium

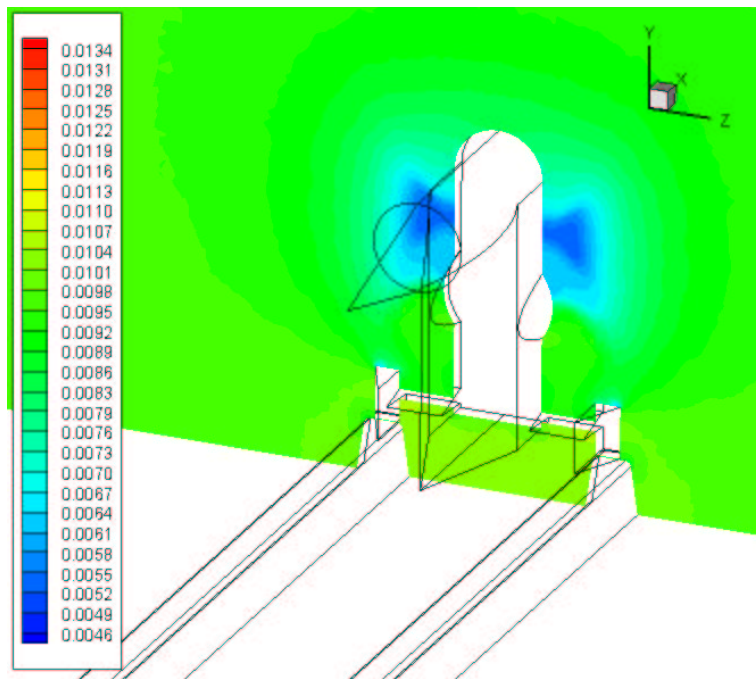


Figure 5.43 Density Contours (lb_m/ft^3) at $x = 22$ Inches for $M_\infty = 1.02$ in Helium

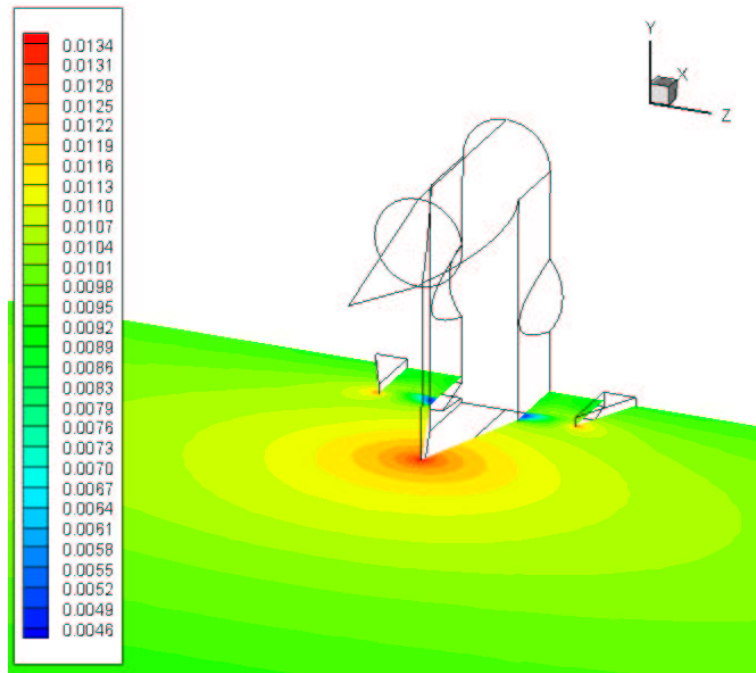


Figure 5.44 Density Contours (lb_m/ft³) at $y = 5$ Inches for $M_\infty = 1.02$ in Helium

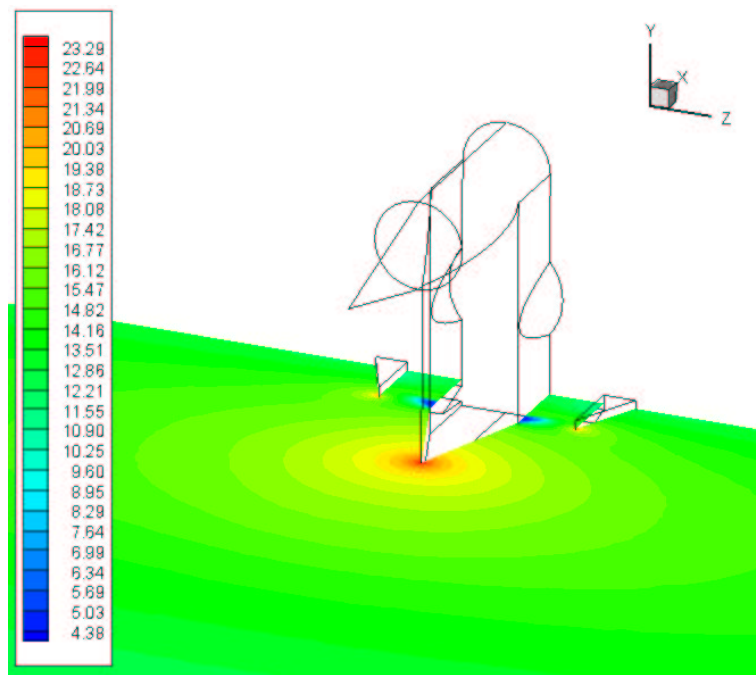


Figure 5.45 Pressure Contours (psi) at $y = 5$ Inches for $M_\infty = 1.02$ in Helium

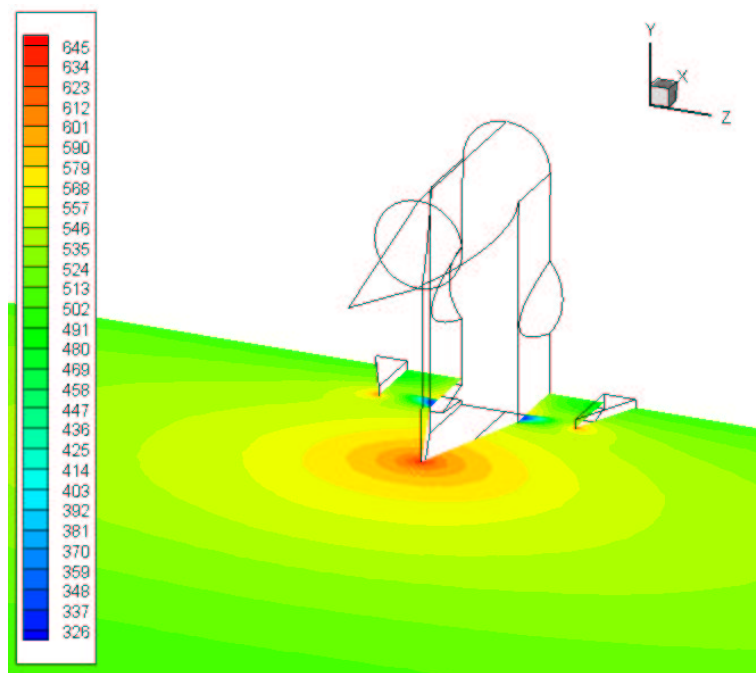


Figure 5.46 Temperature Contours (psi) at $y = 5$ Inches for $M_\infty = 1.02$ in Helium

Slipper/Rail Gap

The properties of the flow in the slipper/rail gap is of primary importance, due to the gouging damage that can be caused to the slipper and rail. Although the actual gap was not included in the computational model, an idea of the flow in the slipper/rail gap can be estimated by looking at the flow immediately upstream in the gap between the rail and the slipper wedge. Again, it is emphasized that the current computational results are inviscid results; viscous effects in the boundary layer would certainly affect the pressures and temperatures that develop in the small gap area.

Streamlines in the slipper/rail gap area for both the $M_\infty = 3.0$ in air and $M_\infty = 1.02$ in helium cases are shown in Figures 5.47-5.50. The streamlines are superimposed on density contour plots. The streamlines shown in Figures 5.47 and 5.48 were generated by following virtual particles inserted with equal spacing at $y = 0.2$ inches, upstream of the gap and following them downstream. This y -plane was higher than the upper surface of the gap (which is at $y = 0$ inches). The streamlines for the $M_\infty = 3.0$ in air case (Figure 5.47 show that the mass flowing *above* the gap is what actually flows *through* the gap. There is, most likely, a shock wave at the entrance to the gap that turns the flow downward and into the gap. This is not seen for the $M_\infty = 1.02$ in helium case; there, the particles starting at $y = 0.2$ inches do not enter the gap, but are diverted around the slipper wedge. The streamline visualization for the air case also shows that a small number of streamlines actually flow through the gap compared with the majority that are diverted around the gap. This suggests that the mass flow through the gap is rather small.

Figures 5.49 and 5.50 were generated by inserting virtual particles at equal spacing midway through the gap (at $y = -0.0625$ inches) and following their paths *upstream*. These, then, show the path taken by the particles that actually enter the gap. In both the air and the helium cases, it is evident that the mass flowing through the gap comes from the region just inside the rails. It is also evident that the mass flowing through the gap is relatively small, since the streamlines in the gap come from a small region upstream of the slipper wedge.

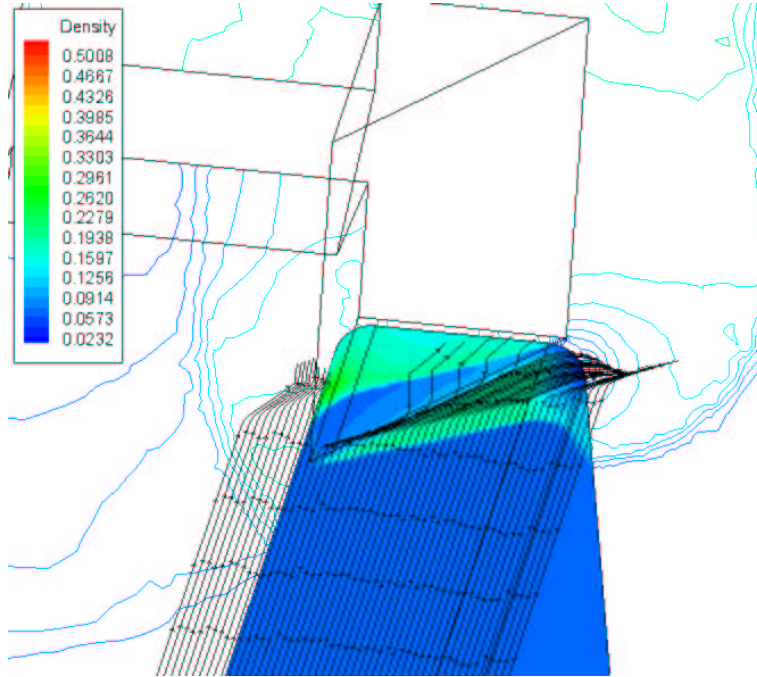


Figure 5.47 Streamlines in Slipper/Rail Gap Area ($y = 0.2$ Inches) for $M_\infty = 3.0$ in Air.

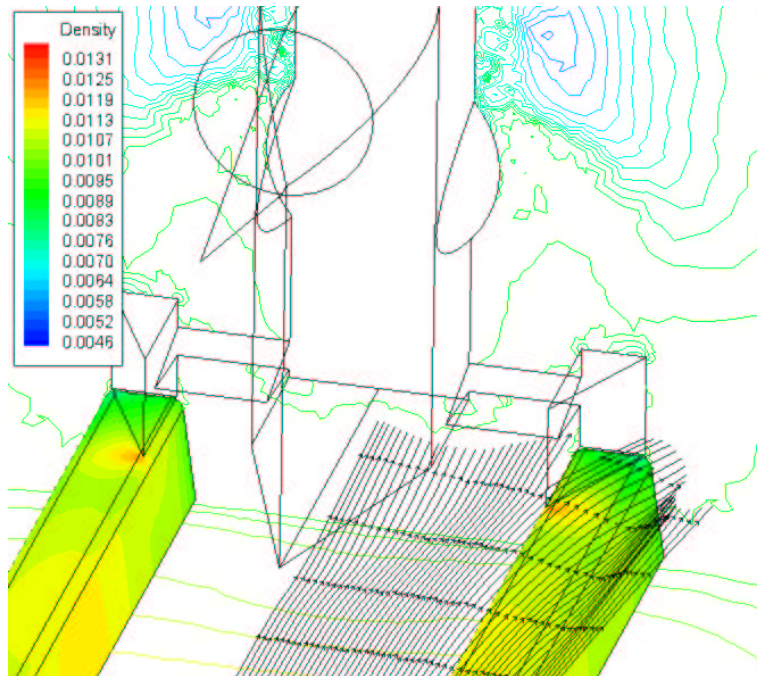


Figure 5.48 Streamlines in Slipper/Rail Gap Area ($y = 0.2$ Inches) for $M_\infty = 1.02$ in Helium

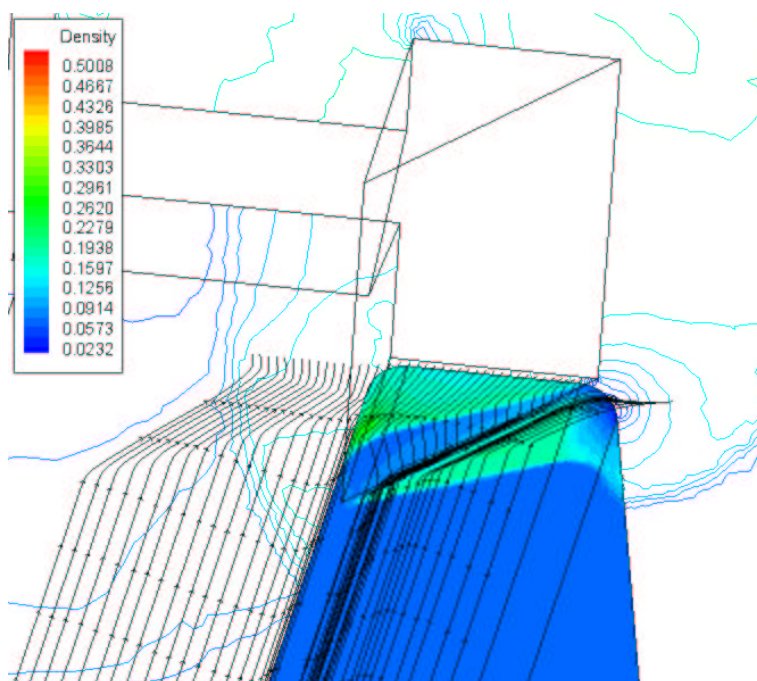


Figure 5.49 Streamlines in Slipper/Rail Gap Area ($y = -0.0625$ Inches) for $M_\infty = 3.0$ in Air.

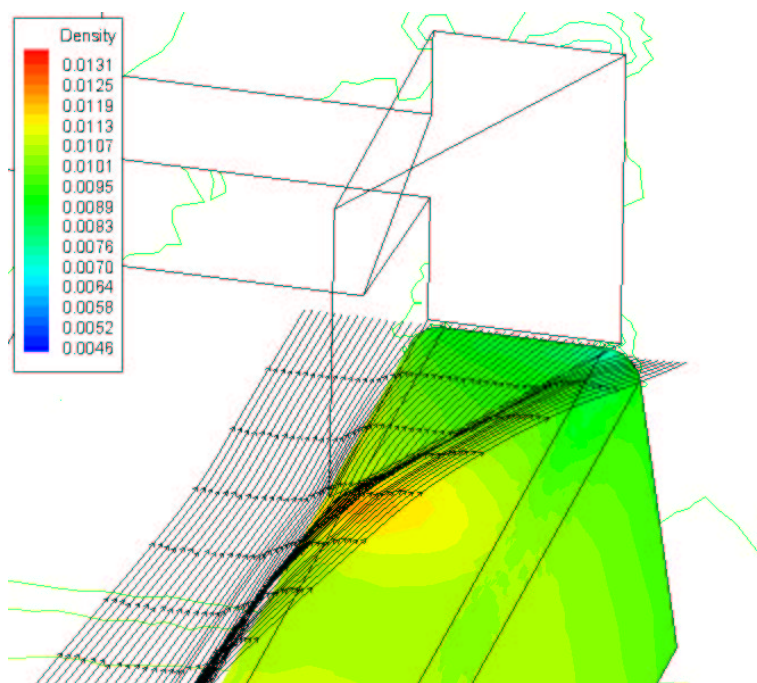


Figure 5.50 Streamlines in Slipper/Rail Gap Area ($y = -0.0625$ Inches) for $M_\infty = 1.02$ in Helium

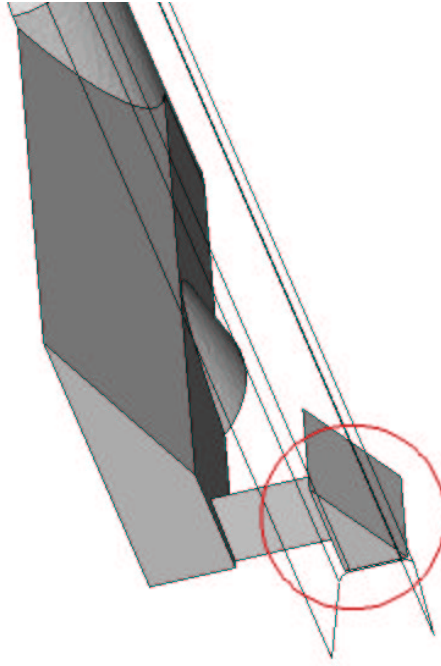


Figure 5.51 Detail of Slipper/Rail Gap Area (Looking Up Through Transparent Rail)

Pressure and temperature data was also taken along the lower surface of the slipper wedge shown in Figure 5.51 along three lines as defined in Figure 5.52. Line 1 runs along the outflow plane in the z -direction. Line 2 runs along the inboard side of the slipper wedge in the x -direction. Line 3 runs along the outboard side of the slipper wedge. The lengths in each case have been normalized to run from 0 to 1. The data were taken along each of the lines at the surface of the wedge ($y = 0$ inches), the middle of the gap ($y = -0.0625$ inches) and at the upper rail surface ($y = -0.125$ inches), and are plotted in Figures 5.53-5.58. The properties in each case are relatively independent of the y -position (vertically), with the possible exception of Line 2 (inboard edge of the slipper wedge).

The pressure and temperature distributions along the outflow plane (Figures 5.53 and 5.54) follow similar trends. For the air case, the pressures and temperatures are highest on the inboard side after being compressed through the shock generated by the strut wedge; they decrease along the outboard side due to the expansion of the air past the edge of the rail (the flow is forced along the wedge and then expands downward at the edge of the

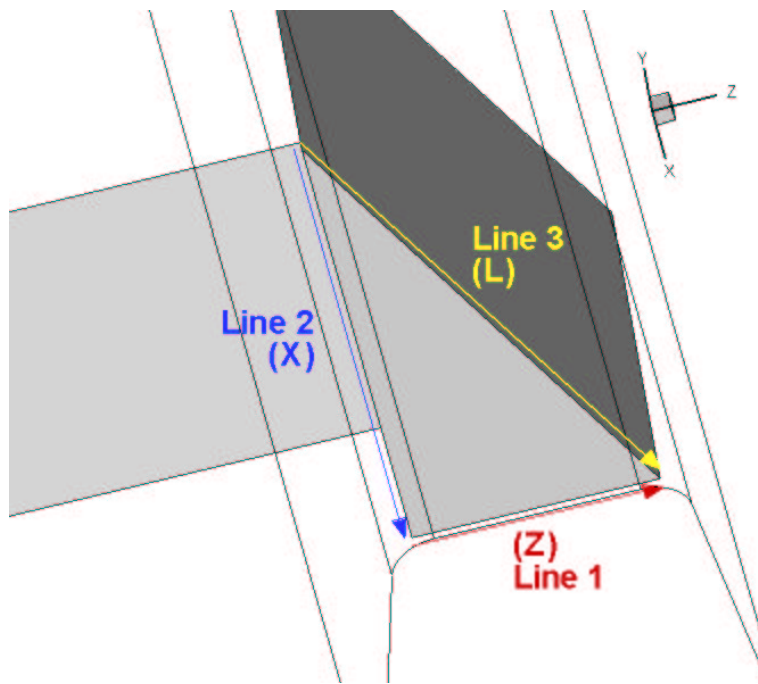


Figure 5.52 Definitions of Lines Used in Plots (Looking Up Through Rail to Bottom of Slipper Wedge)

rail). Since there is no shock generated in the helium case, the pressure and temperatures are much lower than in the air.

The effects of the shock impinging on the wedge surface are clearly seen in the plots along the inboard side (Figures 5.55 and 5.56). The spikes are due to the impinging shock and the resulting pressure gradients would likely cause vibrations in this region. Again, the helium values and gradients are lower because there is no shock impinging in this region.

Similar trends can be seen along the outboard side of the slipper wedge (Figures 5.57 and 5.58). The air case demonstrates higher pressures and temperatures due to the shock off the leading edge. The pressure and temperature at the leading edge are lower because that portion is just in front of the shock. The values decrease near the outflow plane due to the expansion around the edge of the rail. For the helium case, the values are highest at the leading edge in the stagnation region and they drop off as the flow progresses back and expands.

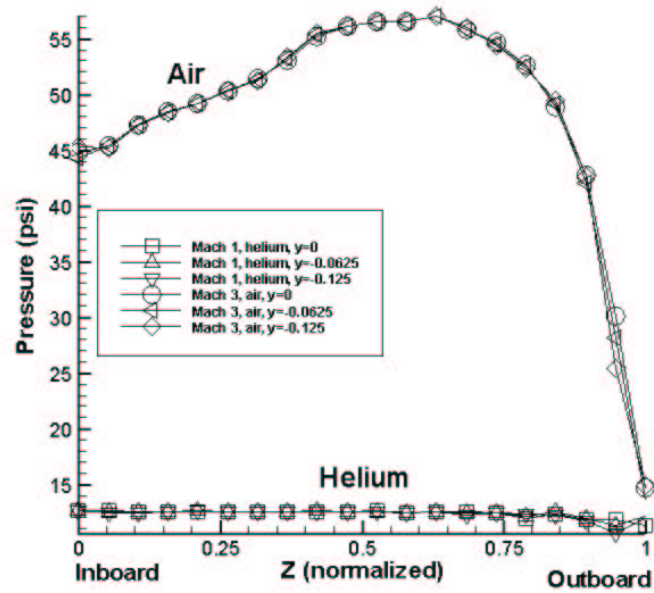


Figure 5.53 Pressure Distribution Along Line 1 (Outlet)

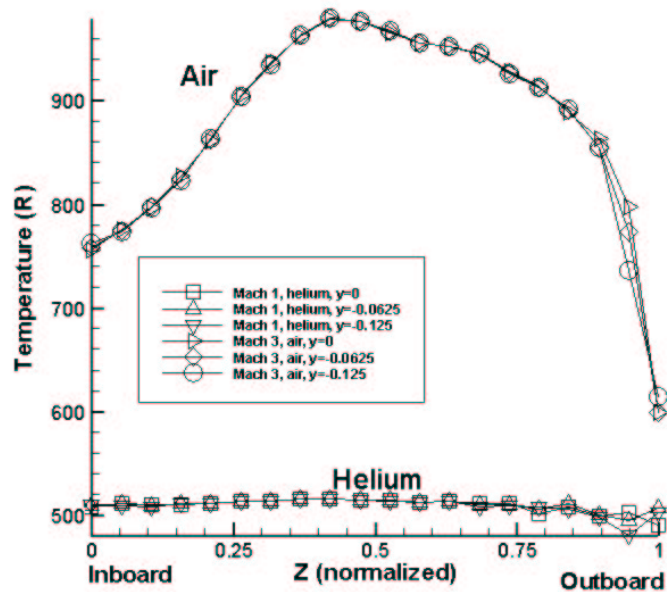


Figure 5.54 Temperature Distribution Along Line 1 (Outlet)

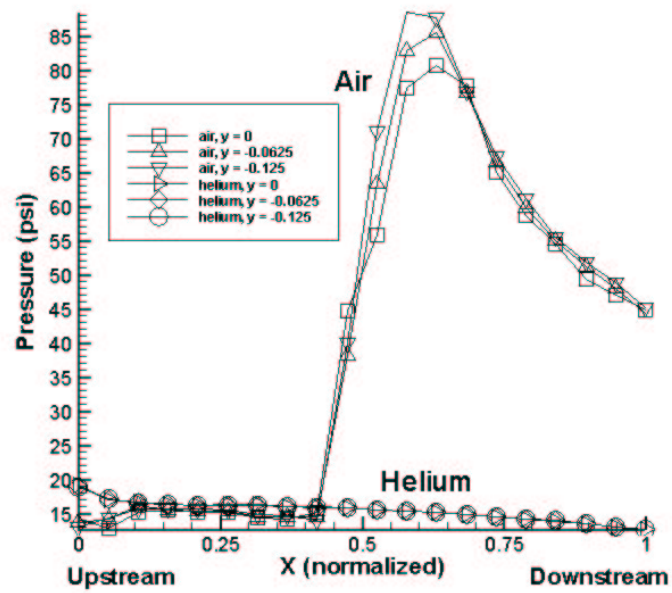


Figure 5.55 Pressure Distribution Along Line 2 (Inboard Side)

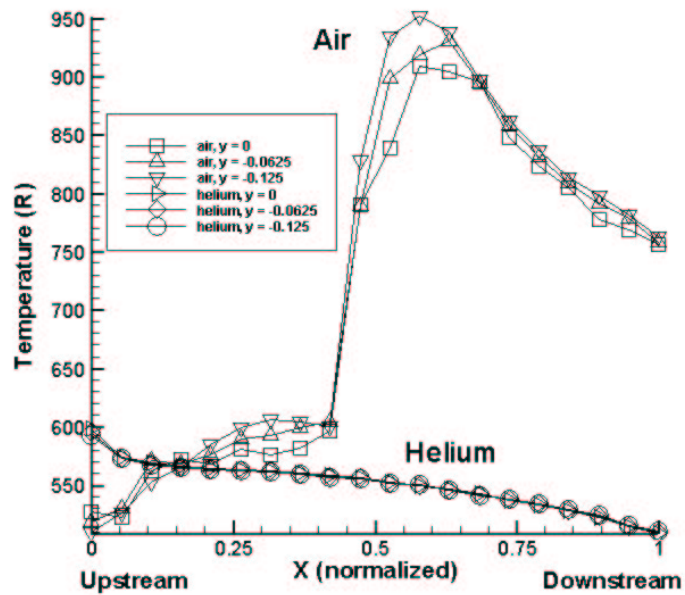


Figure 5.56 Temperature Distribution Along Line 2 (Inboard Side)

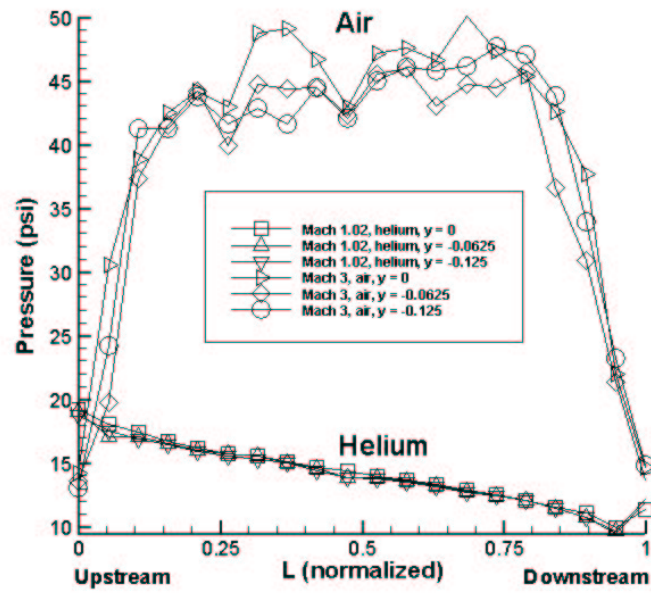


Figure 5.57 Pressure Distribution Along Line 3 (Outboard Side)

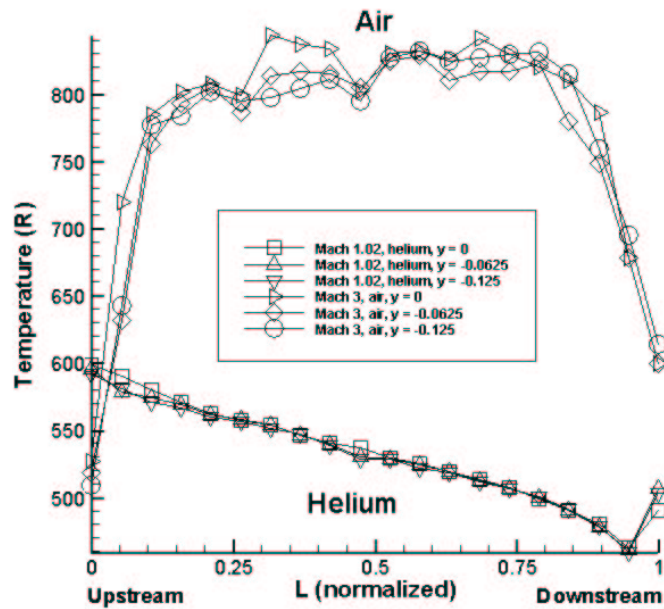


Figure 5.58 Temperature Distribution Along Line 3 (Outboard Side)

Unsteady, Inviscid Flow

Due to the vast amount of data generated with the unsteady computation and the difficulty in visualizing the results on paper, only the pressure solution will be presented here, although the same trends occur for the temperature and density values.

A total of 7.5 milliseconds were modeled with the unsteady calculation, with 1,500 time steps ($\Delta t = 5 \times 10^{-6}$ seconds). Snapshots of the solution were taken every 200 time steps, generating 750 animation frames. Of those 750, nine are presented here.

As discussed previously, the unsteady computation was set up by simply changing the boundary condition on the pressure-far-field boundary to be 100% helium at $M_\infty = 1.02$, or 3,300 fps. Figures 5.59-5.62 show the mass fraction of air during a portion of the computation. The helium diffuses through the domain within a period of 5 milliseconds. It should be noted that the surface boundaries still reflect a composition of 100% air due to the way the boundary conditions are implemented in FLUENT. Several different methods of implementing the boundary conditions were explored, but all gave the same results.

These frames illustrate a difficulty with modeling the unsteady transition from air to helium as the sled enters a tent. Presumably, the transition should take place in a constant- x plane – that is, the helium should diffuse from upstream of the sled only. However, due to the shape of the pressure-far-field boundary, helium was introduced into the domain as a function of x also (it appears as though the helium were diffusing in from the z_{max} boundary as well). Although this may not be entirely accurate, the sled is engulfed completely in the helium environment in less than 2 milliseconds and the inaccuracies may be negligible. The simulation would most likely be more accurate if different boundary zones were implemented to model the transition better.

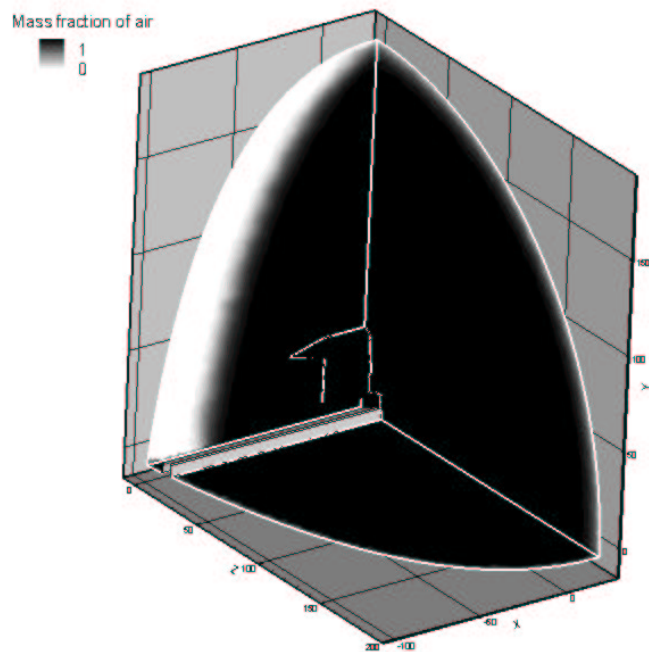


Figure 5.59 Mass Fraction of Air at $t = 1.0 \times 10^{-3}$ Seconds

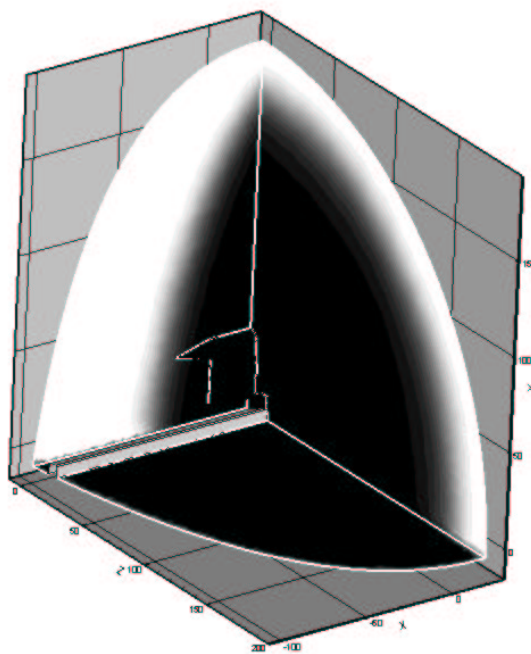


Figure 5.60 Mass Fraction of Air at $t = 2.0 \times 10^{-3}$ Seconds

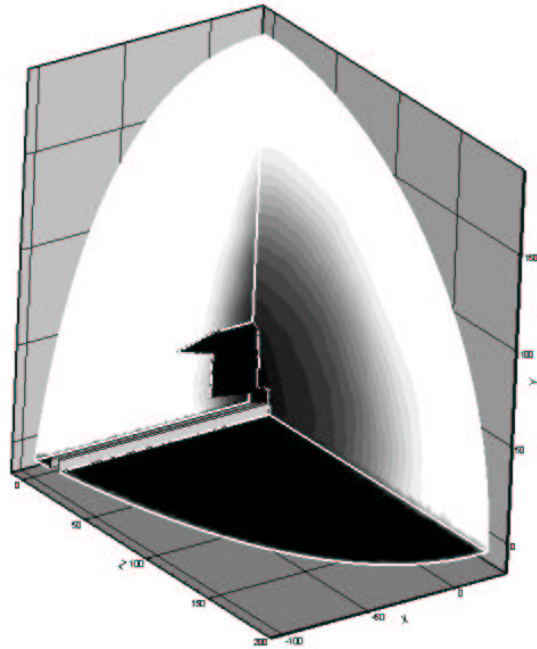


Figure 5.61 Mass Fraction of Air at $t = 3.0e - 3$ Seconds

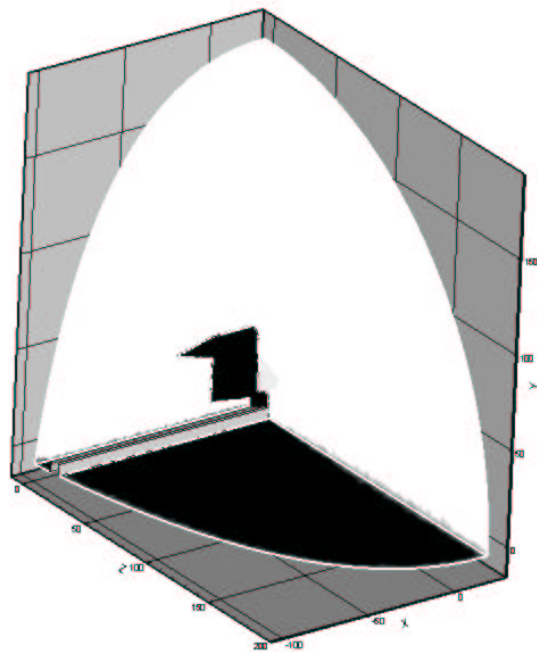


Figure 5.62 Mass Fraction of Air at $t = 4.0e - 3$ Seconds

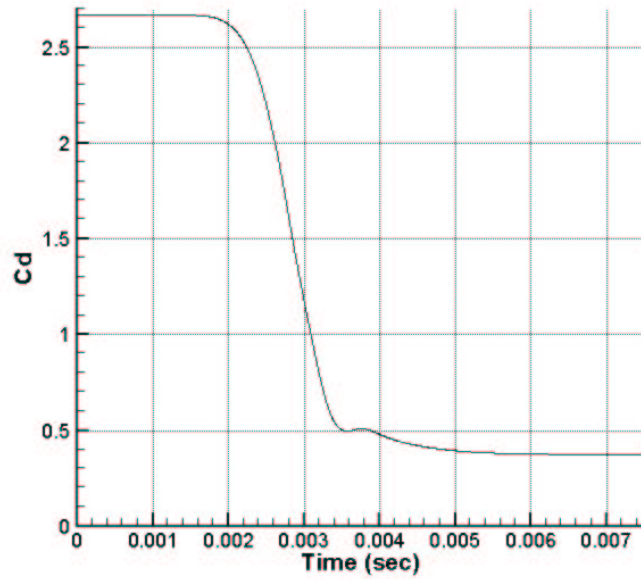


Figure 5.63 Drag Coefficient During Air-to-Helium Transition

The drag coefficient changes during the air-to-helium transition is shown in Figure 5.63. As the sled begins to enter the helium at about 2 milliseconds, the drag coefficient drops. The entire sled is engulfed in helium a little before 4 milliseconds. The slight bounce in the drag coefficient as it bottoms out, begins to increase, then decreases again demonstrates the dynamic effect as the pressures stabilize after the sled has completely entered the helium environment. The unsteadiness eventually settles out to a steady-state solution after 6 milliseconds.

Figures 5.64-5.81 give a good idea of the pressure distribution throughout the transition. These frames span the time from $t = 2.0 \times 10^{-3}$ to $t = 6.0 \times 10^{-3}$. It is important to note that the range of pressure contours are different for each frame; the optimal contour level range was computed automatically by Tecplot to give the best resolution of contours at each time step.

During the transition, the maximum pressures decrease and the shock angles increase, giving the appearance that the contours "spread out" (that is, the shocks don't lay so closely to the sled itself, but fan out into the freestream). The dynamic effect seen in the

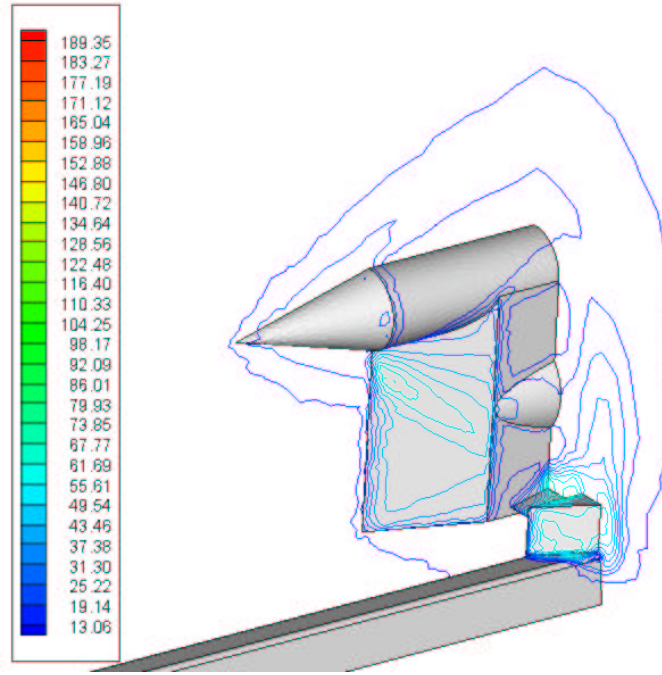


Figure 5.64 Static Pressure (psi) Contours at $t = 2.0 \times 10^{-3}$ Seconds

drag coefficient is also seen in the pressure contours as the Mach line extending upward from the expansion around the shoulder of the vertical wedge continues to come forward (Figure 5.69) and then settles further back on the body (Figure 5.72).

These frames also show that the maximum pressure areas migrate from the corner near the slipper wedge (where the shock impinges on the structure) and settles on the stagnation region on the leading edge of the wedges. The final steady-state solution is the familiar solution discussed previously for the $M_\infty = 1.02$ in helium case.

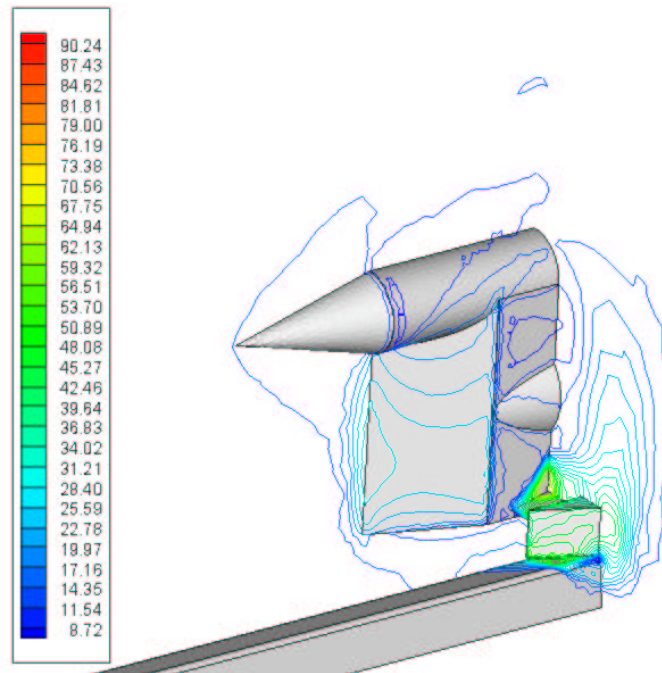


Figure 5.65 Static Pressure (psi) Contours at $t = 3.0 \times 10^{-3}$ Seconds

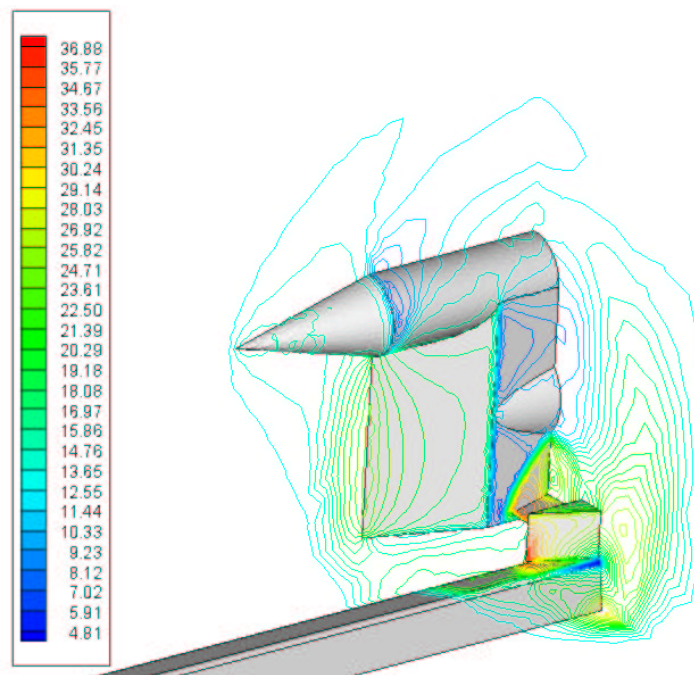


Figure 5.66 Static Pressure (psi) Contours at $t = 3.3 \times 10^{-3}$ Seconds

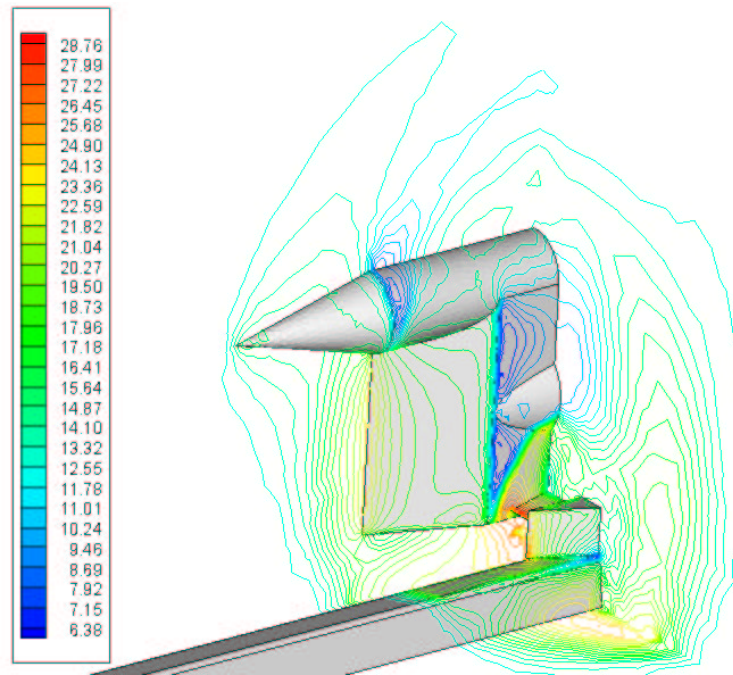


Figure 5.67 Static Pressure (psi) Contours at $t = 3.5 \times 10^{-3}$ Seconds

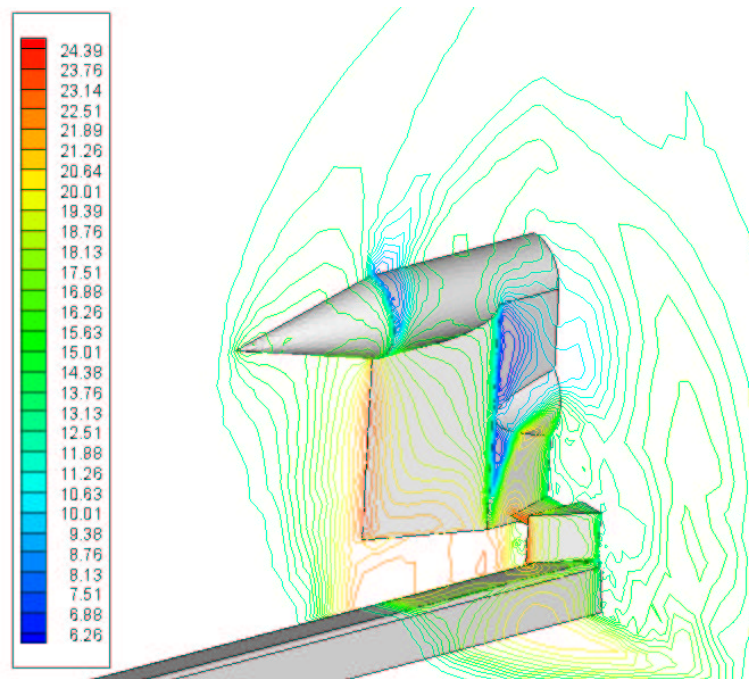


Figure 5.68 Static Pressure (psi) Contours at $t = 3.7 \times 10^{-3}$ Seconds

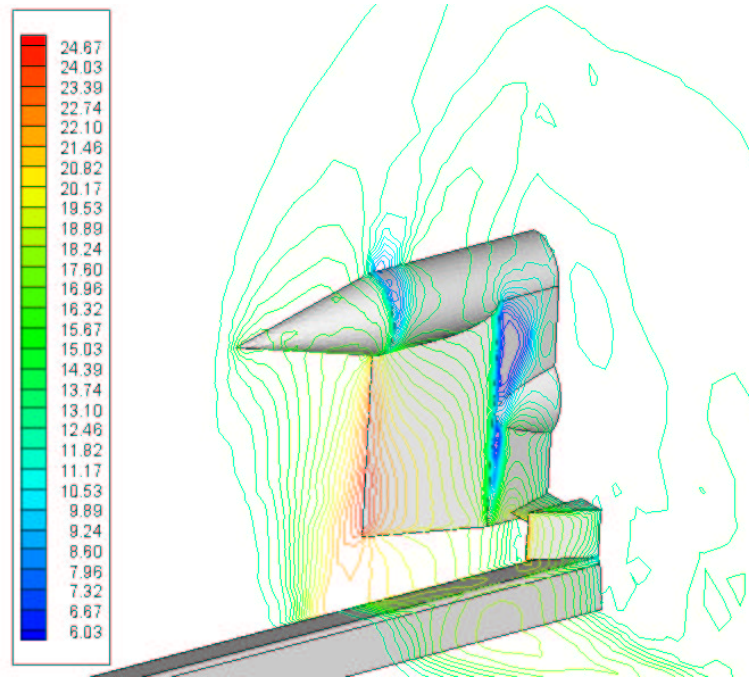


Figure 5.69 Static Pressure (psi) Contours at $t = 4.0 \times 10^{-3}$ Seconds

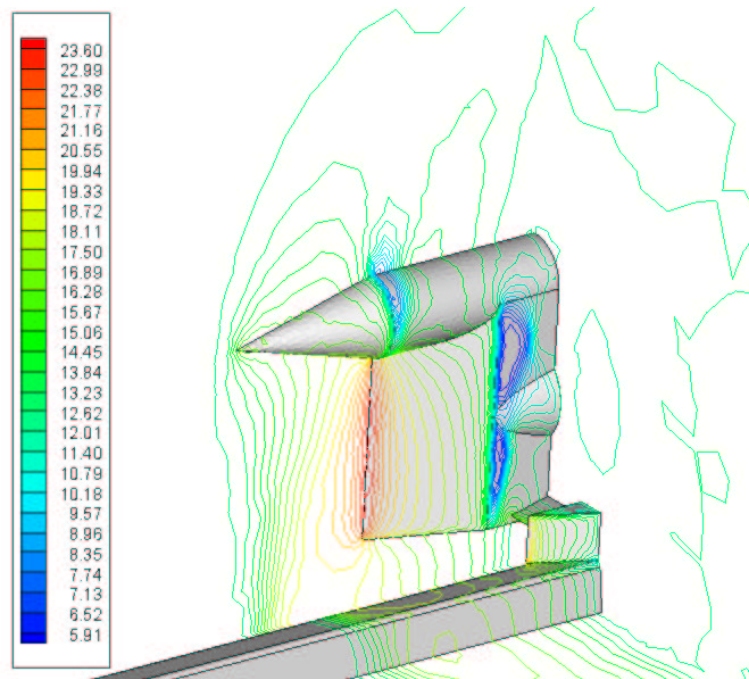


Figure 5.70 Static Pressure (psi) Contours at $t = 4.5 \times 10^{-3}$ Seconds

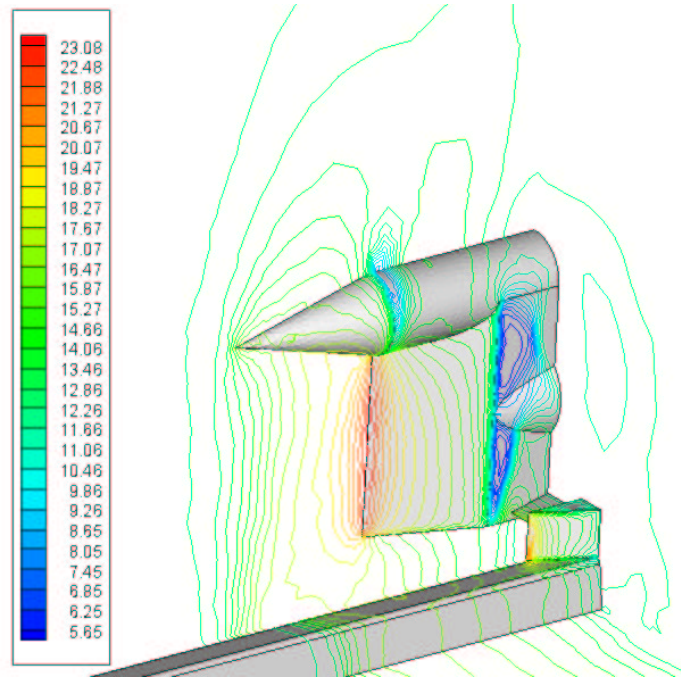


Figure 5.71 Static Pressure (psi) Contours at $t = 5.0 \times 10^{-3}$ Seconds

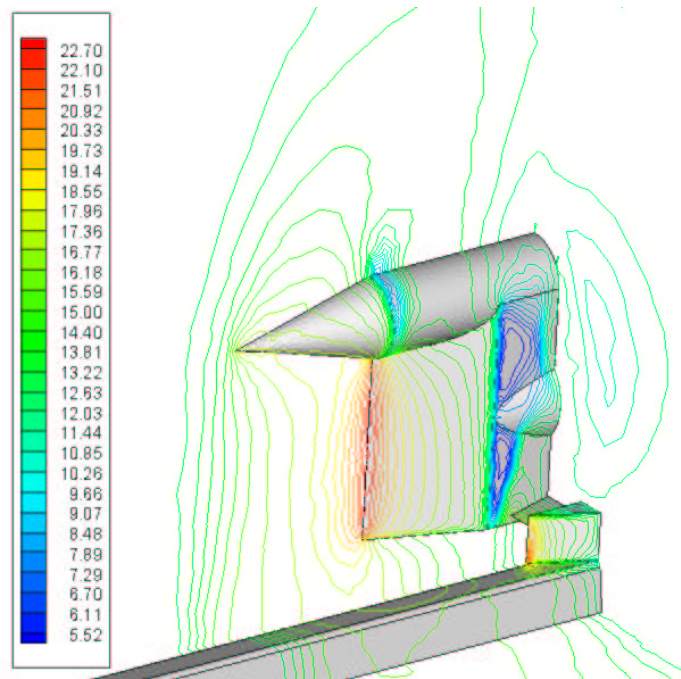


Figure 5.72 Static Pressure (psi) Contours at $t = 6.0 \times 10^{-3}$ Seconds

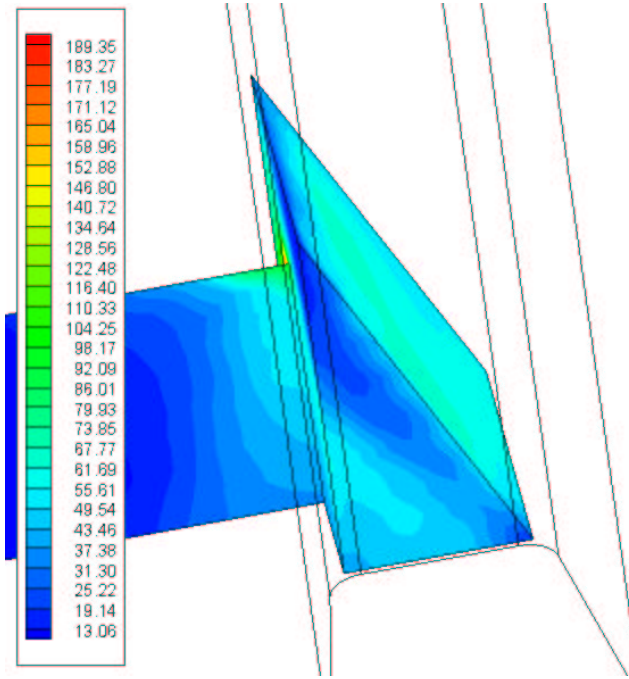


Figure 5.73 Surface Static Pressure (psi) Contours at $t = 2.0 \times 10^{-3}$ Seconds

The pressure on the underside of the slipper wedge (upper surface of the slipper wedge/rail gap) is seen in Figures 5.73-5.81. The gradients change from those caused by the impinging shock, to those resulting from the flow stagnation on the leading edge of the wedge.

When viewing the animations from which these frames were taken, some unsteadiness was observed on the underside of the strut wedge at the outflow plane. Oscillations in the pressure gradients were observed in this area toward the end of the unsteady flow simulations, that is, after the solutions were to have achieved a steady state. This suggests one of two things; either the boundary conditions are influencing the solution in non-physical ways, or there is an inherent unsteadiness in the flow at that point. These oscillations were not observed at any other location in the domain, suggesting that it is, in fact, an inherent unsteadiness. This could explain the oscillations in the residual values that prevented the reduction in residuals by three orders of magnitudes. Similar unsteadiness may have caused the second-order solutions to become unstable as well (the numerical viscosity in first-order solutions may have damped out the oscillations).

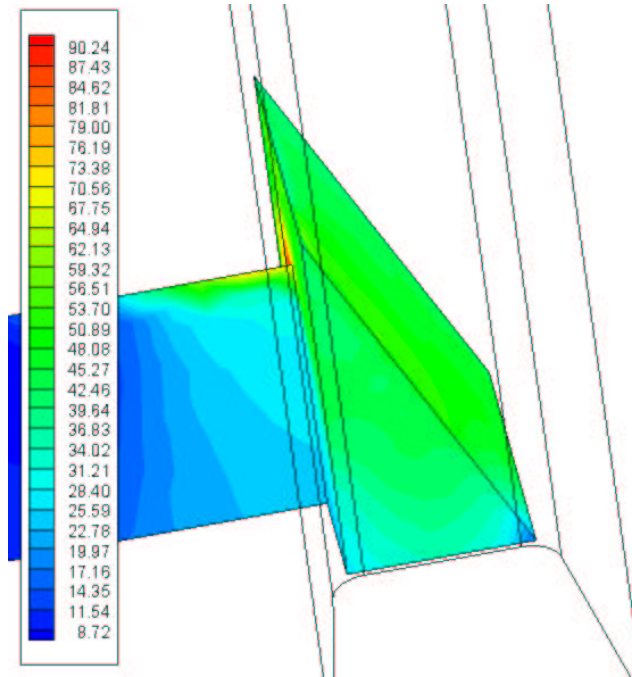


Figure 5.74 Surface Static Pressure (psi) Contours at $t = 3.0 \times 10^{-3}$ Seconds

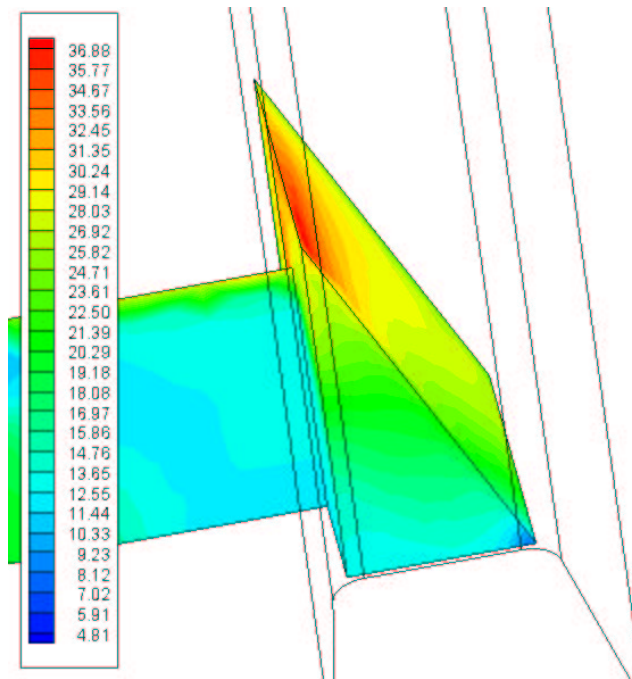


Figure 5.75 Surface Static Pressure (psi) Contours at $t = 3.3 \times 10^{-3}$ Seconds

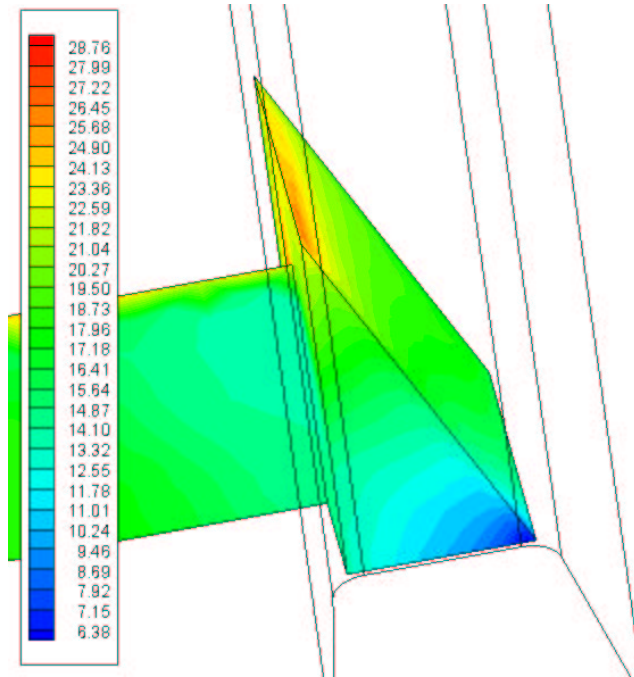


Figure 5.76 Surface Static Pressure (psi) Contours at $t = 3.5 \times 10^{-3}$ Seconds

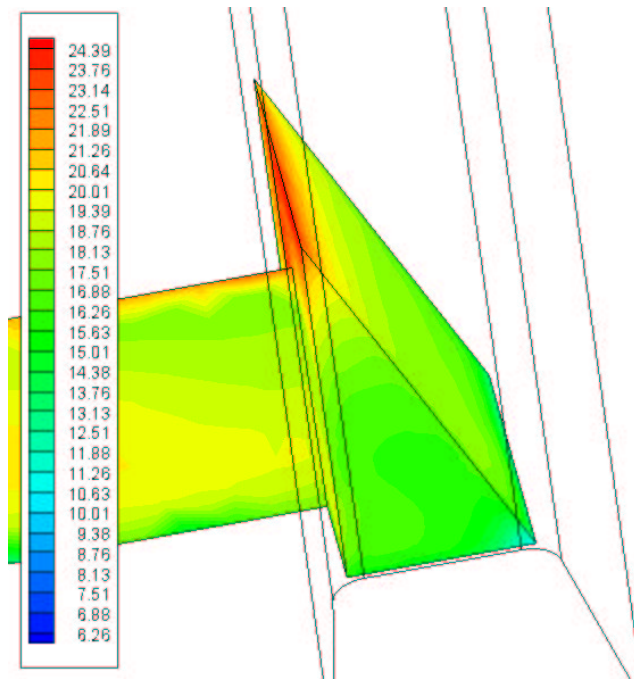


Figure 5.77 Surface Static Pressure (psi) Contours at $t = 3.7 \times 10^{-3}$ Seconds

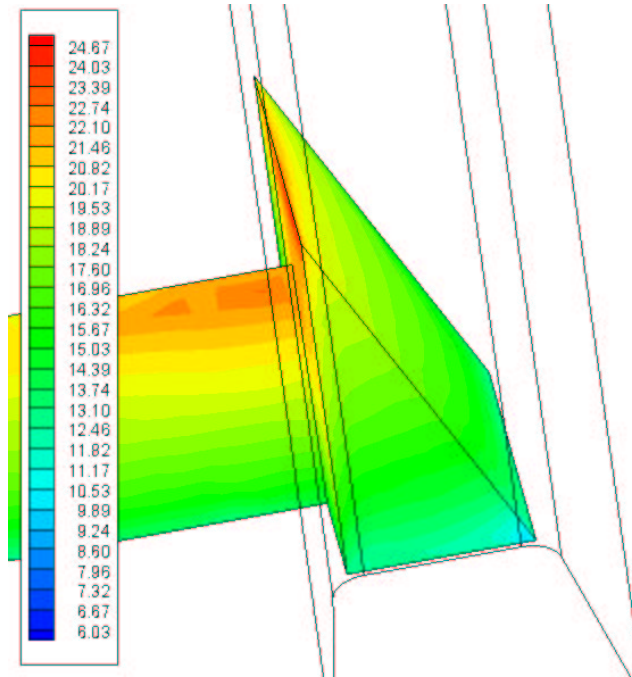


Figure 5.78 Surface Static Pressure (psi) Contours at $t = 4.0 \times 10^{-3}$ Seconds

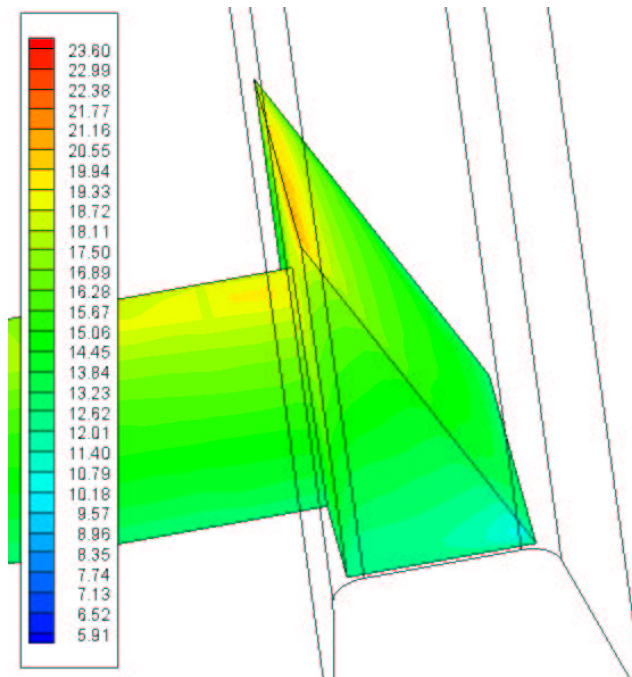


Figure 5.79 Surface Static Pressure (psi) Contours at $t = 4.5 \times 10^{-3}$ Seconds

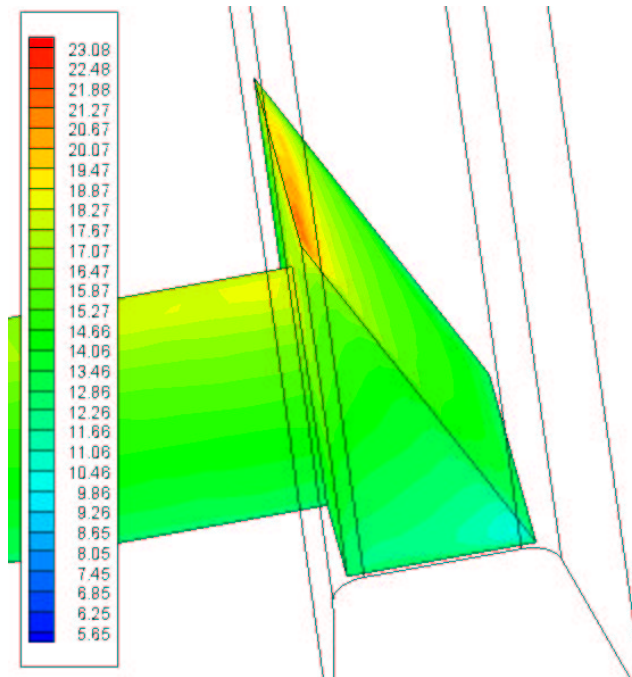


Figure 5.80 Surface Static Pressure (psi) Contours at $t = 5.0 \times 10^{-3}$ Seconds

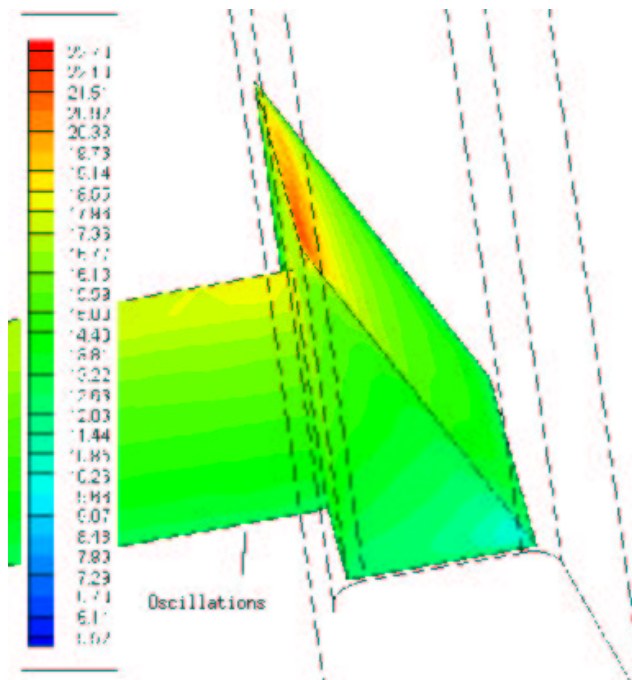


Figure 5.81 Surface Static Pressure (psi) Contours at $t = 6.0 \times 10^{-3}$ Seconds

VI. *Conclusions and Recommendations*

Steady, three-dimensional, inviscid flow solutions were presented for Mach numbers of 2 and 3 in air (2,200 and 3,300 feet per second), and for Mach numbers of 1.02, 2.5 and 3.1 in helium (3,300, 8,076 and 10,000 feet per second). Second-order solutions were obtained for the Mach 3 in air and Mach 1.02 in helium cases. The unsteady transition from air to helium at 3,300 feet per second was also modeled.

Mesh adaptation allows the computation of accurate CFD solutions while maintaining computational efficiency. The adaptation procedure, based on gradients of pressure, is an effective method to refine the flow solution in regions around shock waves and were utilized in this study. The resulting meshes contained around 2 million cells, dramatically increasing the memory and computation requirements.

Mesh quality can also impact the stability and accuracy of the solution. Node spacings in the slipper/rail gap region may not have been sufficiently small; mesh adaptations improved this to some extent. Second-order results were obtained for the $M_\infty = 3.0$ in air and $M_\infty = 1.02$ in helium cases, while only first-order results were obtained for the other cases modeled.

The thermodynamic properties of the flow around the hypervelocity sled are strongly affected by the discontinuities of the flow, such as shock waves, expansions and their interactions. In turn, the location of these shocks and expansions are dependent on the Mach number of the freestream (or velocity of the sled).

In the case of the $M_\infty = 3.0$ flow in air, the shock generated by the vertical wedge impinges on the sled structure. The resulting reflection and interaction with other flow features and structural components create a stagnation region with high temperatures and pressures. These high temperatures and pressures could weaken the structure, decreasing the performance of the sled. Additionally, the high gradients could cause vibrations and heating that would worsen damage through the gouging phenomenon.

The same deteriorating effects are not seen in the $M_\infty = 1.02$ in helium case, even though the actual velocities are the same. The magnitudes of the pressures and temper-

atures are reduced, with the maximum values being in the stagnation regions along the leading edges of the wedges.

The flow entering the slipper/rail gap is also strongly affected by the location of any shocks in the flow. Again, the aero-thermodynamic heating is reduced in the gap area when run through a helium rather than an air environment.

Future Work

The research presented here is only the beginning of what would need to be accomplished to accurately model the flow around the hypervelocity sled. Some of those areas that need future work include:

- **Improvements in mesh generation.** The existing mesh was shown to be of fairly low quality. This may have had an impact on the stability and accuracy of the solution. A suggested method to investigate the effects of mesh quality on the solution stability is to gradually build up the model from component pieces. One could start with the payload section and compute the relatively simple solution (including a second-order solution to verify stability) about that section only. Other components could then be added. In this way, areas of the mesh that affect solution stability can be found and improved.
- **Second-order solutions for all cases.** The stability and convergence properties of the second-order solver is much more sensitive than the first-order solver. Refining the mesh generation process may solve this problem.
- **Mesh adaptation.** The type of mesh adaptation discussed here (conformal node adaptation based on pressure gradients) is only a small portion of what is available in FLUENT. The main constraint on adaptation was due to memory limits; conformal node adaptation can only be performed on a single processor. Another method, the hanging-node method, while using more memory, can be performed in parallel. With more machines available, the memory constraints would not be as restrictive and the maximum gradients can be reduced further.

- **Viscous effects.** The actual aerodynamic heating that occurs as the shocks impinge on the structural components of the sled cannot be predicted without accurately modeling the viscous effects. Neither can the flow field properties be accurately modeled in the slipper/rail gap, where the boundary layer thickness may be close to the gap height. The work involved in the construction of a viscous mesh and the subsequent numerical solutions is at least an order of magnitude greater than the work in this study.
- **Modeling of the actual slipper/rail gap.** The current model was truncated forward of the actual slipper/rail gap due to numerical concerns. If the sled is modeled using a fully viscous model, these issues would no longer be of concern.
- **Pseudo-Unsteady Solutions.** The current study showed that there may be inherent unsteadiness in the flow. This unsteadiness would possibly prevent a steady solution from converging. Computing a steady solution with an unsteady scheme would capture the steady solution without the convergence difficulties.

Bibliography

1. Amtec Engineering Incorporated, Bellevue WA. *CFD Analyzer User's Manual, Version 2.0*, 1999. Electronic documentation, <http://www.amtec.com>.
2. Amtec Engineering Incorporated, Bellevue WA. *Tecplot User's Manual, Version 9, Revision 2*, August 2001.
3. Bosmajian, Neil and others. *Status of the Magnetic Levitation Upgrade of the Holloman High Speed Test Track*. AIAA Technical Paper AIAA-2000-2289, Washington DC: American Institute of Aeronautics and Astronautics, 2000.
4. Fluent Incorporated, Lebanon NH. *Fluent 6.0 User's Guide*, December 2001. Electronic documentation on CD-ROM accompanying FLUENT Version 6.0 software.
5. *Guide for the Verification and Validation of Computational Fluid Dynamics Simulations*. AIAA Guide G-077-1998, Washington DC: American Institute of Aeronautics and Astronautics, January 1998.
6. Hoffmann, Klaus A. and Steve T. Chiang. *Computational Fluid Dynamics* (Fourth Edition), *Volume II*. Wichita KS: Engineering Education System, August 2000.
7. Hoffmann, Klaus A. and Steve T. Chiang. *Computational Fluid Dynamics* (Fourth Edition), *Volume I*. Wichita KS: Engineering Education System, August 2000.
8. Hooser, Michael. *Simulation of a 10,000 Foot per Second Ground Vehicle*. AIAA Technical Paper AIAA-2000-2290, Washington DC: American Institute of Aeronautics and Astronautics, 2000.
9. Hooser, Michael D. Personal Correspondance. Holloman Air Force Base NM: 846 TS/TGTDD, 2001.
10. Jenke, Leroy M. and Ernest J. Lucas. *Supersonic Wind Tunnel Tests of Dual Rail and Monorail Rocket Sleds*. Technical Report AEDC-TR-65-70, Arnold Air Force Station TN: Arnold Engineering Development Center, April 1965.
11. Korkegi, Robert H. and Ronald A. Briggs. *Aerodynamics of the Hypersonic Slipper Bearing*. Technical Report ARL 68-0028, Wright-Patterson Air Force Base OH: Aerospace Research Laboratories, February 1968.
12. Korkegi, Robert H. and Ronald A. Briggs. "The Hypersonic Slipper Bearing—A Test Track Problem," *Journal of Spacecraft and Rockets*, 6(2):210–212 (February 1969).
13. Krupovage, Daniel J. and Hans J. Rassmussen. *Hypersonic Rocket Sled Development*. Technical Report AD-TR-82-41, Holloman Air Force Base NM: Test Track Division, September 1982.
14. Laird, David J. *The Investigation of Hypervelocity Gouging*. PhD dissertation, Graduate School of Engineering, Air Force Institute of Technology (AETC), Wright-Patterson AFB OH, January 2002 (AFIT/DS/ENY/02-01).
15. Myers, Jack. "Aerodynamic Analysis, Nike O/U Narrow Gage Sled, Generic Payload." Unpublished Draft Report, Personal Communication, February 2002.

16. National Advisory Committee for Aeronautics (NACA). *Equations, Tables and Charts for Compressible Flow*. Report 1135. Moffett Field CA: Ames Aeronautical Laboratory, 1953.
17. Pointwise, Incorporated, Fort Worth TX. *Gridgen User Manual, Version 13.3*, 1999. Electronic documentation on CD-ROM accompanying Gridgen Version 13.3 software.
18. Roache, Patrick J. *Verification and Validation in Computational Science and Engineering*. Albuquerque NM: Hermosa Publishers, 1998.
19. Schoenfeld, William P. *Requirements for Upgrading the Holloman High Speed Test Track Computational Fluid Dynamics Analytical Capability*. AIAA Technical Paper AIAA-2000-2288, Washington DC: American Institute of Aeronautics and Astronautics, 2000.
20. Thompson, Joe F., "A Reflection on Grid Generation in the 90s: Trends, Needs and Influences." <http://capella.colorado.edu/~laney/thompson.htm>, 12 December 2001.
21. U.S. Government Printing Office. *U.S. Standard Atmosphere, 1976*. Technical Report. 1976. <http://aero.stanford.edu/StdAtm.html>.
22. Warren, Gary P. and others. *Grid Convergence for Adaptive Methods*. AIAA Technical Paper AIAA-91-1591, Washington, DC: American Institute of Aeronautics and Astronautics, 1991.

Vita

Captain Andrew J. Lofthouse graduated from Timpview High School in Provo, Utah, in 1991. Following graduation, he enlisted in the United States Air Force Reserves as an Aircraft Armament Systems Specialist with the 419th Tactical Fighter Wing, Hill Air Force Base, Utah. He entered undergraduate studies at Brigham Young University in Provo, Utah where he graduated with a degree in Mechanical Engineering in December of 1997. He was commissioned as a Second Lieutenant in the United States Air Force through Detachment 855 of AFROTC at Brigham Young University where he was recognized as a distinguished graduate.

His first assignment was to the Warner Robins Air Logistics Center at Robins AFB, Georgia as an Aircraft Battle Damage Repair Engineer and a program manager. In September 2000, he was assigned to Wright-Patterson AFB, Ohio as a graduate student in the Aeronautical Engineering program at the Air Force Institute of Technology. Upon graduation, he will be assigned to the National Air Intelligence Center at Wright-Patterson AFB, Ohio.

REPORT DOCUMENTATION PAGE				Form Approved OMB No. 074-0188	
<p>The public reporting burden for this collection of information is estimated to average 1 hour per response, including the time for reviewing instructions, searching existing data sources, gathering and maintaining the data needed, and completing and reviewing the collection of information. Send comments regarding this burden estimate or any other aspect of the collection of information, including suggestions for reducing this burden to Department of Defense, Washington Headquarters Services, Directorate for Information Operations and Reports (0704-0188), 1215 Jefferson Davis Highway, Suite 1204, Arlington, VA 22202-4302. Respondents should be aware that notwithstanding any other provision of law, no person shall be subject to a penalty for failing to comply with a collection of information if it does not display a currently valid OMB control number.</p> <p>PLEASE DO NOT RETURN YOUR FORM TO THE ABOVE ADDRESS.</p>					
1. REPORT DATE (DD-MM-YYYY) 26-03-2002		2. REPORT TYPE Master's Thesis		3. DATES COVERED (From – To) Sep 2001 – Mar 2002	
4. TITLE AND SUBTITLE COMPUTATIONAL AERODYNAMIC ANALYSIS OF THE FLOW FIELD ABOUT A HYPERVELOCITY TEST SLED				5a. CONTRACT NUMBER	
				5b. GRANT NUMBER	
				5c. PROGRAM ELEMENT NUMBER	
6. AUTHOR(S) Lofthouse, Andrew J., Capt, USAF				5d. PROJECT NUMBER ENR# 1999-115	
				5e. TASK NUMBER	
				5f. WORK UNIT NUMBER	
7. PERFORMING ORGANIZATION NAMES(S) AND ADDRESS(S) Air Force Institute of Technology Graduate School of Engineering and Management (AFIT/ENY) 2950 P Street, Building 640 WPAFB OH 45433-7765				8. PERFORMING ORGANIZATION REPORT NUMBER AFIT/GAE/ENY/02-07	
9. SPONSORING/MONITORING AGENCY NAME(S) AND ADDRESS(ES) AFOSR/NM Attn: Dr. Len Sakell 801 N. Randolph Street, Romm 732 Arlington, VA 22203-1977 DSN: 426-6566				10. SPONSOR/MONITOR'S ACRONYM(S)	
				11. SPONSOR/MONITOR'S REPORT NUMBER(S)	
12. DISTRIBUTION/AVAILABILITY STATEMENT APPROVED FOR PUBLIC RELEASE; DISTRIBUTION UNLIMITED.					
13. SUPPLEMENTARY NOTES .					
14. ABSTRACT <p>The flow field about the nose section of a hypervelocity test sled is computed using computational fluid dynamics. The numerical model of the test sled corresponds to the Nike O/U narrow gage sled used in the upgrade program at the High Speed Test Track facility, Holloman Air Force Base, New Mexico. The high temperatures and pressures resulting from the aerodynamic heating and loading affect the sled structure and the performance of the vehicle. The sled transitions from an air environment to a helium environment at a speed of approximately 3,300 feet per second (Mach 3 in air, Mach 1.02 in helium) to reduce the effects of high Mach number flows. Steady, three-dimensional, inviscid flow solutions are computed for Mach numbers of 2 and 3 in air (2,200 and 3,300 feet per second), and for Mach numbers of 1.02, 2.5 and 3.1 in helium (3,300, 8,076 and 10,000 feet per second). Mesh adaptation is used to obtain a mesh-independent solution. Second-order solutions are obtained for the Mach 3 in air and Mach 1.02 in helium cases. The unsteady transition from air to helium at 3,300 feet per second is also modeled. Mach 3 in air computations are compared with analytical results.</p>					
15. SUBJECT TERMS High Velocity, Test Vehicles, Computational Fluid Dynamics, Hypersonic Test Vehicles, Euler Equations					
16. SECURITY CLASSIFICATION OF:		17. LIMITATION OF ABSTRACT UU	18. NUMBER OF PAGES 118	19a. NAME OF RESPONSIBLE PERSON Lt Col Montgomery C. Hughson	
a. REPORT U	b. ABSTRACT U			c. THIS PAGE U	19b. TELEPHONE NUMBER (Include area code) (937) 255-3636 ext 4597

Standard Form 298 (Rev. 8-98)
Prescribed by ANSI Std. Z39-18

Form Approved
OMB No. 074-0188